Quantum Monte Carlo Studies of Strongly Correlated Fermion- and Spin-Systems with Competing Interactions

Von der Fakultät für Mathematik, Informatik und Naturwissenschaften
der RWTH Aachen University zur Erlangung des akademischen Grades
eines Doktors der Naturwissenschaften genehmigte Dissertation

vorgelegt von
Alexander Sushchyev, M.Sc.
aus Winniza, Ukraine

Berichter: Prof. Stefan Weßel, Ph. D
Prof. Dr. rer. nat. Dante Kennes

Tag der mündlichen Prüfung: 17. 06. 2024

“*Maybe it’s not too late to learn how to love and forget how to hate.*”

- Crazy Train by Ozzy Osbourne

Abstract

In this thesis we study (quantum) phase transitions in fermion and spin systems. In the first part we consider the Hubbard model on the square lattice at half filling. For a more realistic description of real materials with partially screened Coulomb interactions, we include non-local repulsive terms. In detail, we include (i) nearest-neighbor interactions and (ii) long-range Coulomb (LRC) interactions. Based on DQMC simulations within sign-problem free coupling regimes we report results for the temperature resolved double occupancy and entropy, assess a recent study in terms of a first-order metal-to-insulator transition and discuss various phase transitions in the vicinity of the analyzed parameter regime. Continuing DQMC simulations, we examine the Hubbard model on an ABCA stacked tetra-layer graphene structure regarding its magnetic ground state properties over a wide range of the local Hubbard-U. Motivated by experimental findings, we added an extended layer-to-layer interaction and analyzed the extended model in the sign-problem free regime. The second part considers the Heisenberg model regarding different spin exchange interactions, based on SSE simulations. We examine the most generic case of three varying couplings along the unequivalent directions on a honeycomb lattice, where we find anomalous finite-size scaling corrections in the Binder ratio along the quantum phase transition lines between an AFM order and dimerized unordered states. Finally, we extend our Heisenberg model studies to the three-dimensional diamond lattice for both antiferromagnetic as well as ferromagnetic couplings. We determine the finite critical temperatures and find the value of the Néel temperature to be higher than the value for the Curie temperature. We discuss the stability of the ordered phases against thermal fluctuations with respect to the low-temperature entropy gain.

Zusammenfassung

In der vorliegenden Arbeit untersuchen wir (Quanten-)Phasenübergänge in Fermionen- und Spinsystemen. Im ersten Teil betrachten wir das Hubbard-Modell auf einem quadratischen Gitter bei halber Füllung. Um eine realistischere Beschreibung realer Materialien mit teilweise abgeschirmten Coulomb-Wechselwirkungen zu erhalten, erweitern wir das Modell um nicht-lokale repulsive Terme. Im Detail beziehen wir (i) Nächste-Nachbar-Wechselwirkungen und (ii) Langstrecken-Coulomb-Wechselwirkungen (LRC) ein. Auf der Grundlage von DQMC-Simulationen in vorzeichenfreien Kopplungsregimen geben wir Ergebnisse für die temperaturaufgelöste Doppelsetzung und Entropie wieder, bewerten eine aktuelle Studie im Hinblick auf einen Metall-Isolator-Übergang erster Ordnung und diskutieren verschiedene Phasenübergänge in der Nähe des analysierten Parameterbereiches. In Fortsetzung der DQMC-Simulationen untersuchen wir das Hubbard-Modell auf einer ABCA-gestapelten Tetra-Schicht-Graphenstruktur hinsichtlich seiner magnetischen Grundzustandseigenschaften über einen weiten Bereich des lokalen Hubbard-U. Motiviert durch experimentelle Befunde fügten wir eine erweiterte Schicht-zu-Schicht-Wechselwirkung hinzu und analysierten das erweiterte Modell im vorzeichenfreien Regime. Im zweiten Teil betrachten wir das Heisenberg-Modell im Hinblick auf verschiedene Spin-Austausch-Wechselwirkungen, basierend auf SSE-Simulationen. Wir untersuchen den allgemeinsten Fall von drei variierenden Kopplungen entlang der ungleichen Richtungen auf einem Wabengitter, wo wir anomale Skalierungskorrekturen auf endlichen Systemgrößen im Binder-Verhältnis entlang der Quantenphasenübergangslinien zwischen einer AFM-Ordnung und dimerisierten ungeordneten Zuständen finden. Schließlich weiten wir unsere Untersuchungen des Heisenberg-Modells auf das dreidimensionale Diamantgitter aus, sowohl für antiferromagnetische als auch für ferromagnetische Kopplungen. Wir bestimmen die endlichen kritischen Temperaturen und stellen fest, dass der Wert der Néel-Temperatur höher ist als der Wert für die Curie-Temperatur. Wir diskutieren die Stabilität der geordneten Phasen gegenüber thermischen Fluktuationen im Hinblick auf den Entropiegewinn bei niedrigen Temperaturen.

Contents

Acronyms

AFM antiferromagnet

CDW charge density wave

DFT density functional theory

DMFT dynamical mean field theory

DMRG density matrix renormalization group

DOS density of states

DQMC determinant quantum Monte Carlo

ED exact diagonalization

FM ferromagnet

HS Hubbard-Stratonovich

iPEPS infinite projected entangled pair states

LRC long range Coulomb

MC Monte Carlo

QMC quantum Monte Carlo

RG renormalization group

SDW spin density wave

SSE stochastic series expansion

TDL thermodynamic limit

Introduction

1

In condensed matter physics, fermionic many-body systems have been successfully studied by an effective single-particle picture, which is the integral element of simple band structure calculations. A cornerstone for the description of metals is Landau's Fermi liquid theory (see the review in Ref. [3]). It maps the interacting electron system to non-interacting quasiparticles "dressed" by interactions, so that the degrees of freedom, such as spin, charge and momentum, remain the same as for non-interacting fermions (Fermi gas), while dynamical properties, like the mass or magnetic moments, are renormalized. In the case of weak interactions (and a spatial dimension larger or equal to two) the single-particle picture is still applicable, even in ordered states determined by instabilities, e.g. the divergence of the magnetic susceptibility. However, when interactions become stronger, i.e., competing on the same scale with the kinetic energy, a fermionic many-body system's properties cannot be expressed properly by filling up single-particle energy eigenstates [3]. The study of such *strongly correlated* many-body systems and the understanding of mechanisms that induce (quantum) phase transitions is an ongoing quest in current condensed matter research.

Phase transitions describe the change between different states in which matter may exist. They can be distinguished into two groups: first and second order transitions, where the former is characterized by a discontinuity in its observables, while the latter shows a continuous change of certain quantities in a model's parameter space. Many such transitions are characterized as critical phenomena, at which degrees of freedom at all scales are coupled in a non-trivial manner. Even though a microscopic model contains only short-ranged interactions, a state with macroscopic long-ranged order can emerge. This process is called "spontaneous symmetry breaking", where an ordered state exhibits less symmetry than the model itself. These critical points, where small and large scales are not well separated, can be classified by the divergence of various quantities, e.g., the correlation length ξ of a two-point correlation function for the local magnetization or density. Successive elimination of short-ranged degrees of freedom through appropriate Hamiltonian mappings, allows one to generate predictions for long-distance physical features, which was the fundamental idea in the development of the renormalization group (RG) [4, 5]. This technique may lead to fixed points, at which the system on different length scales "looks" the same. Essentially, this formalism predicts, as a result of the independence on microscopic details, the same critical behavior for different model groups. This allows for the classification into *universality classes.*

A prominent example of a thermal phase transition in strongly correlated electron systems, such as transition-metal compounds, is the *metal-to-insulator* transition [6]. According to band structure calculations, a system exhibits metallic behavior, but incorporating interactions, it can exhibit insulating behavior at low temperatures. To describe the competition of repulsive Coulomb interaction and kinetic energy for itinerant electrons in a theoretical (lattice) framework the Hubbard model [7–9] has been proposed in the 1960s and remains intensively studied to this day (see Ref. [10] for a recent review). Indeed, the first part of this thesis explores extended interaction models based on the Hubbard model

$$H = -t \sum_{\langle i,j \rangle, \sigma} \left(c^{\dagger}_{i\sigma} c_{j\sigma} + \text{h.c.} \right) + U \sum_{i} n_{i\uparrow} n_{i\downarrow} \tag{1.1}$$

on different lattices regarding thermal, as well as quantum phase transitions, i.e. transitions induced through quantum fluctuations at $T = 0$. Here, t denotes the hopping amplitude between nearest-neighbor sites $\langle i, j \rangle$, $c^{\dagger}_{i\sigma}$ ($c_{i\sigma}$) the fermionic creation (annihilation) operator on lattice site i and spin projection $\sigma = \uparrow, \downarrow$, U the on-site repulsion and $n_{i\sigma} = c^{\dagger}_{i\sigma} c_{i\sigma}$ the spin resolved, local number counting operator.

In chapter 3, we explore the influence of extended non-local interactions on the thermodynamic properties of the pure Hubbard model on the square lattice at half-filling for theoretical studies of materials with more realistic partially screened interactions. Additionally to the on-site U-interaction, we include two cases: (i) nearest-neighbor interactions and (ii) long-range Coulomb (LRC) interactions. We perform determinantal quantum Monte Carlo (DQMC) simulations within sign-problem free coupling regimes at finite temperatures, assess a recent study regarding a first-order metal-to-insulator transition and propose a possible scenario how non-local interactions expand the Hubbard model phase diagram.

In chapter 4, we study ground state properties of the Hubbard model on a honeycomb tetra-layer lattice at half-filling based on the projective DQMC scheme. The low-energy band structure of graphene multi-layers shows a sharply peaked density of states (DOS) at the Fermi level, which enhances correlation effects and allows for interaction-driven magnetic order. We explore magnetic correlations over a wide range of interaction strengths and investigate the scenario of amplified inter-layer hopping strengths and extended layer-to-layer interactions.

We find strong magnetic correlations emerging at higher interaction strengths compared to the square lattice case. If we follow this trend of increasing interactions, what physical behavior and phase transitions can we explore? Upon further increasing the on-site interaction strength at half-filling, we may drive a fermion system into a regime where charge fluctuations are frozen out, while retaining the spin degree of freedom. The charge density is localized at the lattice sites with an effective spin exchange interaction, resulting in a quantum spin model, namely the spin-1/2 Heisenberg model

$$H = \sum_{\langle ij \rangle} J_{ij} \, \mathbf{S}_i \cdot \mathbf{S}_j \, , \tag{1.2}$$

with $J_{ij} = 4t_{ij}^2/U$ being the coupling strength of neighboring spins described by the vector spin operator $\mathbf{S}_i$. While the Hubbard model describes itinerant magnetic behavior of the conduction band electrons for arbitrary band fillings, the Heisenberg model is a model of fully localized strongly interacting spins that arises for an exactly half-filled band, which is the basis for the second part of this thesis. The derivation of the Heisenberg model as an effective description of the Hubbard model in the high-U regime is insightfull. The idea is to decompose the Hubbard Hamiltonian into processes that leave double occupied sites unchanged and in those that increase (decrease) the double occupancy of a lattice site. Then, the goal is to find a suitable operator that minimizes or eliminates those processes changing the double occupancy within a unitary Schrieffer-Wolff transformation [11]. Up to lowest order in the separated energy scales one ends up with the t-J model at arbitrary fillings as an effective description of low-energy Hubbard physics and the Heisenberg model at half-filling [12]. While isolated spins are simply described in a one-particle picture, the interactions between them may induce collective magnetism in various compounds [13–17]. In a realistic setup, the interaction between spins however is not uniform, but shows different strengths regarding for instance different spatial directions [18, 19], thus giving rise to quantum phase transitions in the ground state, e.g. between ordered and (dimerized) unordered states. The ordering is determined by the sign of the coupling, i.e., $J > 0$ leads to antiferromagnetic alignment (spins on neighboring sites point in opposite directions) and $J < 0$ to ferromagnetism (spins point in the same direction).

In chapter 5, we determine the ground state phase diagram of the spin-1/2 antiferromagnetic Heisenberg model on the honeycomb lattice. Within our quantum Monte Carlo (QMC) simulations based on the stochastic series expansion (SSE) formulation, we consider the most generic case of varying exchange couplings along the three different lattice directions. We determine continuous quantum phase transition lines that separate an antiferromagnetic state from three quantum disordered dimer states. In the QMC studies, we find anomalously large scaling corrections in the finite-size data. In this context, we include more general comments on the non-universality of critical cumulant ratios in anisotropic systems.

In chapter 6, we turn to a three-dimensional lattice, thus overcoming the impossibility of continuous symmetry breaking in two and one spatial dimensions at finite temperatures, which is known as the Mermin-Wagner theorem [20]. In this regard, we examine the spin-1/2 Heisenberg model on the diamond lattice with both antiferromagnetic as well as ferromagnetic nearest-neighbor exchange couplings, based on SSE simulations. We determine both critical temperatures from paramagnet to (anti)ferromagnetic order through a finite-size scaling analysis. We find a significant difference in the values of the critical temperatures, which we discuss with respect to the stability of the antiferromagnetic (AFM) and ferromagnetic (FM) state against fluctuations based on the respective temperature-resolved entropy.

Despite their simple formulation, solutions to the above mentioned interacting quantum models turn out to be a challenging problem and led to the development of highly advanced numerical methods. The most intuitive approach to investigate thermodynamic properties is to diagonalize the full Hamiltonian matrix on finite lattices given a proper basis. Although unbiased, the exact diagonalization (ED) technique [21] has the highest computational cost due to the exponential growth of the Hilbert space with system size. This renders the ED method to be the perfect benchmark trial for more complex unbiased methods or approximative approaches, at least for small system sizes. Often interesting behavior can only be observed, or numerically resolved, on much larger sizes than accessible with ED. Therefore, we employ the powerful machinery of QMC methods. To be precise, we use DQMC [22] for fermionic systems. Its computational cost scales linear in inverse temperature and cubic in the system size. For spin systems, we use the SSE [23–25] that has also a linear scaling in inverse temperature, but scales also linear in the number of spins. Both methods rely on efficient statistical sampling the significant part of the configuration space (e.g., in the easiest case the spin projection configurations). Albeit the fact that QMC methods are unbiased, they are often limited to certain parameter regimes. For sign-problem free simulations, DQMC is restricted to Hubbard type models at half-filling and non-frustrated lattices. SSE exhibits a sign-problem on geometrically frustrated lattices, which can be mended to a certain degree [26–29]. Further prominent and successful methods in strongly correlated condensed matter physics involve dynamical mean-field theory (DMFT) [30, 31], the density matrix renormalization group (DMRG) [32, 33], which in particular is well suited for one dimensional systems, its two-dimensional extension iPEPS [34] or the manifold descendants of the renormalization group [4, 5].

Before presenting the results on the fermionic models in Chap. 3, 4 and the spin models in Chap. 5, 6, we introduce the QMC methods relevant for this thesis in Chap. 2. Finally, we summarize the individual conclusions and outlooks in Chap. 7

Monte Carlo Methods

2

In this chapter we introduce the QMC methods used in this thesis. Monte Carlo methods are a powerful technique for statistically unbiased large-scale simulations of classical as well as quantum lattice models. Here, we employ two different formulations, namely the DQMC and the SSE. The former suits the study of strongly correlated fermion lattice models, e.g., the Hubbard model, the latter is used to investigate spin models, e.g., the Heisenberg model. These are only two methods from a wide range of quantum Monte Carlo schemes, tailored to different models and scenarios.
To understand the quantum formulation of any QMC scheme, it is instructive to begin with classical Monte Carlo.

2.1 Classical Monte Carlo

The outline of this section follows the detailed description in Refs. [35, 36]. In general, the Monte Carlo (MC) method is a powerful tool to estimate high-dimensional integrals. Thus, a natural application is the evaluation or rather the estimation of statistical quantities of many-body systems. The fundamental values to be calculated in any MC simulation are the estimates of the expectation value and the variance for an in general unknown distribution. The expectation value of an observable O is given by

$$\langle O \rangle_P = \int_\Omega \mathrm{d}^d\vec{x}\, O(\vec{x}) P(\vec{x}), \tag{2.1}$$

where the *configuration space* Ω is a set of elementary random variables, $\vec{x} \in \Omega$ is one such *configuration* of the system's constituents and $P(\vec{x})$ is a probability distribution satisfying positivity and a normalization condition:

$$P(\vec{x}) \geq 0, \tag{2.2}$$

$$\int_\Omega \mathrm{d}^d\vec{x}\, P(\vec{x}) = 1. \tag{2.3}$$

For a classical statistical mechanics problem we typically consider the probability distribution to be the Boltzmann distribution $P(\vec{x}) = Z^{-1} \exp^{-\beta H(\vec{x})}$, where $Z = \int_\Omega \mathrm{d}^d\vec{x}\, \mathrm{e}^{-\beta H(\vec{x})}$ and $\vec{x} \in \mathbb{R}^N$ is a vector denoting the configuration of N particles in the model described by the Hamilton function $H(\vec{x})$. It would be possible to calculate $\langle O \rangle_P$ directly by brute force integration. However, the phase space of reasonable system sizes becomes very large and this procedure turns out to be slow or even numerically impossible.

A more elegant and faster way to compute such integrals is the stochastic approximation of $\langle O \rangle_P$. It is obtained by generating an independent sequence of random configurations $\vec{x}_i \in \Omega$ $(i = 1, ..., M)$ drawn from the probability distribution $P(\vec{x}_i)$. Then the *estimator* $\bar{O}_M$ is calculated by the mean

$$\bar{O}_M = \frac{1}{M} \sum_{i=1}^{M} O(\vec{x}_i), \tag{2.4}$$

where $O(\vec{x}_i)$ is a snapshot, mathematically speaking the evaluation, of a function O for a given random configuration $\vec{x}_i$. We obtain numerically exact, respectively *unbiased*, results through the implicit action of the central limit theorem. It states that in the large M limit the underlying probability (or sampling) distribution of $\bar{O}_M$ tends to a Gaussian distribution

$$P(\bar{O}_M) = \frac{1}{\sqrt{2\pi\sigma^2}} \exp^{-\frac{(\bar{O}_M - \langle O \rangle_P)^2}{2\sigma^2}} \tag{2.5}$$

with

$$\sigma^2 = \frac{1}{M} \left(\langle O^2 \rangle_P - \langle O \rangle_P^2 \right). \tag{2.6}$$

In particular, as we increase M, the estimators converge with the rate $1/\sqrt{M}$, e.g. to increase the accuracy by a factor of 10, we need to provide 100 more samples.

2.1.1 Importance Sampling

The simplest and most naive approach to sample the configurations $\vec{x}_i$ is by randomly drawing them uniformly from the configuration space Ω. In our classical example this means that for the set of all particles in the system we randomly choose a configuration $\vec{x}_i$ from a finite set of configurations and evaluate the observable O at the given configuration space point. We repeat this procedure until we reach a satisfactory accuracy in the statistical error. Albeit foolproof, this *simple sampling* has the major disadvantage that it samples configurations with vanishing probability weights. Usually only a small amount of configurations has a significant weight in the calculation of the statistical quantities. The optimal choice of any $\vec{x}_i$ would be drawing it with a probability proportional to the underlying probability density $P(\vec{x})$. This process is called *importance sampling* and can be realized in a Markov Chain [37]. The chain can be illustrated as follows:

$$\vec{x}_0 \xrightarrow{W} \vec{x}_1 \xrightarrow{W} \vec{x}_2 \xrightarrow{W} ... \xrightarrow{W} \vec{x}_M$$

Starting with a (uniformly drawn) initial configuration $\vec{x}_0$ we update one degree of freedom in $\vec{x}_i$ to obtain $\vec{x}_{i+1}$ with a transition probability $W(\vec{x}_i \to \vec{x}_{i+1})$, i.e. each new configuration depends on its predecessor. This simple scheme comes with the price that it introduces an autocorrelation, which means that the configurations are not strictly independent of each other. We elaborate on how to work with this circumstance and how to maintain unbiased results in Sec. 2.4.

The transition probability obeys following conditions:

(i) Positivity: $W(\vec{x}_i \to \vec{x}_{i+1}) \geq 0, \quad \forall \vec{x}_i, \vec{x}_{i+1} \in \Omega$

(ii) Normalization: $\sum_{\vec{x}_{i+1}} W(\vec{x}_i \to \vec{x}_{i+1}) = 1, \quad \forall \vec{x}_i \in \Omega$

(iii) Stationarity: $\sum_{\vec{x}_i} W(\vec{x}_i \to \vec{x}_{i+1}) P(\vec{x}_i) = P(\vec{x}_{i+1}), \quad \forall \vec{x}_{i+1} \in \Omega$

The distribution of the generated configurations $\{\vec{x}_i\}$ is guaranteed to converge to the target distribution $P(\vec{x}_i)$ under two conditions:

- **Ergodicity**: Each configuration $\vec{x}_j$ can be reached starting from another configuration $\vec{x}_i$ with non-vanishing probability in a finite number of steps.
- **Detailed balance**: The transition probabilities are related to the target distribution through the relation

  $$W(\vec{x}_i \to \vec{x}_{i+1}) P(\vec{x}_i) = W(\vec{x}_{i+1} \to \vec{x}_i) P(\vec{x}_{i+1}). \tag{2.7}$$

  This automatically fulfills the stationarity condition

  $$\sum_{\vec{x}_i} W(\vec{x}_i \to \vec{x}_{i+1}) P(\vec{x}_i) = P(\vec{x}_{i+1}) \sum_{\vec{x}_i} W(\vec{x}_{i+1} \to \vec{x}_i) = P(\vec{x}_{i+1})$$

Given the general rules for the Markov process, there are different possibilities how to realize the transitions. Reformulating the detailed balance condition (2.7) into

$$\frac{f(R)}{1 + f(R)} = R, \tag{2.8}$$

where $f(R)$ is a function of the acceptance ratio $R = P(\vec{x}_{i+1})/P(\vec{x}_i)$, we find several choices of $f(R)$ to satisfy this equation. Note that the normalization constants cancel each other. Well established solutions are, e.g.

- Metropolis algorithm [38]: $W(\vec{x}_i \to \vec{x}_{i+1}) = f(R) = \min(1, R)$
- Heat-bath algorithm [39]: $W(\vec{x}_i \to \vec{x}_{i+1}) = f(R) = R/(1 + R)$

Contrary to the sequential update scheme presented above there is a class of update schemes known as global updates, e.g., the Wolff cluster algorithm [40]. In these schemes several degrees of freedom are updated at the same time making a significant change to the system's current state. The advantage over sequential schemes is the improved performance in the vicinity of second order phase transitions.

The crucial ingredient for a Monte Carlo simulation is to find a suitable transition probability for the configuration updates for the sampling procedure. While for a classical problem the Boltzmann factor $\mathrm{e}^{-\beta H(\vec{x}_i)}$ is always a real number greater zero and thus can be used as a probability measure, for a quantum system this no longer holds true. In general, the configuration weight, associated with the operator exponential $\mathrm{e}^{-\beta \hat{H}(\vec{x}_i)}$, is a complex number, so that we have to find other ways to express a well defined transition probability for quantum Monte Carlo simulations or find cases, where the weight is positive.

The next two sections will cover such formulations of the Monte Carlo scheme for particular quantum lattice models. We will see that the quantum algorithms in essence boil down to classical Monte Carlo propagated through imaginary time τ from 0 to β.

2.2 Determinantal Quantum Monte Carlo

In this section we introduce the fundamental construction of two forms of DQMC algorithms for fermionic lattice systems with spin and charge degrees of freedom. A pedagogical introduction to the DQMC technique can be found in Refs. [41, 42].

The so called Blankenbecler, Scalapnio, Sugar (BSS) algorithm [22] is the primary choice for the unbiased numerical study of a vast range of strongly correlated electron systems. One is able to simulate thermodynamic properties of Hubbard type models [43, 44], topological insulators [45–48], superconductivity in spin-orbit split flat bands [46, 49], long-range Coulomb interacting graphene systems [50–54] and Yukawa SYK models [55], to name a few. DQMC allows for an unbiased determination of different phase transitions like the metal-to-insulator transition [56] or nematic [57, 58] and magnetic [59, 60] quantum phase transitions in metals and enables the exploration of rich phase diagrams.

The DQMC methods we use in this work transform the (grand) canonical partition function (the chemical potential term is included in the kinetic energy) in the form

$$Z = \mathrm{Tr}\left(\mathrm{e}^{-\beta H}\right) = \sum_{C} \xi(C)\, \mathrm{e}^{-S(C)}, \tag{2.9}$$

where β is the inverse temperature, $\xi(C)$ is a configuration dependent prefactor to the exponential of the action $S(C)$ of non-interacting fermions subject to a space-time fluctuating auxiliary field. This field stems from a Hubbard-Stratonovich (HS) transformation (see App. A.1.2) decoupling the electron-electron interaction into an electron-field interaction. With this we are able to sample the partition function. The algorithms scale linear in imaginary time β and cubic in the volume N, i.e. the number of lattice sites.

The DQMC method can be subdivided in a projective QMC scheme for $T = 0$ properties in the canonical ensemble and in a finite temperature algorithm in the grand canonical ensemble. The finite temperature version can be used to probe for ground state properties as well by going to sufficiently low temperatures, but the projective scheme is computationally more efficient for this task [42]. In the following, we demonstrate the steps required to extract a well defined probability measure from the partition function. The calculations for both versions follow the same steps.

2.2.1 Partition Function

The goal of our QMC computations is to obtain the thermodynamic expectation value in the (grand) canonical ensemble of an observable O:

$$\langle O \rangle = \frac{1}{Z} \mathrm{Tr} \left(O \mathrm{e}^{-\beta H} \right), \tag{2.10}$$

where $Z = \mathrm{Tr}\, \mathrm{e}^{-\beta H}$. In the following we demonstrate the reformulation of the partition function on the U-V model (3.1), which is the main subject in Chap. 3. First, we have to write the interaction terms in quadratic form to allow the application of the Hubbard-Stratonovich transformation. The Hamiltonian reads

$$H = H_t + \frac{\bar{U}}{2} \sum_i (n_i - 1)^2 + \frac{V}{2} \sum_{\langle i,j \rangle} (n_i + n_j - 2)^2, \tag{2.11}$$

where H_t contains the nearest-neighbor hoppings and the chemical potential term, $n_x = n_{x\uparrow} + n_{x\downarrow}$ is the sum of the spin resolved number operators and $\bar{U} = U - z_D V$ is a renormalized on-site interaction. $z_D = 2 \cdot D$ is a spacial dimension D dependent prefactor to the inter-site interaction V. We begin with the Suzuki-Trotter decomposition (see App. A.1.1) of the operator exponential

$$\begin{aligned}
\mathrm{e}^{-\beta H} &= \exp \left(-\beta \left(H_t + \frac{\bar{U}}{2} \sum_{i=1}^{N} (n_i - 1)^2 + \frac{V}{2} \sum_{\langle ij \rangle = 1}^{DN} (n_i + n_j - 2)^2 \right) \right) && (2.12) \\
&= \left[\mathrm{e}^{-\Delta\tau H_t} \mathrm{e}^{-\Delta\tau \frac{\bar{U}}{2} \sum_{i=1}^{N} (n_i - 1)^2} \mathrm{e}^{-\Delta\tau \frac{V}{2} \sum_{\langle ij \rangle = 1}^{DN} (n_i + n_j - 2)^2} \right]^{L_T} + \mathcal{O}(\Delta\tau^2) && (2.13) \\
&= \prod_{m=1}^{L_T} \left[\mathrm{e}^{-\Delta\tau H_t} \prod_{i=1}^{N} \mathrm{e}^{-\Delta\tau \frac{\bar{U}}{2} (n_i - 1)^2} \prod_{\langle i,j \rangle = 1}^{DN} \mathrm{e}^{-\Delta\tau \frac{V}{2} (n_i + n_j - 2)^2} \right] + \mathcal{O}(\Delta\tau^2) && (2.14)
\end{aligned}$$

This allows the decomposition of the exponential of our full Hamiltonian into products of exponentials of the individual terms. Furthermore, we discretize the imaginary time into $L_T = \beta / \Delta\tau$ time slices of "thickness" $\Delta\tau$, introducing thereby a systematic error in the order of magnitude of $\Delta\tau^2$.

The next step is to apply the Hubbard-Stratonovich decomposition for the interaction terms:

$$\begin{aligned}\mathrm{e}^{-\beta H} = \prod_{m=1}^{L_T} &\left[\mathrm{e}^{-\Delta\tau H_t} \prod_{i=1}^{N} \sum_{a_{i,m}=\pm1,\pm2} \gamma(a_{i,m}) \mathrm{e}^{\sqrt{-\Delta\tau\frac{\bar{U}}{2}\eta(a_{i,m})(n_i-1)}} \right] \times \\ &\left[\prod_{\langle ij\rangle=1}^{DN} \sum_{b_{i,m}=\pm1,\pm2} \gamma(b_{i,m}) \mathrm{e}^{\sqrt{-\Delta\tau\frac{V}{2}}\eta(b_{i,m})(n_i+n_j-2)} \right] + \mathcal{O}(\Delta\tau^2)\,. \end{aligned} \tag{2.15}$$

Having decoupled the electron-electron interaction, we can carry out the sums over the field variables and rearrange the trace over the above expression in the following way:

$$\begin{aligned}\operatorname{Tr}\mathrm{e}^{-\beta H} &= \sum_{C} \left(\prod_{m=1}^{L_T} \prod_{i=1}^{N} \gamma(a_{i,m})\gamma(b_{i,m}) \right) \times \\ \operatorname{Tr} &\prod_{m=1}^{L_T} \left(\mathrm{e}^{-\Delta\tau H_t} \prod_{i=1}^{N} \mathrm{e}^{\sqrt{-\Delta\tau\frac{\bar{U}}{2}}\eta(a_{i,m})(n_i-1)} \prod_{\langle ij\rangle=1}^{DN} \mathrm{e}^{\sqrt{-\Delta\tau\frac{V}{2}}\eta(b_{i,m})(n_i+n_j-2)} \right) + \mathcal{O}(\Delta\tau^2)\ . \end{aligned} \tag{2.16}$$

The sum runs over the configuration space $C = \{a_{i,m}, b_{i,m} | i = 1 \dots L, m = 1 \dots L_T\}$, where each $a_{i,m}$ or $b_{i,m}$ takes the values ±1 or ±2. These configurations are to be sampled with the Monte Carlo scheme. On every time slice the fields are updated sequentially. We iterate over the number of lattice sites and proposes an update of the local HS field to one of the other three possible values with probability 1/3.

The final step to obtain the form of the partition function in Eq. (2.9) is to trace out the fermions. The trace runs over the fermionic Fock space and for a given configuration we can express it as a determinant (see App. A.1.3). Notice that the trace is independent of the spin degree of freedom, which is a consequence of the SU(2) symmetry of the Hamiltonian and the chosen HS transformation.

$$\begin{aligned}&\operatorname{Tr} \prod_{m=1}^{L_T} \left(\mathrm{e}^{-\Delta\tau H_t} \prod_{i=1}^{N} \mathrm{e}^{\sqrt{-\Delta\tau\frac{\bar{U}}{2}}\eta(a_{i,m})\left(n_{i\uparrow}+n_{i\downarrow}-1\right)} \prod_{\langle ij\rangle=1}^{DN} \mathrm{e}^{\sqrt{-\Delta\tau\frac{V}{2}}\eta(b_{i,m})\left(n_{i\uparrow}+n_{i\downarrow}+n_{j\uparrow}+n_{j\downarrow}-2\right)} \right) \\ &= \operatorname{Tr} \left[\prod_{m} \left(\mathrm{e}^{-\Delta\tau H_t} \prod_{i} \mathrm{e}^{\sqrt{-\Delta\tau\frac{\bar{U}}{2}}\eta(a_{i,m})(n_i-1/2)} \prod_{\langle ij\rangle} \mathrm{e}^{\sqrt{-\Delta\tau\frac{V}{2}}\eta(b_{i,m})(n_i+n_j-1)} \right) \right]^2 \end{aligned} \tag{2.17}$$

$$\begin{aligned}&= \left(\prod_{m} \prod_{i} \mathrm{e}^{-\frac{1}{2}\sqrt{-\Delta\tau\frac{\bar{U}}{2}}\eta(a_{i,m})} \prod_{\langle ij\rangle} \mathrm{e}^{-\sqrt{-\Delta\tau\frac{V}{2}}\eta(b_{i,m})} \right)^2 \times \\ &\operatorname{Tr} \left(\prod_{m} \mathrm{e}^{-\Delta\tau H_t} \prod_{i} \mathrm{e}^{\sqrt{-\Delta\tau\frac{\bar{U}}{2}}\eta(a_{i,m}) n_i} \prod_{\langle ij\rangle} \mathrm{e}^{\sqrt{-\Delta\tau\frac{V}{2}}\eta(b_{i,m})(n_i+n_j)} \right)^2 \end{aligned} \tag{2.18}$$

$$
\begin{aligned}
&= \prod_m \prod_i \mathrm{e}^{-\sqrt{-\Delta\tau\frac{\bar{U}}{2}}\eta(a_{i,m})} \prod_{\langle ij\rangle} \mathrm{e}^{-2\sqrt{-\Delta\tau\frac{V}{2}}\eta(b_{i,m})} \times \\
&\left(\det\left[\boldsymbol{I} + \prod_m \mathrm{e}^{-\Delta\tau T} \prod_i \mathrm{e}^{\sqrt{-\Delta\tau\frac{\bar{U}}{2}}\eta(a_{i,m})A^{(i)}} \prod_{\langle ij\rangle} \mathrm{e}^{\sqrt{-\Delta\tau\frac{V}{2}}\eta(b_{i,m})B^{(\langle ij\rangle)}}\right]\right)^2 \ . \qquad (2.19)
\end{aligned}
$$

The constant factor is a complex number and can be taken out of the trace. The remaining is equivalent to the determinant of the given quantity, where $\boldsymbol{I}$ is the unity matrix and T, $A^{(i)}$ and $B^{(\langle ij\rangle)}$ are matrices that are defined by the following relations:

$$
H_t = \sum_{\langle ij\rangle,\sigma} c^{\dagger}_{i\sigma} T_{ij} c_{j\sigma} \ , \qquad (2.20)
$$

$$
H_U^{(i)} = \frac{\bar{U}}{2}\left(\sum_{\sigma}\left[c^{\dagger}_{i\sigma}A^{(i)}c_{i\sigma} - \frac{1}{2}\right]\right)^2 \ , \qquad (2.21)
$$

$$
H_V^{(\langle ij\rangle)} = \frac{V}{2}\left(\sum_{\sigma}\left[\begin{pmatrix} c^{\dagger}_{i\sigma} \\ c^{\dagger}_{j\sigma}\end{pmatrix} \cdot B^{(\langle ij\rangle)} \begin{pmatrix} c_{i\sigma} \\ c_{j\sigma}\end{pmatrix} - 1\right]\right)^2 \qquad (2.22)
$$

In total the partition function is given by

$$
\begin{aligned}
Z &= \operatorname{Tr} \mathrm{e}^{-\beta H} \\
&= \sum_C \left(\prod_{m=1}^{L_T}\prod_{i=1}^{N}\gamma(a_{i,m})\gamma(b_{i,m})\right) \mathrm{e}^{-\sum_m\sum_i\sqrt{-\Delta\tau\frac{\bar{U}}{2}}\eta(a_{i,m})} \mathrm{e}^{-2\sum_m\sum_{\langle ij\rangle}\sqrt{-\Delta\tau\frac{V}{2}}\eta(b_{i,m})} \times \\
&\left(\det\left[\boldsymbol{I} + \prod_m \underbrace{\mathrm{e}^{-\Delta\tau T} \prod_i \mathrm{e}^{\sqrt{-\Delta\tau\frac{\bar{U}}{2}}\eta(a_{i,m})A^{(i)}} \prod_{\langle ij\rangle} \mathrm{e}^{\sqrt{-\Delta\tau\frac{V}{2}}\eta(b_{i,m})B^{(\langle ij\rangle)}}}_{=:B_m^C}\right]\right)^2 + \mathcal{O}(\Delta\tau^2) \\
&\equiv \sum_C \xi(C)\mathrm{e}^{-S(C)} + \mathcal{O}(\Delta\tau^2) \ . \qquad (2.23)
\end{aligned}
$$

From this formulation one can see where the name *determinant* QMC originates. B_m^C is a useful definition that will be used in the following. Summing over the configuration space yields, under certain conditions, a real and positive number: with the definition of the values of the HS fields and for vanishing chemical potential μ (as well as non-frustrated lattices) the individual summands come in complex conjugate pairs, such that the imaginary parts cancel, while the real part is greater zero. In the doped case $\mu \neq 0$, some configuration weights will become negative. Although a sign problem, which is model and regime dependent, is present it is possible to quantify its severity and gain physical information about the system's state [61].

Being able to sample the partition function, we can measure expectation values of observables at finite temperatures as well as in the ground state at $T = 0$.

2.2.2 Finite Temperature DQMC

The quantity of interest is given by the expression

$$\langle O \rangle = \frac{1}{Z}\mathrm{Tr}\left(O\mathrm{e}^{-\beta H}\right) = \sum_C P_C \langle O \rangle_C + \mathcal{O}(\Delta\tau^2)\,, \tag{2.24}$$

where $P_C = \frac{\xi(C)\mathrm{e}^{-S(C)}}{\sum_C \xi(C)\mathrm{e}^{-S(C)}}$ and $\langle O \rangle_C$ is the expectation value of an observable O for a given HS field configuration C. Note that each field configuration is implicitly associated with an imaginary time slice.

The fact that we deal with non-interacting electrons allows us to employ Wick's theorem (see Sec. 2.2.4) by measuring the single particle Green's function. With this quantity we are able to calculate two-body correlation functions or scalar observables.

First, we introduce two imaginary time propagators:

$$U_C(\tau_2, \tau_1) = \prod_{m=m_1+1}^{m_2} \mathrm{e}^{-\Delta\tau \mathbf{c}^\dagger T \mathbf{c}} \mathrm{e}^{\mathbf{c}^\dagger V(C_m)\mathbf{c}} \mathrm{e}^{\mathbf{c}^\dagger \tilde{V}(C_m)\mathbf{c}} \tag{2.25}$$

$$B_C(\tau_2, \tau_1) = \prod_{m=m_1+1}^{m_2} \mathrm{e}^{-\Delta\tau T} \mathrm{e}^{V(C_m)} \mathrm{e}^{\tilde{V}(C_m)} = \prod_{m=m_1+1}^{m_2} B_m^C\,, \tag{2.26}$$

with $\tau_i = m_i \Delta\tau$. With these definitions the expectation value in Eq. (2.24) reads

$$P_C = \frac{\gamma(C)\mathrm{e}^{-S(C)}\det\left(\boldsymbol{I} + B_C(\beta, 0)\right)}{\sum_C \gamma(C)\mathrm{e}^{-S(C)}\det\left(\boldsymbol{I} + B_C(\beta, 0)\right)} \tag{2.27}$$

$$\langle O \rangle_C = \frac{\mathrm{Tr}\left(U_C(\beta, \tau)\, O\, U_C(\tau, 0)\right)}{\mathrm{Tr}\, U_C(\beta, 0)}\,. \tag{2.28}$$

The expectation value for a given configuration $\langle O \rangle_C$ is computed from the discretization of the same continuous quantity

$$\begin{aligned}\langle O \rangle_C &= \frac{1}{Z}\mathrm{Tr}\left(\mathrm{e}^{-\beta H}\mathrm{e}^{\tau H} O\, \mathrm{e}^{-\tau H}\right)\\ &= \frac{1}{Z}\mathrm{Tr}\left(\mathrm{e}^{-(\beta-\tau)H} O\, \mathrm{e}^{-(\tau-0)H}\right)\\ &\approx \frac{1}{Z}\mathrm{Tr}\left(U_C(\beta, \tau)\, O\, U_C(\tau, 0)\right)\,. \end{aligned} \tag{2.29}$$

With $\mathrm{Tr}\,(U_C(\beta,0)) = \det\,(\boldsymbol{I} + B_C(\beta,0))$ we can evaluate $\langle O\rangle_C$ in terms of the matrices $B_C(\tau_2,\tau_1)$ for a single-body operator $O = \mathbf{c}^\dagger X \mathbf{c}$ in the following way:

$$\begin{aligned}
\langle O\rangle_C &= \frac{\partial}{\partial\alpha} \ln \mathrm{Tr}\left(U_C(\beta,\tau)\mathrm{e}^{\alpha O} U_C(\tau,0)\right)\Big|_{\alpha=0} \\
&= \frac{\partial}{\partial\alpha} \ln \det\left(\boldsymbol{I} + B_C(\beta,\tau)\mathrm{e}^{\alpha O} B_C(\tau,0)\right)\Big|_{\alpha=0} \\
&= \frac{\partial}{\partial\alpha} \mathrm{Tr}\ln\left(\boldsymbol{I} + B_C(\beta,\tau)\mathrm{e}^{\alpha O} B_C(\tau,0)\right)\Big|_{\alpha=0} \\
&= \mathrm{Tr}\left(\frac{B_C(\beta,\tau)\, O\, B_C(\tau,0)}{\boldsymbol{I} + B_C(\beta,\tau) B_C(\tau,0)}\right) \\
&= \mathrm{Tr}\left(B_C(\tau,0)(\boldsymbol{I} + B_C(\beta,0))^{-1} B_C(\beta,\tau)\, O\right) \\
&= \mathrm{Tr}\left[\left(\boldsymbol{I} - (\boldsymbol{I} + B_C(\tau,0)B_C(\beta,\tau))^{-1}\right) O\right] \, . \qquad (2.30)
\end{aligned}$$

In particular, the equal time (Matsubara) Green's function is computed with above procedure for $O = c_x c_y^\dagger = \delta_{xy} - \mathbf{c}^\dagger A^{(yx)}\mathbf{c}$, where the subscript x or y is a super index for a lattice site and spin (i,σ) and $A^{(yx)}_{ab} = \delta_{ay}\delta_{bx}$. The Green's function on a time slice τ is given by

$$G_C(\tau)_{xy} = \langle c_x(\tau) c_y^\dagger(\tau)\rangle_C = (\boldsymbol{I} + B_C(\tau,0)B_C(\beta,\tau))^{-1}_{xy} \, . \qquad (2.31)$$

Although unequal time observables will not be considered in any project of this thesis, the calculation of the unequal time Green's function is mentioned for completeness. The derivation is analogous to the one above:

$$G_C(\tau_1,\tau_2)_{xy} = \langle T c_x(\tau_1) c_y^\dagger(\tau_2)\rangle_C = \begin{cases} \langle c_x(\tau_1) c_y^\dagger(\tau_2)\rangle_C & ,\text{if } \tau_1 \geq \tau_2 \\ -\langle c_y^\dagger(\tau_2) c_x(\tau_1)\rangle_C & ,\text{if } \tau_1 < \tau_2 \end{cases} , \qquad (2.32)$$

where T denotes the time ordering operator. For $\tau_1 > \tau_2$ the computation results in

$$\langle c_x(\tau_1) c_y^\dagger(\tau_2)\rangle_C = \frac{\mathrm{Tr}\left(U_C(\beta,\tau_1)\, c_x\, U_C(\tau_1,\tau_2)\, c_y^\dagger\, U_C(\tau_2,0)\right)}{\mathrm{Tr}\,(U_C(\beta,0))} \qquad (2.33)$$

$$\Rightarrow\; G_C(\tau_1,\tau_2)_{xy} = [B_C(\tau_1,\tau_2) G_C(\tau_2,\tau_2)]_{xy} \, . \qquad (2.34)$$

A similar calculation for $\tau_1 < \tau_2$ yields

$$G_C(\tau_1,\tau_2)_{xy} = -\left[(\boldsymbol{I} - G_C(\tau_1,\tau_1)\, B_C^{-1}(\tau_2,\tau_1))\right]_{xy} \, . \qquad (2.35)$$

We find that the computation of the unequal time Green's functions boils down to the knowledge of the equal time Green's function. Unequal time observables can be used to access experimentally measurable quantities like the DOS by analytically continuating the Green's function from imaginary time to real time, e.g., with the maximum entropy method [62].

2.2.3 Projective DQMC

For the analysis of ground state properties the projective approach is the method of choice. The prerequisite for the application is to propose a trial wavefunction $|\psi_T\rangle$ that is non-orthogonal to the unknown, true ground state $|\psi_0\rangle$:

$$\langle\psi_t|\psi_0\rangle \neq 0\,. \tag{2.36}$$

The ground state expectation value of an observable O is given by the projection of the trial wavefunction along the imaginary time

$$\frac{\langle\psi_0|O|\psi_0\rangle}{\langle\psi_0|\psi_0\rangle} = \lim_{\theta\to\infty} \frac{\langle\psi_T|\mathrm{e}^{-\theta H}\mathrm{e}^{-(\beta-\tau)H}O\,\mathrm{e}^{-\tau H}\mathrm{e}^{-\theta H}|\psi_T\rangle}{\langle\psi_T|\mathrm{e}^{-(2\theta+\beta)H}|\psi_T\rangle}\,, \tag{2.37}$$

with β defining the range in imaginary time where observables are measured after carrying out a large number of projections θ to guarantee convergence to the ground state and τ varies from 0 to β for time-displaced observables, i.e., for equal-time observables the expectation value is τ-independent.

For an implementation of the algorithm we require the trial wavefunction of N_p particles to be a Slater determinant characterized by a matrix P

$$|\psi_T\rangle = \prod_{\sigma=\uparrow,\downarrow}\prod_{n=1}^{N_p}\left(\sum_{i=1}^{N} c^\dagger_{i,\sigma}P_{i,n}\right)|0\rangle\;. \tag{2.38}$$

Since the trial wavefunction is expressed as a Slater determinant we can define a single-particle trial Hamiltonian, where the latter is the ground state. We consider the trial Hamiltonian

$$H_T = \sum_{\sigma=\uparrow,\downarrow}\sum_{i,j}^{N} c^\dagger_{i,\sigma}\,h_{i,j}\,c_{j,\sigma} \tag{2.39}$$

and draw the connection to the trial wavefunction through

$$P^\dagger h\,P = \mathrm{diag}(\epsilon_1,\dots,\epsilon_N)\,. \tag{2.40}$$

This means the trial wavefunction is completely characterized by the set of orthogonal vectors defining P.

To compute the expectation value we begin analogously to the finite temperature case

$$\frac{\langle\psi_0|O|\psi_0\rangle}{\langle\psi_0|\psi_0\rangle} = \sum_C P_C\langle O\rangle_C + \mathcal{O}(\Delta\tau^2)\,. \tag{2.41}$$

Here, the weights P_C and expectation values $\langle O \rangle_C$ are given by

$$\begin{aligned} P_C &= \frac{\gamma(C)\mathrm{e}^{-S(C)}\mathrm{det}(P^\dagger B_C(2\theta,0)\,P)}{\sum_C \gamma(C)\mathrm{e}^{-S(C)}\mathrm{det}(P^\dagger B_C(2\theta,0)\,P)}\,, \\ \langle O \rangle_C &= \frac{\langle \psi_T | U_C(2\theta,\theta)\,O\,U_C(\theta,0)|\psi_T\rangle}{\langle \psi_T | U_C(2\theta,0)|\psi_T\rangle}\,. \end{aligned} \tag{2.42}$$

Similar to the calculation of the equal time Green's function in Eq. (2.30) we obtain for the projective case

$$G_C(\theta)_{xy} = \langle c_x^\dagger c_y \rangle_C = \Big(\boldsymbol{I} - B_C(\theta,0)P(P^\dagger B_C(2\theta,0)P)^{-1}P^\dagger B_C(2\theta,\theta)\Big)_{xy} \tag{2.43}$$

and for completeness we mention the unequal time Green's function as well:

$$G_C\left(\theta+\frac{\tau}{2},\theta-\frac{\tau}{2}\right)_{xy} = \left[B_C\left(\theta+\frac{\tau}{2},\theta-\frac{\tau}{2}\right)G_C\left(\theta-\frac{\tau}{2}\right)\right]_{xy} \tag{2.44}$$

$$G_C\left(\theta-\frac{\tau}{2},\theta+\frac{\tau}{2}\right)_{xy} = -\left[\left(\boldsymbol{I}-G_C\left(\theta-\frac{\tau}{2}\right)\right)B_C^{-1}\left(\theta+\frac{\tau}{2},\theta-\frac{\tau}{2}\right)\right]_{xy} \tag{2.45}$$

2.2.4 Wick's Theorem

In the general case we consider thermodynamic expectation values of the form

$$\langle T[\zeta_1(\tau_1)\zeta_2(\tau_2)...\zeta_n(\tau_n)]\rangle\;, \tag{2.46}$$

where the $\zeta_\alpha(\tau_\alpha)$ are bosonic or fermionic creation/annihilation operators and T is the time ordering operator. Since we deal with non-interacting electrons, we may elegantly break down the above expectation value of the operator sequence into a much simpler form. To this end we define a contraction of two operators:

$$\overbracket{\zeta_\alpha(\tau)\zeta_{\alpha'}}(\tau') = \langle T[\zeta_\alpha(\tau)\zeta_{\alpha'}(\tau')]\rangle\,. \tag{2.47}$$

In particular we find

$$\overbracket{c_x(\tau_1)c_y^\dagger}(\tau_2) = \langle T[c_x(\tau_1)c_y^\dagger(\tau_2)]\rangle = G(\tau_1,\tau_2)_{xy} \tag{2.48}$$

and the main measurable quantity of the algorithm, the one-particle equal time Green's function, is given by

$$\overbracket{c_x(\tau)c_y^\dagger}(\tau) = \langle c_x(\tau)c_y^\dagger(\tau)\rangle = G(\tau)_{xy}\,. \tag{2.49}$$

To evaluate Eq. (2.46) Wick's theorem allows us to decompose this quantity into a sum over all possible fully contracted terms:

$$
\begin{aligned}
&\langle T[\zeta_1(\tau_1)\zeta_2(\tau_2)\ldots\zeta_n(\tau_n)]\rangle \\
&= \sum_{\text{pair combinations}} (\pm 1)^P \langle T\zeta_{p(1)}(\tau_{p(1)})\zeta_{p(2)}(\tau_{p(2)})\rangle \ldots \langle T\zeta_{p(n-1)}(\tau_{p(n-1)})\zeta_{p(n)}(\tau_{p(n)})\rangle \\
&= \wick{\c1 \zeta_1(\tau_1) \c1 \zeta_2(\tau_2) \c1 \zeta_3(\tau_3) \c1 \zeta_4(\tau_4) \ldots \c1 \zeta_{n-1}(\tau_{n-1}) \c1 \zeta_n(\tau_n)} \\
&+ \wick{\c1 \zeta_1(\tau_1) \c2 \zeta_2(\tau_2) \c2 \zeta_3(\tau_3) \c1 \zeta_4(\tau_4) \ldots \c1 \zeta_{n-1}(\tau_{n-1}) \c1 \zeta_n(\tau_n)} + \ldots \,,
\end{aligned} \tag{2.50}
$$

where $p(1)\ldots p(n)$ is any permutation of the indices $1\ldots n$ and P is the parity of these permutations. The crossing of contractions is defined as

$$
\wick{\c1 \zeta_1 \c2 \zeta_2 \c1 \zeta_3 \c2 \zeta_4} = \pm \wick{\c1 \zeta_1 \c1 \zeta_3 \c1 \zeta_2 \c1 \zeta_4} \;. \tag{2.51}
$$

For bosonic operators the parity equals always 1, because no sign change occurs for the exchange of two operators. A negative sign can only emerge for fermionic operators. This Wick decomposition yields only finite values for (i) an even number of operators n and (ii) an equal number of creation and annihilation operators.

A convenient way to express this decomposition for DQMC simulations reads

$$
\begin{aligned}
&\langle T[c^\dagger_{x_1}(\tau_1)c_{x'_1}(\tau_{x'_1})...c^\dagger_{x_n}(\tau_n)c_{x'_n}(\tau_{x'_n})]\rangle_C = \\
&\det \begin{bmatrix}
\langle T[c^\dagger_{x_1}(\tau_1)c_{x'_1}(\tau_{x'_1})]\rangle_C & \langle T[c^\dagger_{x_1}(\tau_1)c_{x'_2}(\tau_{x'_2})]\rangle_C & \cdots & \langle T[c^\dagger_{x_1}(\tau_1)c_{x'_n}(\tau_{x'_n})]\rangle_C \\
\langle T[c^\dagger_{x_2}(\tau_2)c_{x'_1}(\tau_{x'_1})]\rangle_C & \langle T[c^\dagger_{x_2}(\tau_2)c_{x'_2}(\tau_{x'_2})]\rangle_C & \cdots & \langle T[c^\dagger_{x_2}(\tau_2)c_{x'_n}(\tau_{x'_n})]\rangle_C \\
\vdots & \vdots & \ddots & \vdots \\
\langle T[c^\dagger_{x_n}(\tau_n)c_{x'_1}(\tau_{x'_1})]\rangle_C & \langle T[c^\dagger_{x_n}(\tau_n)c_{x'_2}(\tau_{x'_2})]\rangle_C & \cdots & \langle T[c^\dagger_{x_n}(\tau_n)c_{x'_n}(\tau_{x'_n})]\rangle_C
\end{bmatrix} .
\end{aligned} \tag{2.52}
$$

As an example we demonstrate the decomposition of the double occupancy $D_i = \langle n_{i\uparrow} n_{i\downarrow}\rangle$:

$$
\begin{aligned}
\langle n_{i\uparrow} n_{i\downarrow}\rangle &= \langle c^\dagger_{i\uparrow} c_{i\uparrow} c^\dagger_{i\downarrow} c_{i\downarrow}\rangle \\
&= \wick{\c1 c^\dagger_{i\uparrow} \c1 c_{i\uparrow} \c1 c^\dagger_{i\downarrow} \c1 c_{i\downarrow}} + \wick{\c1 c^\dagger_{i\uparrow} \c2 c_{i\uparrow} \c1 c^\dagger_{i\downarrow} \c2 c_{i\downarrow}} + \wick{\c1 c^\dagger_{i\uparrow} \c2 c_{i\uparrow} \c2 c^\dagger_{i\downarrow} \c1 c_{i\downarrow}} \\
&= \wick{\c1 c^\dagger_{i\uparrow} \c1 c_{i\uparrow} \c1 c^\dagger_{i\downarrow} \c1 c_{i\downarrow}} - \wick{\c1 c^\dagger_{i\uparrow} \c1 c^\dagger_{i\downarrow} \c1 c_{i\uparrow} \c1 c_{i\downarrow}} + \wick{\c1 c^\dagger_{i\uparrow} \c1 c_{i\downarrow} \c1 c_{i\uparrow} \c1 c^\dagger_{i\downarrow}} \\
&= \langle c^\dagger_{i\uparrow} c_{i\uparrow}\rangle \langle c^\dagger_{i\downarrow} c_{i\downarrow}\rangle = \bar{G}^2_{ii} \,,
\end{aligned} \tag{2.53}
$$

where $\bar{G}_{xy} = \delta_{xy} - G_{xy}$. The last two terms vanish, because the expectation of both processes is zero. Only contractions with similar spins remain. This manifests the independence of the one-particle Green's function on the spin degree of freedom.

2.2.5 Monte Carlo Sampling

At this point we obtained all ingredients to carry out a DQMC simulation that proceeds as follows:

(i) Initiate a random HS field configuration for every site and bond.

(ii) Calculate the Green's function on time slice zero with

$$\begin{aligned} G_C(0) &= \left(\boldsymbol{I} + B_C(\beta, 0)\right)^{-1} \\ &= \left(\boldsymbol{I} + \prod_{m=1}^{L_T} B_m^C\right)^{-1} , \end{aligned} \tag{2.54}$$

for the finite-temperature method or correspondingly with Eq. (2.43) for the projective version.

(iii) To generate a Markov chain we adopt sequential flips of a local field component with probability 1/3. Accept the proposed configuration with probability $W(C \to C') = \min(1, R),\ R = P(C')/P(C)$ corresponding to the Metropolis scheme. In practice, we repeat this step a number of times equal to the number of lattice sites on every time slice.

(iv) Measure observables employing Wick's theorem.

(v) Propagate the Green's function to the next time slice with

$$G_C(\tau + \Delta\tau) = B_C(\tau + \Delta\tau, \tau) G_C(\tau) B_C^{-1}(\tau + \Delta\tau, \tau) \tag{2.55}$$

or, at appropriate points in imaginary time, stabilize it, i.e. recalculate the Green's function from scratch at the given time step like in step (ii). Instabilities arise from ill-conditioned matrices, where large scales suppress small scales in repeated matrix-matrix multiplications in the calculation of the Green's function. Because of the limited machine precision exponentially large round-off errors occur. To cure this problem we employ a QR-decomposition or a singular value decomposition of the matrices [63, 64]. However, the projective scheme does not suffer stabilization issues at any point.

(vi) Repeat the steps (ii)-(v) M times.

Additionally, we draw attention to a recent proposal on how to improve the sampling procedure in order to reduce statistical fluctuations on local quantities [65].

Reweighting and Sign problem

In general the configuration weight $P(C)$ is a complex number prohibiting a direct sampling of the transition probability $W(C \to C') = \min\left(1, \frac{P(C')}{P(C)}\right)$. This leads to the infamous fermionic sign problem. The sign problem is formulation and model dependent.

It has been shown that the sign problem is non-deterministic polynomial (NP) hard, which implies that a generic solution of the sign problem would solve all problems in the complexity class NP in polynomial time [66]. A hypothetical non-deterministic machine, in contrast to our current deterministic classical machines, could solve a NP problem in polynomial time. Finding a P algorithm for a NP decision problem, which would result in NP=P, seems impossible. In addition, it must be possible to confirm a result to a NP problem on a classical machine in polynomial time. Despite decades of research it is believed that NP $\neq$ P and no deterministic polynomial time algorithm exists, although the statement NP $\neq$ P is yet to be proven. This remains one of the unsolved millennium problems.

The standard way of dealing with complex or negative weights is the following reweighting scheme. We expand the sum and find that the partition function for the considered Hubbard-type models is real

$$Z = \sum_C \xi(C)\mathrm{e}^{-S(C)} = \sum_C \left[\xi(C)\mathrm{e}^{-S(C)}\right]^* = \sum_C \mathrm{Re}\left[\xi(C)\mathrm{e}^{-S(C)}\right] \tag{2.56}$$

and with the definition of the sign of a configuration

$$\mathrm{sign}(C) = \frac{\mathrm{Re}\left[\xi(C)\mathrm{e}^{-S(C)}\right]}{\left|\mathrm{Re}\left[\xi(C)\mathrm{e}^{-S(C)}\right]\right|}\ , \tag{2.57}$$

the expectation value is rewritten into

$$\begin{aligned}
\langle O\rangle &= \frac{\sum_C \xi(C)\mathrm{e}^{-S(C)}\langle O\rangle_C}{\sum_C \xi(C)\mathrm{e}^{-S(C)}} \\
&= \frac{\sum_C \mathrm{Re}\left[\xi(C)\mathrm{e}^{-S(C)}\right] \frac{\xi(C)\mathrm{e}^{-S(C)}}{\mathrm{Re}\left[\xi(C)\mathrm{e}^{-S(C)}\right]}\langle O\rangle_C}{\sum_C \mathrm{Re}\left[\xi(C)\mathrm{e}^{-S(C)}\right]} \\
&= \frac{\left(\sum_C \left|\mathrm{Re}\left[\xi(C)\mathrm{e}^{-S(C)}\right]\right| \mathrm{sign}(C)\frac{\xi(C)\mathrm{e}^{-S(C)}}{\mathrm{Re}\left[\xi(C)\mathrm{e}^{-S(C)}\right]}\langle O\rangle_C\right) / \sum_C \left|\mathrm{Re}\left[\xi(C)\mathrm{e}^{-S(C)}\right]\right|}{\left(\sum_C \left|\mathrm{Re}\left[\xi(C)\mathrm{e}^{-S(C)}\right]\right| \mathrm{sign}(C)\right) / \sum_C \left|\mathrm{Re}\left[\xi(C)\mathrm{e}^{-S(C)}\right]\right|} \\
&= \frac{\langle \mathrm{sign}\frac{\xi\mathrm{e}^{-S}}{\mathrm{Re}[\xi\mathrm{e}^{-S}]}\langle O\rangle\rangle_{\bar{P}}}{\langle \mathrm{sign}\rangle_{\bar{P}}}\ ,
\end{aligned} \tag{2.58}$$

where $\bar{P} = \frac{\left|\mathrm{Re}\left[\xi(C)\mathrm{e}^{-S(C)}\right]\right|}{\sum_C \mathrm{Re}\left[\xi(C)\mathrm{e}^{-S(C)}\right]}$ and $\langle \mathrm{sign}\rangle_{\bar{P}} \in \mathbb{R}$. This allows to measure observables even with negative transition weights. However, the configurations with negative and positive sign nearly cancel each other, so that $\langle \text{sign} \rangle_{\bar{P}}$ decays exponentially to zero with increasing system size N and inverse temperature β. We can see this by considering the average sign as the ratio of the partition function of the fermionic system $Z = \sum_C \xi(C) \mathrm{e}^{-S(C)}$ and the corresponding bosonic system $Z' = \sum_C \left| \xi(C) \mathrm{e}^{-S(C)} \right|$. As the partition functions are exponentials of the corresponding free energies, this ratio is an exponential of the free energy density difference Δf

$$\langle \text{sign} \rangle = \frac{Z}{Z'} \propto \mathrm{e}^{-\beta N \Delta f} \; . \tag{2.59}$$

Consequentially, the relative error on the average sign increases exponentially with increasing particle number and inverse temperature:

$$\begin{aligned} \frac{\sigma_{\langle \text{sign} \rangle}}{\langle \text{sign} \rangle} &= \frac{\sqrt{\left(\langle \text{sign}^2 \rangle - \langle \text{sign} \rangle^2 \right) / M}}{\langle \text{sign} \rangle} \\ &= \frac{\sqrt{1 - \langle \text{sign} \rangle^2}}{\sqrt{M} \langle \text{sign} \rangle} \\ &\propto \frac{\mathrm{e}^{\beta N \Delta f}}{\sqrt{M}} \; , \end{aligned} \tag{2.60}$$

where M is the number of MC samples and $\Delta f > 0$. If a sign problem is present, for instance for $\mu \neq 0$ in the case of the U-V model, the relative error on the average sign and thus on the measurement increases exponentially with increasing system size and inverse temperature [66, 67].

2.3 Stochastic Series Expansion

Starting with Hubbard-type models and drastically increasing the local interaction, so that $U \gg t$, we find the Heisenberg model to be an effective description for the residual spin physics. We could continue simulating the high-U regime with DQMC, however, the stochastic series expansion (SSE) is perfectly tailored to compute thermodynamic properties of the spin-1/2 Heisenberg model [23–25]. It is based on a high-temperature series expansion of the partition function. The sampling of the partition function is enabled through the Monte Carlo scheme.

This method is not solely limited to spin-1/2 Heisenberg Hamiltonians, but has been applied to higher spin models as well [68]. The simulations have been successfully performed on a distinct range of lattices including frustrated systems [26–29, 69], models with long-range interactions [70], hard-core and soft-core boson Hamiltonians [71–73] and generalized SU(N) symmetric models [74, 75] making a connection to field-theoretic studies of quantum phase transitions and universality [76, 77], among others.

We adapt this section from the profound introduction of the SSE in [23, 25] with the addition of directed loop updates [78, 79].

2.3.1 Series Expansion of the Partition Function

We demonstrate the SSE method on the example of the Heisenberg model without external magnetic field:

$$\begin{aligned} H &= J \sum_{\langle i,j \rangle} \left(S_i^x S_j^x + S_i^y S_j^y + S_i^z S_j^z \right) \\ &= \frac{J}{2} \sum_{\langle i,j \rangle} \left(S_i^+ S_j^- + S_i^- S_j^+ + 2 S_i^z S_j^z \right) . \end{aligned} \tag{2.61}$$

The second line is a consequence of the definition of the spin ladder operators $S_i^{\pm} = S_i^x \pm \mathrm{i} S_i^y$ and $J > 0$ describes an antiferromagnet, whereas $J < 0$ describes a ferromagnet. The sum runs over nearest neighbor sites or bonds, respectively.
We want to expand the quantum partition function for small inverse temperatures $\beta = 1/T$:

$$\begin{aligned} Z &= \mathrm{Tr} \left(\mathrm{e}^{-\beta H} \right) = \sum_{\{|\alpha\rangle\}} \langle \alpha | \mathrm{e}^{-\beta H} | \alpha \rangle \\ &= \sum_{\{|\alpha\rangle\}} \sum_{n=0}^{\infty} \frac{(-\beta)^n}{n!} \langle \alpha | H^n | \alpha \rangle , \end{aligned} \tag{2.62}$$

where H is the Hamiltonian of our lattice spin system and the set $\{|\alpha\rangle\}$ spans an orthonormal basis of the Hilbert space of H with

$$|\alpha\rangle = |\alpha_1\rangle \otimes |\alpha_2\rangle \otimes \cdots \otimes |\alpha_N\rangle , \tag{2.63}$$

where the index denotes the site number. For instance, we take the tensor product of the eigenstates of the local S_i^z operators $|\alpha\rangle = |s_1^z, s_2^z, \ldots, s_N^z\rangle$. To evaluate the occurring matrix elements we decompose the Hamiltonian into bond operators

$$H = -\sum_{a,b} h_{a,b} , \tag{2.64}$$

with $b = (i, j)$ labeling the bond consisting of sites i and j and a denoting the operator type. A bond operator can be of a diagonal Ising type interaction or an off-diagonal spin-flip operator type with respect to the S^z-basis

$$h_{1,b(i,j)} = S_i^z S_j^z - \epsilon \tag{2.65}$$

$$h_{2,b(i,j)} = S_i^+ S_j^- + S_i^- S_j^+ \,. \tag{2.66}$$

We add the constant ϵ to ensure that the diagonal matrix elements are positive. Furthermore, on a bipartite lattice, we perform a rotation on one sublattice transforming $S_i^\pm \to (-1)^i S_i^\pm$ for positive weights. For a well defined probability weight we have to introduce a restriction on the chosen basis states. We require the action of the bond operators $h_{a,b}$ on the states $|\alpha\rangle$ to be non-branching:

$$h_{a,b}\,|\alpha\rangle \propto |\alpha'\rangle \quad , |\alpha\rangle\,, |\alpha'\rangle \in \{|\alpha\rangle\}\,. \tag{2.67}$$

This means that the bond operators map each pure state $|\alpha\rangle$ onto another pure state $|\alpha'\rangle$ in the Hamiltonian's Hilbert space. With this decomposition the powers of the Hamiltonian can be written as

$$(H)^n = \left(-\sum_{a,b} h_{a,b}\right)^n = \sum_{\{S_n\}} (-1)^n \prod_i^n h_{a_i,b_i}\,, \tag{2.68}$$

where $\{S_n\} = \{[a_1, b_1], [a_2, b_2], \ldots, [a_n, b_n]\}$ are all product sequences of bond operators called the "operator string". Inserting this expression in the partition function's trace we obtain

$$Z = \sum_{n=0}^{\infty} \sum_{\{S_n\}} \sum_{\{|\alpha\rangle\}} \frac{\beta^n}{n!} \langle\alpha| \prod_i^n h_{a_i,b_i} |\alpha\rangle \ . \tag{2.69}$$

Analogously, for the expectation value of an operator O we get

$$\langle O\rangle = \frac{1}{Z} \sum_{n=0}^{\infty} \frac{\beta^n}{n!} \sum_{\{S_n\}} \sum_{\{|\alpha\rangle\}} \langle\alpha| O \prod_i^n h_{a_i,b_i} |\alpha\rangle \ . \tag{2.70}$$

Expansion Cut-Off

For numerical implementations it is impractical to work with variable length or infinite series expansions. To be able to implement the method we truncate the fluctuating expansion order by

$$L \gg \langle n\rangle \propto N\beta\,, \tag{2.71}$$

where L is a fixed upper bound, N the system size and $\beta = 1/T$ the inverse temperature. We have to ensure that we do not truncate too early so that this systematic error due to a finite expansion is much smaller than the statistical error in the Monte Carlo scheme. In practice, large system sizes sharpen the expansion order's distribution around its average so that $L \approx 2\langle n\rangle$ is sufficient. Since we fix the operator string length by the number bigger than its average, we have to fill the $(L-n)$ vacancies with identity operators $\boldsymbol{I} \equiv h_{0,0}$. There are $\binom{L}{n}$ spots to insert these identity operators, which have to be accounted for in the partition function:

$$Z = \sum_{\{S_L\}} \sum_{\{|\alpha\rangle\}} \frac{\beta^n}{n!\binom{L}{n}} \langle\alpha| \prod_{i}^{L} h_{a_i,b_i} |\alpha\rangle \ . \tag{2.72}$$

In the above equation the number of non-identity operators n is implicitly calculated through the amount of inserted identity operators $h_{0,0}$ and the truncation order L.

In the evaluation of the partition function the next step is to calculate the action of the operator string on the basis states. Therefore, we introduce the concept of a propagated state

$$|\alpha(p)\rangle \propto \left(\prod_{i=1}^{p} h_{a_i,b_i}\right) |\alpha(0)\rangle \ , \tag{2.73}$$

where $|\alpha(0)\rangle = |\alpha\rangle$ is the initial state. With the non-branching property of the bond operators, $|\alpha(p)\rangle$ is always a pure state. Furthermore, we assume the propagated states to be normalized. For finite system sizes the series index p does not correspond precisely to imaginary time, but represents a distribution of the latter, so that it is appropriate to refer to the p-space as imaginary time-space.

Finally, we obtain a form of the partition function that can be efficiently sampled

$$Z = \underbrace{\sum_{\{S_L\}} \sum_{\{|\alpha\rangle\}}}_{=\sum_C} \underbrace{\frac{\beta^n (L-n)!}{L!} \prod_{p=1}^{L} \langle\alpha(p)| h_{a_p,b_p} |\alpha(p-1)\rangle}_{=P(\alpha,S_L)=P_C} = \sum_C P_C \, , \tag{2.74}$$

where due to periodicity of the trace the boundary condition $|\alpha(0)\rangle = |\alpha(L)\rangle$ holds. A state propagated by the operator string needs to return to its initial composition of local states. Thus, a configuration in the SSE is given by a combination of a state $|\alpha\rangle$ and an operator string S_L.

2.3.2 Observables

We focus on observables relevant to this thesis, which do not represent a complete list of measurable quantities in the SSE. For observables diagonal in the computational basis, such as the magnetization $m = \sum_i s_i^z$ and its higher moments, we calculate the expectation value straight forward:

$$\langle O\rangle = \frac{1}{Z} \mathrm{Tr}\, O \mathrm{e}^{-\beta H} = \sum_{\{S_L\}} \sum_{\{|\alpha\rangle\}} P(\alpha, S_L) \, \langle\alpha|O|\alpha\rangle = \sum_C P_C \langle O\rangle_C \, . \tag{2.75}$$

By averaging over all possible insertion position of the operator we can improve the statistics:

$$\langle O\rangle = \sum_{\{S_L\}}\sum_{\{|\alpha\rangle\}}\frac{1}{n}\sum_{p=1}^{n} P(\alpha, S_L)\,\langle \alpha(p)|O|\alpha(p)\rangle\ . \tag{2.76}$$

However, non-diagonal observables can be computed as well.
Considering the expectation value of the system's energy

$$\langle H\rangle = E = -\frac{\partial}{\partial\beta}\log(Z)\,, \tag{2.77}$$

we see that the partial derivative can be carried out explicitly in Eq. (2.74). The additive constant to the diagonal bond operators ϵ has to be subtracted again yielding

$$E = -\frac{1}{\beta}\langle n\rangle - N_b\epsilon\,, \tag{2.78}$$

where N_b denotes the total number of bonds. We find a connection between the energy and the mean expansion order. Similarly we find for the specific heat

$$\begin{aligned} C &= \frac{\partial E}{\partial T} = \frac{\partial\beta}{\partial T}\frac{\partial E}{\partial\beta} \\ &= \langle n^2\rangle - \langle n\rangle^2 - \langle n\rangle\,. \end{aligned} \tag{2.79}$$

With above approach one can compute higher moments of the energy $\langle H^m\rangle$.
In the same manner we can measure only parts of the Hamiltonian, namely single bond operators. Extending this to products of these operators allows the measurement of correlations of the form

$$\langle h_{a,b}h_{a',b'}\rangle = T^2\langle (n-1)n_{a,b,a',b'}\rangle\,, \tag{2.80}$$

where $n_{a,b,a',b'}$ is the number of adjacent operator pairs in the operator string. An important application are the bond correlations $\vec{S}_i\cdot\vec{S}_j$. They are not diagonal in the computational basis, but their correlation $\langle\left(\vec{S}_i\cdot\vec{S}_j\right)\left(\vec{S}_{i'}\cdot\vec{S}_{j'}\right)\rangle$ can be referred to the bond operators $h_{1,b(i,j)}$ and $h_{2,b(i,j)}$.
Furthermore, the system's response to small perturbations (incorporated via $\tilde{H} = H + hB$)

$$\chi_{AB} = \frac{\partial\langle A\rangle_{\tilde{H}}}{\partial h}\,, \tag{2.81}$$

where A is the observable which response we consider and B the perturbing operator mediated by the strength h. Employing linear response theory, we evaluate these functions with the Kubo formula

$$\chi_{AB} = \int_0^\beta \mathrm{d}\tau\langle A(\tau)B(0)\rangle - \beta\langle A\rangle\langle B\rangle\,, \tag{2.82}$$

where $A(\tau) = \mathrm{e}^{-\tau H} A \mathrm{e}^{\tau H}$.

Sign-Problem

As any other QMC method the SSE is not spared by the notorious sign problem. We can do the same reweighting as we did for DQMC (see Sec. 2.2.5)

$$\langle O \rangle = \sum_C P_C \langle O \rangle_C = \frac{\langle O \,\mathrm{sign} \rangle}{\langle \mathrm{sign} \rangle} \,, \tag{2.83}$$

including only positive, real valued configuration weights $|P_C| \geq 0$ and absorbing the sign assigned to a configuration into the measured observable. What seems to be a promising circumvention of the sign problem, comes with an exponential numerical cost in the system's size N and inverse temperature β, cf. Eq. (2.60).
In the SSE the weight $P_C = P(\alpha, S_L)$ depends on the chosen basis $\{|\alpha\rangle\}$. For the diagonal operators we ensure a positive weight by adding a trivial constant and if the lattice can be decomposed such that it is bipartite, the off-diagonal operators are made positive by a spin-rotation on one of the sublattices. The problem arises when the lattice is frustrated. There is an odd number of off-diagonal operators contributing to the operator string S_L so that we obtain a net negative weight P_C. However, choosing a proper basis, like a dimer basis for frustrated spin ladders [80–84], one can eliminate the sign problem or at least improve it in certain models for a certain parameter range [85, 86].

2.3.3 Diagonal Update

For the Markov chain Monte Carlo process we have to efficiently update the configurations $C = C(|\alpha\rangle, S_L) \to C'$. These updates have to be ergodic in the configuration space and fulfill the detailed balance condition as described in Sec. 2.1.1.
We distinguish two alternating update schemes in the SSE described in this and the following sections. The diagonal update changes diagonal operators $h_{1,b}$ in the operator string S_L sequentially leaving the off-diagonal operators untouched. The boundary condition $|\alpha(0)\rangle = |\alpha(L)\rangle$ is trivially fulfilled since a diagonal operator never changes the state $|\alpha\rangle$. In particular, with certain probabilities we insert at uniform randomly chosen bonds $P(b_p) = 1/N_b$ a diagonal operator at the position of an identity operator or vice versa. There is only one unique way to remove a diagonal operator, to be precise to change a diagonal operator into an identity operator. However, there are N_b possible spots to insert

a diagonal operator. The respective probabilities are given by

$$P_{\text{insert}} = \min\left(1, \frac{N_b\beta \langle\alpha(p)|h_{1,b_p}|\alpha(p-1)\rangle}{L-n}\right) \tag{2.84}$$

$$P_{\text{remove}} = \min\left(1, \frac{L-n+1}{N_b\beta \langle\alpha(p)|h_{1,b_p}|\alpha(p-1)\rangle}\right) . \tag{2.85}$$

Detailed balance is fulfilled for a whole sweep, i.e. going from $p=1$ to $p=L$. However, on its own the diagonal update is not ergodic.

2.3.4 Graphical Configuration Representation

For the introduction of the off-diagonal updates it is instructive to represent the operator string in a certain diagram. We encode the product of matrix elements in the partition function Eq. (2.74) as a bidirectional linked-vertex list. Each vertex, which mathematically corresponds to the action of a bond operator on the current spin state $|\alpha(p)\rangle = h_{a,b(i,j)}\,|\alpha(p-1)\rangle$, consists of four legs and the operator type. The lower and upper two legs form the same bond in real space, while we perform one imaginary time step along the y-axis. The four possible vertices for the isotropic spin-1/2 Heisenberg model with the leg numbering convention is depicted in Fig. 2.1.

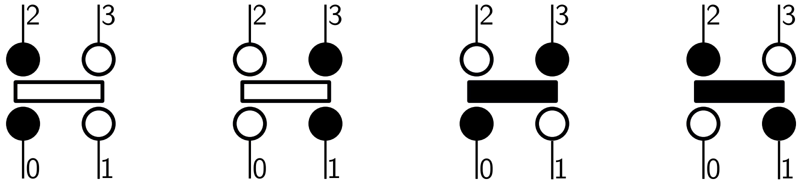

Figure 2.1: Allowed vertices for the spin-1/2 Heisenberg model. The solid(open) circles represent a local one-particle spin up(down) state and the solid(open) bar stands for a diagonal(off-diagonal) bond operator. Reading each vertex from bottom to top we pictorially show the action of both operator types on a bond in the propagated state $|\alpha(p)\rangle$.

An example of an 8 spin-chain SSE configuration is shown in Fig. 2.2. Constant spin states along the propagation direction are connected by straight lines, which we call bidirectional links (numerically pointers). The propagated states $|\alpha(p)\rangle$ are manipulated by the bond operators denoted as vertices in the space-time diagram, whereas the absence of a horizontal bar represents an identity operator. An SSE configuration is only valid if the propagation sequence is periodic, i.e. $|\alpha(0)\rangle = |\alpha(12)\rangle = |\alpha\rangle$.

This graphical representation will be essential in understanding the global off-diagonal update scheme introduced in the next section.

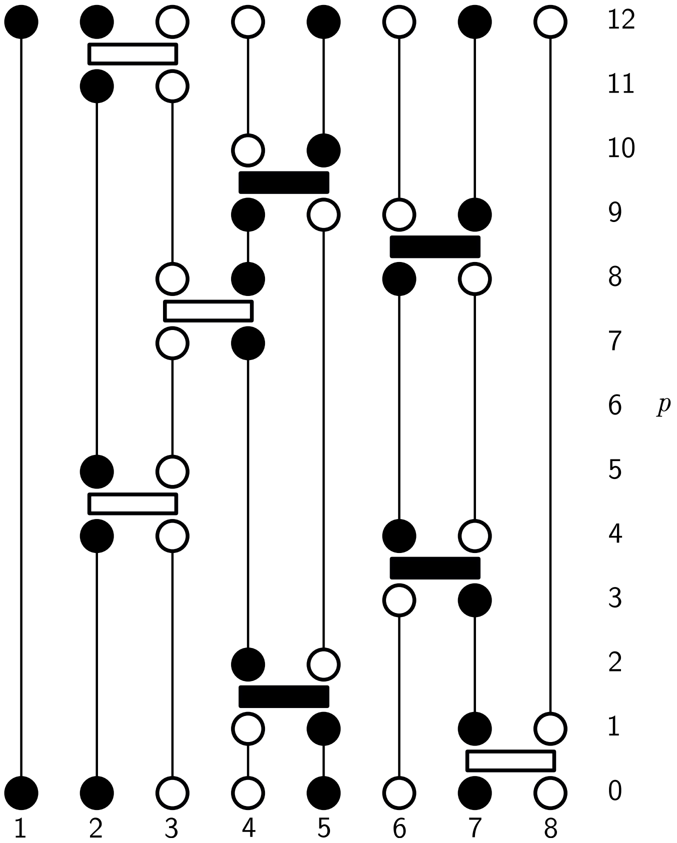

Figure 2.2: An 8 spin-chain SSE configuration adopted from [16]. Solid(open) bars indicate diagonal(off-diagonal) bond operators $h_{1,b}(h_{2,b})$ and solid(open) circles represent the one-particle spin state $|\uparrow\rangle(|\downarrow\rangle)$. The tensor product state $|\alpha\rangle$ is propagated from bottom to top, where no horizontal bar between states corresponds to a "fill-in" identity operator $h_{0,0}$.

2.3.5 Directed Loop-Update

The naive approach to execute an off-diagonal update would be changing an off-diagonal operator pair into diagonal ones and vice versa. At least two changes are necessary to maintain periodicity. In practice this can lead to low acceptance rates and other subtle issues. For better performance global operator-loop updates have been introduced for the SSE [25]. The major improvement is that the configuration weight only depends on the number of operators, which remains unchanged when flipping the loop. In general the performance is enhanced compared to local pair updates, especially in the presence of external fields. However, the loop update has to be tailored to certain models or parameter regimes, respectively, to maintain its efficiency. For instance, taking the spin-1/2 XXZ model

$$H = J \sum_{\langle i,j \rangle} \left(S_i^x S_j^x + S_i^y S_j^y + \Delta S_i^z S_j^z \right) - h \sum_i S_i^z \,, \tag{2.86}$$

with an uniaxial anisotropy Δ and external magnetic field h, it is known that the general formulation performs poorly at the Heisenberg point ($\Delta = 1, h = 0$) or the XY model point ($\Delta = 0, h = 0$), for which efficient schemes have been designed [78]. The latter are only applicable in these limiting cases.

Based on the operator-loop update we discuss a generalized formulation known as the directed loop update. As the name suggests the goal is to construct a closed loop by directed traversing through the space-time diagram. The global update is a series of local updates each fulfilling the detailed balance condition making it a "runtime" global updating scheme. To this end it has to obey certain rules.

Constructing a Closed Loop

To construct the loop we pick a random link in the linked-vertex list and introduce a discontinuity in the configuration at some imaginary time p and site i. We replace the local state $|\alpha_i(p)\rangle$ by two new, artificial states indicated by a square and an arrow in Fig. 2.3. In this abstract picture these states reside at intermediate positions of the discretized p-axis, so that we technically do not associate any physical meaning with them but a mathematical construction. However, these states are consistent within the space-time configuration. From the pair we specify the "tail", indicated by the square, to remain static and the "head", indicated by the arrow, to be able to move through the space-time diagram. On its trajectory, the head is allowed to change the local spin states, even in the initial state $|\alpha(0)\rangle$, and the operator type such that detailed balance and periodicity are fulfilled for any vertex update. At some point the head meets the tail and both annihilate creating a significant change to the configuration. The head moves freely along links in p-direction until it encounters a vertex through an entrance leg. The head leaves then the vertex through a randomly chosen exit leg. This scattering process leads to four scenarios shown in Fig. 2.4: (i) bounce and remain on the same link (which effectively does

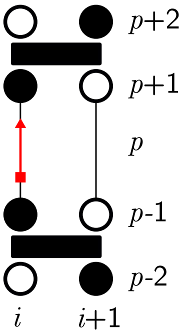

Figure 2.3: Discontinuity in the configuration space at site i and propagation level p. The local state $|\alpha_i(p)\rangle$ is replaced by two artificially constructed states. We indicate the static "tail" with a square and the dynamic "head" with an arrow.

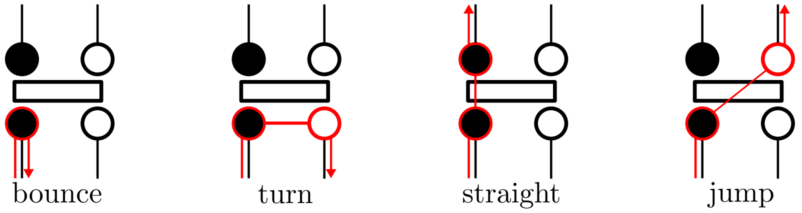

Figure 2.4: Head scattering on a vertex. The encounter of the head with a vertex leads to four scenarios labeled by the terms below the respective picture.

not contribute to an update), (ii) turn by jumping on the adjacent site in the bond and reverse the propagation direction, (iii) continue in a straight line and (iv) jump diagonally on the adjacent site on the state propagated on a level up or down and continue along the original direction. To stay consistent the head changes its spin state to the respective state

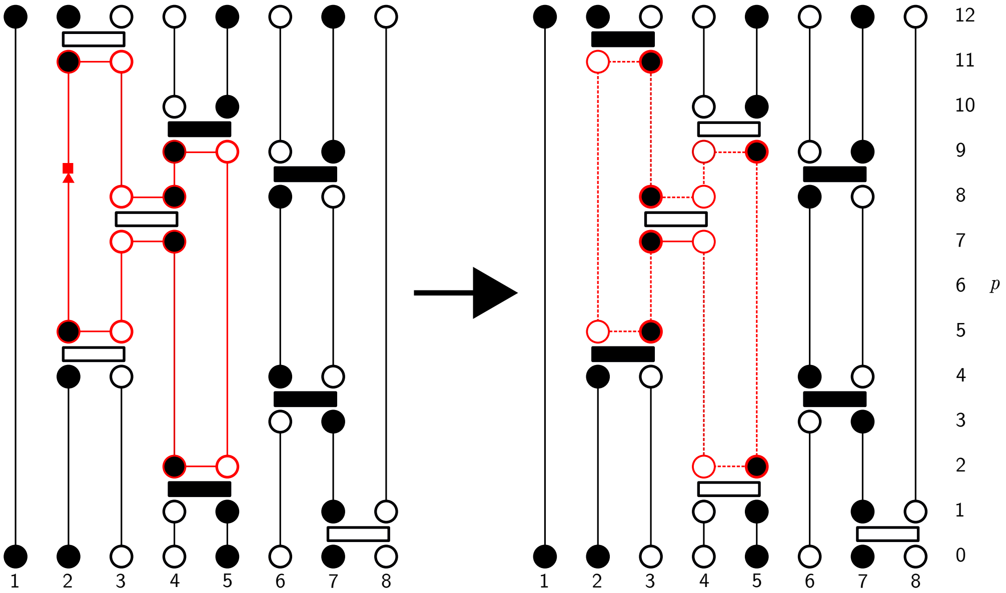

Figure 2.5: An SSE linked-vertex configuration with a directed-loop update. On the left the head-tail pair is introduced on the state $|\alpha_2(9)\rangle$ and is propagated upwards along the red contour. All the spins touched by the head are flipped and the operators in each vertex are changed from diagonal to off-diagonal and vice-versa. On the right the changes of the loop, indicated by the red dashed lines, are displayed forming a new configuration C'.

on the exit leg (we call it the exit state) and goes to the next vertex. The probability of a vertex update is calculated a-priori from a general set of directed-loop equations reviewed in the next paragraph. Furthermore, the head is allowed to change the local spin state on the links themselves. One can imagine the head carries in front of it an S_i^+ or S_i^- operator. In the case of spin-1/2 models the head suffices to be the linear combination $S_i^+ + S_i^-$. Technically, for spin-1/2 systems the tail can be understood as the same operator, so that

the system resides in an “extended space” or “extended ensemble”.
An example of a closed directed loop is shown in Fig. 2.5 on the left side and the new configuration with a remnant indication of the loop on the right side. The head-tail pair replaces the state $|\alpha_2(9)\rangle$ and is propagated upwards following the red contour. On its trajectory it flips the spins it touches with the appropriate operator switch, with no net change if a vertex is visited twice, until it meets the tail again and the loop is closed. We change the operators in the operator string S_L (and may also change the state $|\alpha\rangle$ if the head touches the periodic boundary) keeping the number of operators constant. The driving mechanism to change the operator number and with that the expansion order n is the diagonal update. One diagonal update is followed by a fixed number of loop updates N_L in each Monte Carlo step that is chosen such that on average every vertex is touched twice by the loops.

Directed-Loop Equation

As mentioned before, we need to calculate the probabilities of the head-vertex encounters for the different scenarios. To be precise, we mean the probability to choose the exit leg at each touched vertex. In the following we review equations for these probabilities, based on Ref. [78], which have been generalized in the derivations in Ref. [79].
Consider the head touching a vertex V_i. The state of the vertex, see Fig. 2.1 for our leg labeling convention, before the encounter is

$$\begin{aligned} |\Sigma_{b(i,j),p}\rangle &= |\sigma(0)\rangle \otimes |\sigma(1)\rangle \otimes |\sigma(2)\rangle \otimes |\sigma(3)\rangle \\ &= |\alpha_i(p-1)\rangle \otimes |\alpha_j(p-1)\rangle \otimes |\alpha_i(p)\rangle \otimes |\alpha_j(p)\rangle \ , \end{aligned} \tag{2.87}$$

where b denotes the bond and p the imaginary time level. With $\bar{\Sigma}_{b,p}$ we denote the vertex state after the head-vertex encounter having changed two states and the operator type. The two ingoing legs of a bond $b(i,j)$ are labeled 0 and 1, the outgoing ones 2 and 3. With this definition we can associate a weight to each vertex

$$\begin{aligned} W(\Sigma_{b,p}) &= \left(\langle\sigma(2)| \otimes \langle\sigma(3)|\right) h_{a_p,b_p} \left(|\sigma(0)\rangle \otimes |\sigma(1)\rangle\right) \\ &= \langle\alpha(p)|h_{a_p,b_p}|\alpha(p-1)\rangle \ , \end{aligned} \tag{2.88}$$

which is exactly the matrix element in Eq. (2.74). The head enters a vertex V_i from the leg l_i and exits it through l'_i, where $l = 0, 1, 2, 3$. Both states are changed and become $T_{i-1}\,|\sigma(l_i)\rangle$ and $T_i\,|\sigma(l'_i)\rangle$ with T_{i-1} being the operator carried by the head before the vertex encounter and T_i being the the operator after the first leg encounter. In our spin-1/2 case we can set $T = S^+ + S^-$ for each leg encounter and may drop the vertex index. However, we continue with the general notation. We define the conditional probability of exiting on leg l_i' given the entrance leg l_i (and the guarantee that the head exits the vertex) as

$$P(\Sigma_{b,p}, T_{i-1} \to T_i, l_i \to l_i') \text{ , with} \tag{2.89}$$

$$\sum_{l_i'} P(\Sigma_{b,p}, T_{i-1} \to T_i, l_i \to l_i') = 1 \,. \tag{2.90}$$

Originally it has been shown [25] that a generic solution for any model suffices

$$P(\Sigma_{b,p}, T_{i-1} \to T_i, l_i \to l_i') \propto W(\bar{\Sigma}_{b,p}) \,, \tag{2.91}$$

i.e. setting the exit probability proportional to the weight of the vertex after the head encounter, which is referred to as the heat bath solution. During the method's development it has been found that this choice is not optimal due to the bounce process [74, 78, 87]. It leads to undesired backtracking of the head's propagation. Another more efficient solution was required that minimizes or eliminates the probability of bounces. Now we face a set of equations for an optimization problem under the constraint to fulfill local detailed balance for each scattering:

$$\sum_{l_i'} W(\Sigma_{b,p}) P(\Sigma_{b,p}, T_{i-1} \to T_i, l_i \to l_i') = W(\Sigma_{b,p}) \,, \tag{2.92}$$

$$W(\Sigma_{b,p}) P(\Sigma_{b,p}, T_{i-1} \to T_i, l_i \to l_i') = W(\bar{\Sigma}_{b,p}) P(\bar{\Sigma}_{b,p}, T_i^\dagger \to T_{i-1}^\dagger, l_i' \to l_i) \,. \tag{2.93}$$

Further, one can introduce weights for the head (and tail) for a more general formulation that reduces bounces [79]. A proof of detailed balance can be found in App. A.2.1.

Loop measurement

The directed loop update adds another measurement technique to the list. In the extended ensemble we can measure correlation functions between the head and the tail. Equal time correlation functions are measured by counting the number of times the head on its trajectory crosses the imaginary time p, where the tail remained. This enables us in our example of an S^+ or S^- operator carried by the head to calculate correlations of the form $\langle S_i^s S_j^{s'} \rangle$ for $s, s' \in \{+, -\}$. We can generalize this concept to arbitrary local off-diagonal observables [29] and to non-equal time measurements [88].

With this we close the review of the two quantum Monte Carlo methods DQMC and SSE we use in this thesis and discuss aspects of post-processing numerical data the algorithms produce.

2.4 Data Processing

In general the statistical errors are model and observable dependent so that for strongly fluctuating measurements we require a very high number of MC sweeps. We define one sweep to be one measurement in configuration space $\langle O\rangle_C$, whenever that happens during the execution of the different algorithms. For a proper use of (quantum) Monte Carlo we need the procedure to be parallelized on CPU cores for reliable statistics. That means every CPU core executes a simulation independently, obtaining a set of measurements of estimators for the expectation value of observables, which are averaged over the number of parallel simulations. Typically, we average over the parallel measurements for each MC sweep to generate one data list for every observable.

Thermalization

Since we start every new simulation with a randomly generated configuration, it is highly unlikely to hit the high-weight configuration space region matching the current model parameters. Therefore, we let the algorithm do a certain amount of sweeps during which nothing is measured so that importance sampling leads the computation into the relevant region. This period is called *thermalization* or *equilibration*. In itself this is a non-trivial out-of-equilibrium process. The number of sweeps, which we call Monte Carlo time, necessary to be able to make equilibrium measurements is a-priori unknown. Instead of computing the exact (or an estimated) thermalization time, in practice, we fix it based on experience of repeated simulations.

Autocorrelation and Binning

For the formulas introduced in Sec. 2.1 to hold, we need the individual measurements $O(\vec{x}_i) \equiv O_i$ in the data sets to be uncorrelated. However, since one configuration in the consecutive Markov-chain process depends on its predecessor, a certain correlation during the measurements is naturally introduced. We call the separation of two configurations, which are sufficiently uncorrelated, the *autocorrelation time*. The autocorrelation can be quantified with the statistical error. Inserting the arithmetic mean $\langle O\rangle = \sum_{i=1}^{M} O_i$ in $\sigma_{\langle O\rangle^2} = \langle O^2\rangle - \langle O\rangle^2$, we get

$$\sigma^2_{\langle O\rangle} = \frac{1}{M^2}\sum_{i=1}^{M}\left(\langle O_i^2\rangle - \langle O_i^2\rangle^2\right) + \frac{1}{M^2}\sum_{i\neq j}^{M}\left(\langle O_i O_j\rangle - \langle O_i\rangle\langle O_j\rangle\right) , \tag{2.94}$$

where M is the total number of measurements. In the above equation we separate the diagonal part, which accounts for individual variances of uncorrelated data, from the off-diagonal part. The first term is independent of the measurement time i and yields $\sigma^2_{O_i}/M$.

The second term contains the correlations between the i-th and j-th measurement. For a perfectly uncorrelated data set the second term vanishes. In equilibrium we are guaranteed time-reversal symmetry $i \leftrightarrow j$, so that we can rearrange the terms into

$$\sigma^2_{\langle O \rangle} = \frac{1}{M} \left[\sigma^2_{O_i} + 2 \sum_{k=1}^{M} \left(\langle O_1 O_{1+k} \rangle - \langle O_1 \rangle \langle O_{1+k} \rangle \right) \left(1 - \frac{k}{M} \right) \right] . \tag{2.95}$$

We factor out $\sigma^2_{O_i}$ and obtain the closed form

$$\sigma^2_{\langle O \rangle} = \frac{\sigma^2_{O_i}}{M} 2\tau'_{O,\text{int}} , \tag{2.96}$$

with the *integrated* autocorrelation time

$$2\tau'_{O,\text{int}} = 1 + 2 \sum_{k=1}^{M} A(k) \left(1 - \frac{k}{M} \right) , \tag{2.97}$$

where

$$A(k) = \frac{\langle O_1 O_{1+k} \rangle - \langle O_1 \rangle \langle O_{1+k} \rangle}{\sigma^2_{O_i}} \xrightarrow{k \to \infty} \mathrm{e}^{-k/\tau_{O,\text{exp}}} \tag{2.98}$$

is the normalized autocorrelation function introducing the *exponential* autocorrelation time $\tau_{O,\text{exp}}$ giving an intuitive time scale. In a proper MC simulation $M \gg \tau_{O,\text{exp}}$ so that $k/\tau_{O,\text{exp}} \gg k/M$. Hence, for simplicity we omit the correction and write the integrated autocorrelation time as

$$2\tau_{O,\text{int}} = 1 + \sum_{k=1}^{M} A(k) . \tag{2.99}$$

The goal for a decent data analysis is to reduce the integrated autocorrelation time to 1. A naive error calculation would result in an underestimated statistical error on the mean value. The autocorrelation time is model and parameter dependent, e.g., it is higher close to second order phase transitions, and can be judged for every simulation by evaluating the autocorrelation function.

A convenient method to circumvent the correlation problem is the *binning* analysis. The original data set of M measurements is cast to M_B non-overlapping bins of length k, i.e. every bin is an average of k original measurements. We thus obtain a shortened data set

$$O_i^{(B)} = \frac{1}{k} \sum_{i=1}^{k} O_{(i-1)k+i} , \tag{2.100}$$

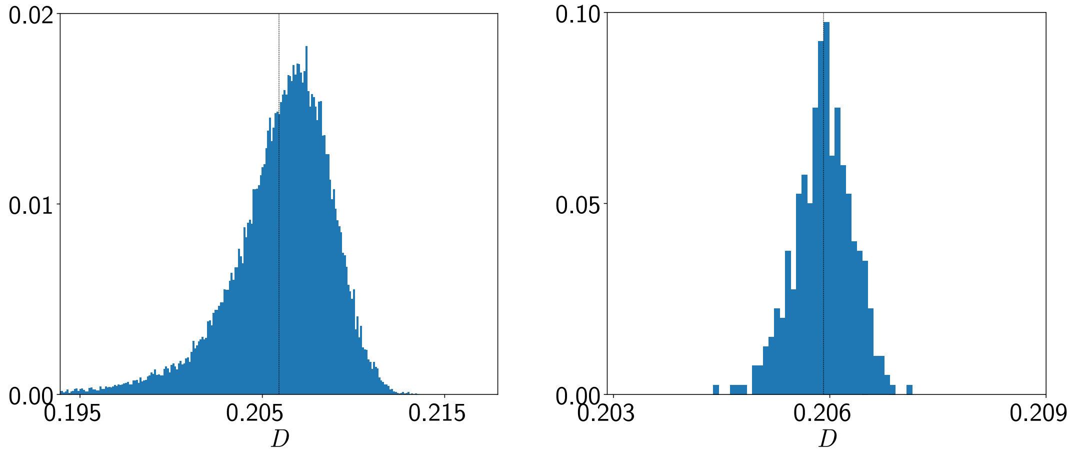

(a) Unbinned data

(b) Binned data, $k = 100$

Figure 2.6: Comparison of (a) unbinned and (b) binned data. The simulations have been carried out with the finite temperature DQMC scheme on a single CPU core for the U-V model on a 12×12 square lattice for $T/t = 0.19$, $U/t = 1.9$ and $V/t = 0.3$. The data consists of around 40000 equilibrated measurements of the double occupancy. The black vertical line indicates the arithmetic mean of the sample. The unbinned data (a) follows an unknown distribution so that the standard data analysis yields biased results. The binned data (b) shrinks the data set to 400 bins each averaged over 100 data points.

with $i = 1, \ldots, M_B$. For $k \gg \tau_{O,\text{int}}$ the bins are essentially uncorrelated. The standard estimator for the variance reads

$$\sigma^2_{\langle O\rangle} = \frac{\sigma^2_B}{M_B} = \frac{1}{M_B(M_B-1)} \sum_{i=1}^{M_B} \left(O_i^{(B)} - \langle O^{(B)} \rangle \right)^2 . \tag{2.101}$$

The binning procedure can be displayed by the distribution of the distinct measurements, as shown in Fig. 2.6. The histograms display the consecutive measurements of the double occupancy $D = \sum_i n_{i\uparrow} n_{i\downarrow}$ with the DQMC method of the U-V model. In the left panel we see how the unbinned data follows a non-symmetric distribution so that the arithmetic mean does not align visually with the expected peak. This originates from correlations in the Markov-chain. The cure is shown in the right panel, where we merge every 100 measurements into one bin. The resulting distribution is symmetric and our estimator for the expectation value fits to the Gaussian mean.

Jackknife-Resampling

Even if the bins are (sufficiently) uncorrelated, the problem of error propagation for quantities that are non-linear combinations of the Green's function (or other directly measured quantities) arises. To circumvent any bias in this case, we employ the *Jackknife* resampling

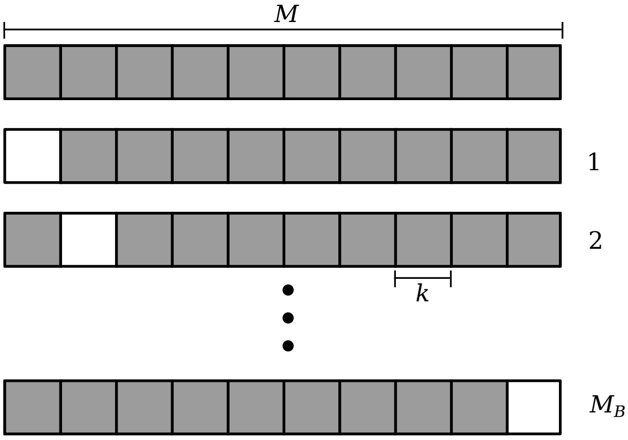

Figure 2.7: The first block shows the whole data set consisting of M measurement values split into $M_B = 10$ bins of length k. The second block ($i = 1$) and all consecutive ones represent the Jackknife blocks leaving out the blank bin.

scheme [89]. From the original bin set we form M_B Jackknife blocks $O_i^{(J)}$, containing all data but the i-th bin,

$$O_i^{(J)} = \frac{M\langle O\rangle - kO_i^{(B)}}{M-k}\,, \tag{2.102}$$

where $i = 1, \ldots, M_B$. Each Jackknife block consists of $M - k$ measured values, which is illustrated in Fig. 2.7. With this scheme we produce a data set of the same length as the original one. We average each "jackknifed" block, which results in a data set that scrambles the original set's information of an error estimate onto the new M_B data points and allows us to use the standard variance formula for any observable. For the estimation of non-linear combinations of basic quantities the bias is comparable to that of the total data set, since $\frac{1}{M-k} \gtrsim \frac{1}{M}$. The Jackknife blocks are trivially correlated, because the same sample is reused over and over again. This correlation is of a different nature than the one originating from the temporal dependence of the Markov-chain. Consequently, the Jackknife variance σ_J^2 will be smaller than the binning variance. However, this reduction can be corrected by multiplying $(M_B - 1)^2$ with Eq. (2.101) to obtain

$$\sigma^2_{\langle O\rangle} = \frac{M_B - 1}{M_B} \sum_{j=1}^{M_B} \left(O_j^{(J)} - \langle O^{(J)}\rangle\right)^2 \ . \tag{2.103}$$

Non-Local Interaction Extensions to the Hubbard Model

3

The Hubbard model is an intriguingly simple, yet rich model to study itinerant fermions in systems with narrow energy bands. The interplay between kinetic energy and the local on-site repulsion yields strong correlation effects. However, for theoretical studies of real materials with partially screened interactions we extend the pure local U-interaction to two cases: (i) nearest-neighbor interactions and (ii) long-range Coulomb (LRC) interactions. We perform large scale DQMC simulations within sign-problem free coupling regimes at finite temperatures, assess a recent study in terms of a first-order metal-to-insulator transition and propose a scenario to accommodate our findings.

The results in this chapter have been published in Ref. [1]. My contributions have been performing the DQMC simulations, carrying out the extrapolations and partially writing the manuscript. This project has been a continuation of my master's thesis. However, all results presented here have been obtained during my PhD time.

3.1 Motivation

Despite its apparent simplicity, to this day the two-dimensional Hubbard model [7–9], remains analytically unsolved in the thermodynamic limit. Nevertheless, it provides a rich ground for the study of fundamental phenomena in condensed matter physics. From the theoretical and computational side it is examined for instance with the numerical linked cluster expansion [90], dynamical cluster approximation [91], variational cluster approximation [92], diagrammatic determinant Monte Carlo [93] or cellular dynamical mean field theory [94], to name a few (see Ref. [43] for benchmarks from a wide range of numerical algorithms). During the exploration of its physical properties, its relevance to a wide breath of fundamental phenomena in condensed matter physics has been demonstrated, including the Mott-insulator transition, and the emergence of symmetry broken states, such as antiferromagnetism (AFM) or superconductivity (see Ref. [10] for a recent review). Furthermore, experimental realizations of this model have been demonstrated. By cold-atom optical trapping [95], experimental groups demonstrated fundamental properties like a superfluid-insulator transition in the Bose-Hubbard model [96], the Mott-insulator behavior of fermionic atoms [97], measurements of energetics and correlations [98, 99] and recently the AFM phase transition [100].

To account for the effects of the partially screened Coulomb interaction we add a nearest-neighbor or a long-range Coulomb interaction term, respectively, in addition to the local Hubbard-U. Non-local interactions are known to affect various quantities, for example the electronic band width [101, 102] or they can induce charge density wave states [103–107]. A recent study explored the effects of both above mentioned inter-site interaction types on the metal-to-insulator transition on the half-filled square lattice based on a variational approach [108, 109]. In detail, employing the Peierls-Feynmann-Bogoliubov variational principle, the extended Hubbard model was approximated in Ref. [109] by an effective local Hubbard model in terms of an effective hopping parameter $\tilde{t}$ and an effective local interaction strength $\tilde{U}$. Based on the integration of thermodynamic data for the effective local Hubbard model, obtained using DQMC simulations on a dense parameter grid, applying a two-dimensional Savitzky-Golay filter and spline interpolation to the grid data the variational free energy was calculated. Evaluating the results of this variational approach, several conclusions regarding the effects of non-local interactions were proposed. In particular, Ref. [109] describes two distinct mechanisms regarding the suppression of correlation effects by non-local interactions: The effective local repulsion $\tilde{U}$ is reduced within the Fermi-liquid regime, while the effective hopping amplitude $\tilde{t}$ is increased in the insulating regime. Furthermore, the competition between both effects was found to be the driving mechanism for a first-order metal-to-insulator transition in the presence of non-local interactions. From a comparison of available experimental data on materials with purely electronic metal-to-insulator transitions with the associated entropy jump across the transition, the authors conclude that non-local interactions are at least in part responsible for the discontinuous metal-to-insulator transitions observed in correlated electron materials. For a substantial conclusion, the results from the variational approach have to be compared to unbiased calculations that take the non-local interactions fully into account. Indeed, the parameter region in the vicinity of the proposed thermodynamic discontinuity is accessible to sign-problem free DQMC simulations. This means we are able to include a full treatment of the non-local interaction terms [50, 110].

3.2 Extended Hamiltonian

We consider the extended Hubbard model including non-local charge density interactions, described by the Hamiltonian

$$H = -t \sum_{\langle i,j \rangle, \sigma} \left(c^{\dagger}_{i\sigma} c_{j\sigma} + \text{h.c.} \right) + U \sum_{i} n_{i\uparrow} n_{i\downarrow} + \frac{1}{2} \sum_{i \neq j} V_{ij} n_i n_j \, . \tag{3.1}$$

Here, $c^{\dagger}_{i\sigma}$ ($c_{i\sigma}$) is the fermionic creation (annihilation) operator on site i with spin σ, $n_{i\sigma}$ the local spin resolved occupation operator and $n_i = n_{i\uparrow} + n_{i\downarrow}$ the total local occupation. Furthermore, t is the nearest-neighbor hopping strength, U is the local electron-electron repulsion and V_{ij} is the inter-site repulsion, which we define for (i) the nearest-neighbor case and (ii) the long-range Coulomb case as follows

$$V_{ij} = \begin{cases} V & \text{, for } i,j \text{ nearest} - \text{neighbors } (U{-}V\text{model}) \\ \frac{V_C}{d_{ij}} & \text{, for } i \neq j \text{ (LRC} - \text{model)} \end{cases} \, . \tag{3.2}$$

We examine the model on a square lattice with $N = L \times L$ sites with periodic boundary conditions in both directions and a lattice constant $a = 1$ at half-filling. For the long-range Coulomb case d_{ij} denotes the minimal distance of lattice sites i and j.

For our studies of the thermodynamic properties of the above introduced model, Eq. (3.1), we use the finite temperature version of the DQMC method (cf. Sec. 2.2). For the implementation we use the ALF code [42] as basis. We simulate the model sign-problem free using appropriate Hubbard-Stratonovich decoupling schemes [50, 110] (cf. App. A.1.2) for both the on-site and inter-site interactions within the regimes (i) $V \leq U/4$ for the U-V model, so that the renormalized $\bar{U} = U - z_D V \geq 0$, and (ii) $V_C \lesssim 0.62U$, such that $U\delta_{ij} + V_{ij}$ is a positive-definite matrix, for the LRC-Hubbard model. Note that an earlier study of the U-V model used a HS decoupling scheme in the DQMC framework that leads to a sign-problem for any finite $V > 0$ [104], which is not mentioned explicitly in that reference. As usual, we denote the (inverse) temperature by T ($\beta = 1/T$), while we set Boltzmann's constant to unity, $k_B = 1$.

In our work we analyze two quantities, namely the entropy S and the double occupancy

$$D = \frac{1}{N} \sum_{i} \langle n_{i\uparrow} n_{i\downarrow} \rangle \, . \tag{3.3}$$

We mainly focus on the double occupancy D, for which we perform a spatial averaging in order to enhance the statistical accuracy. For our temperature resolved results for D, we preformed a $\Delta\tau \to 0$ extrapolation, as detailed below in Sec. 3.5.1. The data for D shown in the results section 3.3 is always obtained from this extrapolation analysis.

The entropy S (per site) is obtained from the DQMC values of the internal energy E (per site) at $\Delta\tau = 0.1/t$ via thermodynamic integration,

$$S = \beta E(\beta) + \ln(4) - \int_0^\beta \mathrm{d}\beta' E(\beta') \,. \tag{3.4}$$

This formula stems from the thermodynamic relations for the free energy $F = E - TS$, $F = -T\ln(Z)$ and the internal energy $E = -\partial_\beta \ln(Z)$, whereas $\ln(4)$ is the value of the entropy in the $T \to \infty$ limit. We evaluate the integral numerically using the trapezoidal rule on a dense β-mesh. For the estimation of a statistical error of the integral we employ a simple bootstrap scheme: We repeatedly let the DQMC data points for E fluctuate within their respective error bars according to a Gaussian distribution and evaluate the integral in each iteration to obtain an averaged value with a statistical error. Additionally, we also measured the structure factors for antiferromagnetic (AF) ordering, stabilized, e.g. in the ground state of the Hubbard model at half-filling and for the commensurate charge density wave (CDW) state that is expected to be stabilized for sufficiently strong V in the U-V model [104]. The structure factors read

$$S_{\mathrm{AF}} = \frac{1}{N}\sum_{i,j=1}^{N} \epsilon_i \epsilon_j \langle \mathbf{S}_i \mathbf{S}_j \rangle \tag{3.5}$$

$$S_{\mathrm{CDW}} = \frac{1}{N}\sum_{i,j=1}^{N} \epsilon_i \epsilon_j \langle n_i n_j \rangle \,, \tag{3.6}$$

where $\epsilon_i = \pm 1$, depending on which sublattice of the bipartite square lattice the site i belongs to.

3.3 Results

In this section, we report the results from our DQMC simulations and compare them with previously reported findings. First, we present results for the Hubbard model, i.e. $V = V_C = 0$. Afterwards, we add more complexity to the system by considering nearest-neighbor non-local interactions and finally consider the long-range interacting case.

3.3.1 Hubbard Model

Highly accurate and detailed DQMC results of numerous thermodynamic quantities for the Hubbard model have been reported in Ref. [111]. However, these do not include the thermal behavior of both D and S, which we review below. For a direct comparison of our results with the numerical results reported from the variational approach in Ref. [109], we focus on the specific on-site repulsion to hopping ratio $U/t = 1.9$, which locates the electronic system within the Slater regime. In contrast to the Mott regime, where the insulating behavior emerges from a strong on-site Coulomb repulsion regardless of magnetic correlations, the Slater insulating regime is characterized by an antiferromagnetic ordering instability. We show in the left panel of Fig. 3.1 the DQMC results for D and in the right panel the results for S as a function of temperature simulated for various system sizes L. A distinctive feature of D in this regime is the appearance of a maximum at low temperatures. Furthermore, we include the extrapolation to the thermodynamic limit (TDL), performed as described below in Sec. 3.5.2.

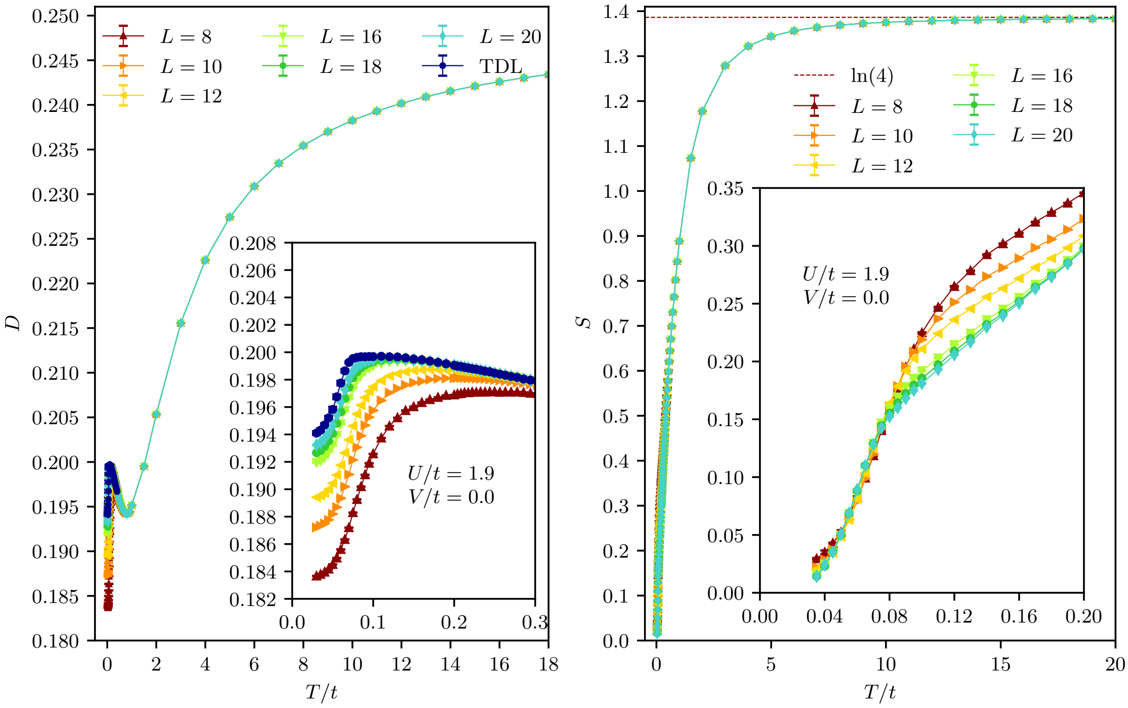

Figure 3.1: Temperature dependence of (left) the double occupancy D and (right) the entropy S for the Hubbard model at $U/t = 1.9$. The insets focus on the low-temperature regime containing the local maximum of D. Both figures are adapted from Ref. [1].

We quickly review the the non-monotonous behavior of D in the Slater regime exhibiting both a local minimum and a maximum. In cases where the long-range antiferromagnetic order in the ground state is quenched , one may also find a local minimum in the double occupancy, e.g., by geometric frustration [112] or within the non-magnetic dynamical-mean-field-theory approximation of the Hubbard model [113]. With increasing T the double occupancy D initially decreases due to an entropic effect analogous to the Pomeranchuk effect in Helium 3 or ultra-cold atoms [114]. The system gains entropy due to the formation of non-ordered local magnetic moments with respect to a state of itinerant electrons. However, further increasing the temperature, D eventually has to increase again due to thermal fluctuations to meet the non-interacting value 1/4 in the limit of infinite T. Combining the tendencies of both effects results in the local minimum of D visible in Fig. 3.1 at $T_{\text{min}} = 0.83t$. As for the local maximum in D at $T_{\text{max}} = 0.085t$ we can understand its formation from the proliferation of antiferromagnetic fluctuations for the Hubbard model on the bipartite square lattice via an energetic effect: In the Slater regime, the local Hubbard interaction energy $U \sum_i \langle n_{i\uparrow} n_{i\downarrow} \rangle = UD$ decreases upon lowering the temperature due to the onset of antiferromagnetic fluctuations [111]. We point out two mechanism responsible for the maximum in D at low temperatures: Moving away from the maximum towards lower temperatures, D is lowered to decrease the interaction energy (Slater effect). Competing to that, D is suppressed towards higher temperature to increase the spin entropy (Pomeranchuk effect). Note that the DQMC data for D in Fig. 3.1 shows an evidently faster drop for decreasing temperatures than for increasing T starting from the position of the maximum at T_{max}.

At this point we can draw a direct comparison of the DQMC data to the results reported from the variational approach [109]. We focus on the local maximum in the low-temperature region in particular. Both approaches agree well regarding the maximum's position T_{max}. However, both the finite-size DQMC data as well as the TDL extrapolated values fall below 0.2, whereas the local maximum extends clearly beyond 0.207 within the variational approach. One might consider this difference rather small, but such a fine scale is indeed relevant in view of the fact that the jumps in D reported in Ref. [109] for finite $V, V_C > 0$ are of even smaller magnitude. The detailed discussion follows below.

Before turning to finite extended interactions, we discuss the results for the entropy S for the same value of $U/t = 1.9$, cf. Fig 3.1. At intermediate temperatures below $T \approx t$, we observe an essentially linear decrease of S for large systems, down to a temperature of $T \approx 0.08t$. Continuing descending in temperature we observe a more rapid decrease of the entropy. Overall, this behavior is similar to the aforementioned asymmetric behavior in D near its local maximum at T_{max}. The enhanced reduction of both D and S below T_{max} reflects the Slater effect mentioned above upon entering the regime of proliferating antiferromagnetic fluctuations. Furthermore, the finite-size data for the entropy indicates a small temperature window below T_{max}, where S exhibits a (mild) increase with system size L, in contrast to its decrease with increasing L outside of this region. We suspect this anomalous behavior to originate from the growth of the antiferromagnetic correlation length on scales comparable to the system sizes for the chosen parameters. Instead, for lower (higher) temperatures the correlation length is well above (below) the dimension L of the finite lattice cell.

3.3.2 U-V Model

Next, we focus on the U-V model. In particular, we perform simulations for the parameters $V/t = 0.3$ and the same $U/t = 1.9$ as above. The reason for this precise parameter set is the observation of a noticeable jump in D within the variational approach at a temperature of $T \approx 0.085t$, which in Ref. [109] has been taken as an indication of a first-order metal-to-insulator transition. We perform the same data analysis for both thermodynamic quantities D and S as in the previous section and obtain the DQMC results presented in Fig. 3.2. In Fig. 3.3 we display the DQMC data for both D and S for the purpose of a direct comparison for the different models. Our data agrees with general expectations and the results from the variational approach regarding the increase of D for the case of finite $V > 0$, corresponding to an overall decrease of the local correlations. As for the entropy we observe a small increase in the low-temperature region for finite $V > 0$, while the general behavior of S remains similar to the $V = 0$ case. Besides the overall enhancement in D, especially in the temperature region around the local maximum, we do not observe a significant change in, e.g., the temperature of the maximum.

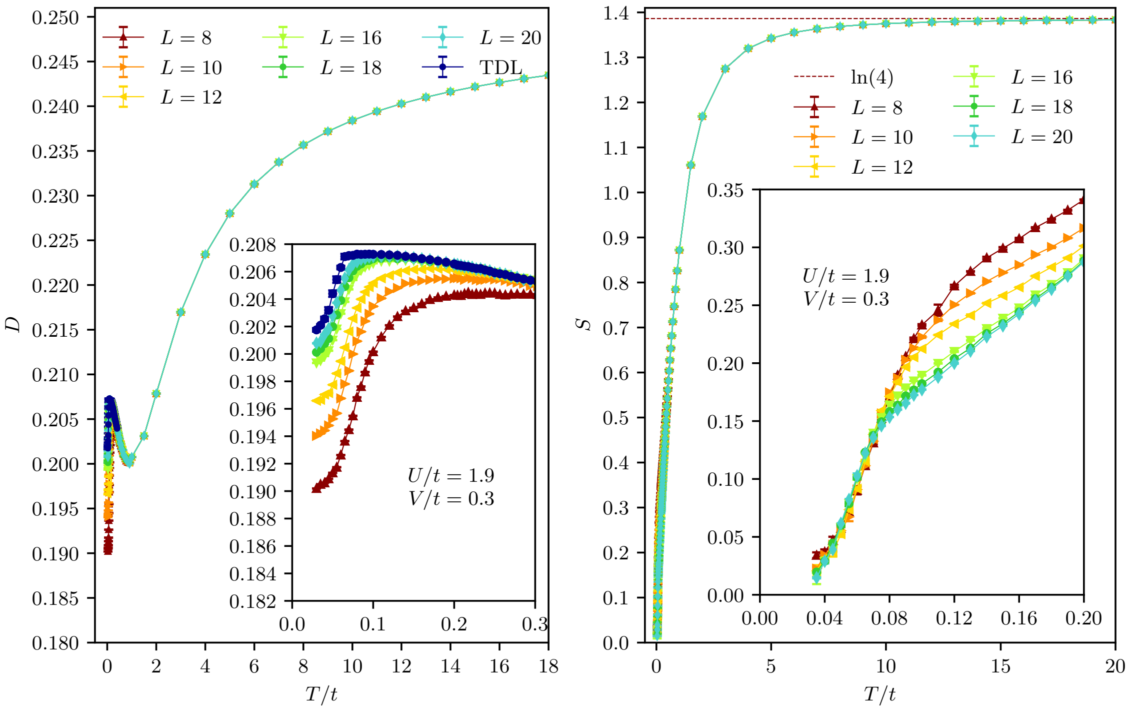

Figure 3.2: Temperature dependence of (left) the double occupancy D and (right) the entropy S for the U-V model at $U/t = 1.9$, $V/t = 0.3$. The insets focus on the low-temperature regime. Both figures are adapted from Ref. [1].

In the TDL extrapolation we observe a steeper drop of D on the low-temperature side of the maximum than for $V = 0$ case. However, compared to the variational approach, the finite-size DQMC data does not exhibit any indication for the onset of a discontinuity in D near the local maximum. Ref. [109] reports that the jump obtained by means of the variational approach is of order 3×10^{-4} for $V/t = 0.3$ and therefore rather small. As discussed in the previous section, we already noted that for the pure Hubbard case $V/t = 0$ the DQMC values for D deviate from the values obtained in Ref. [109] by a much larger difference, namely of order 7×10^{-3}. Furthermore, the finite-size systems studied with the variational approach extend up to $L = 12$, which is well below the value of up to $L = 20$ used in our DQMC simulations. Consequently, these observations suggest that the difference between the DQMC data and the data obtained with the variational approach stem from the interpolation and approximation schemes employed in Ref. [109]. While from our analysis we cannot definitely rule out that an extremely weak discontinuity may eventually arise (e.g., for values outside the sign-problem free regime $V/U > 1/4$), the above direct comparison of the magnitude of the deviations obtained from the variational approach with the DQMC data for the case $V/t = 0$ indicates that the small values of the reported discontinuity actually fall well within the error margins of the variational approach.

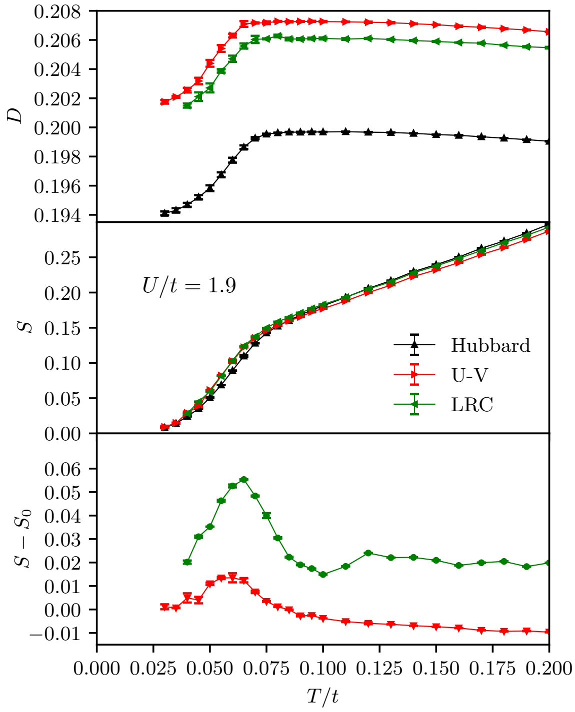

Figure 3.3: Temperature dependence of (left) the TDL-extrapolated double occupancy D and (right) the entropy S for the $L = 20$ systems for the considered models. The inset in the right panel shows the difference $S - S_0$ of the entropy for the models with extended interactions with respect to the entropy of the Hubbard model (here denoted as S_0). The figure is adapted from Ref. [1]

In addition to the specific value of $V/t = 0.3$, we performed DQMC simulations at other values of V up to including the limiting case of $V = U/4 = 0.475t$ for sign-problem free calculations with $U/t = 1.9$. The TDL-extrapolated values of the double occupancy D for the additional nearest-neighbor interaction strengths can be found in the left panel of Fig. 3.4, whereas the left panel of Fig. 3.5 shows the DQMC values for the entropy S on the largest considered system size $L = 20$ for the U-V model. For the various values of V, as for the case $V/t = 0.3$ in detail considered above, both quantities exhibit similar behavior and trends. A noticeable difference is the presence of a (weak) peak in D at the largest accessible values of $V/t \gtrsim 0.4$. We explain the corresponding enhancement in the local density fluctuations from considering the ordering tendencies of the U-V model. For sufficiently strong V, this model is expected to stabilize in a CDW ground state [104]. With the findings of a recent zero-temperature DQMC study [115], which demonstrates that for $V \leq U/4$ the system has an AFM ground state, we propose the stabilization of a CDW order for V sufficiently larger than $U/4$ only. We provide DQMC data for both

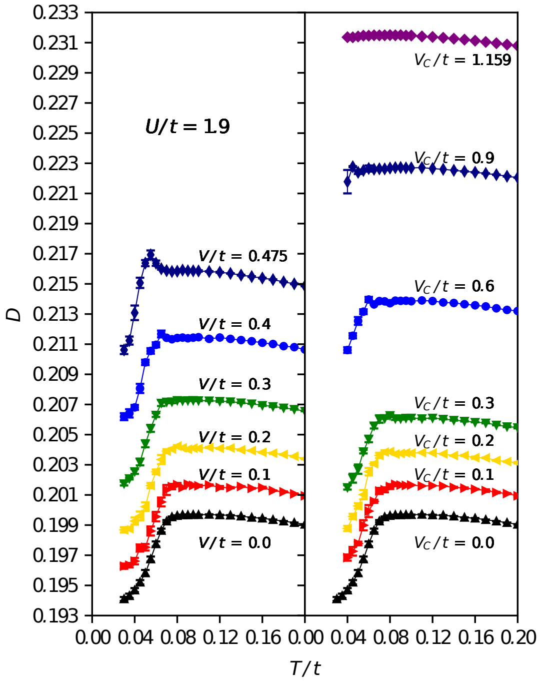

Figure 3.4: Temperature dependence of the TDL-extrapolated double occupancy D for (left) the U-V model and (right) the LRC-Hubbard model at $U/t = 1.9$ for various values of V and V_C. The figure is adapted from Ref. [1]

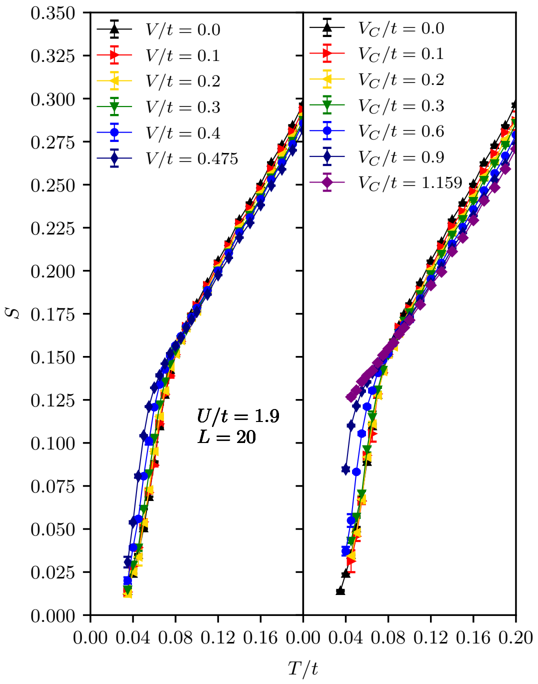

Figure 3.5: Temperature dependence of the entropy S for (left) the U-V model and (right) the LRC-Hubbard model at $U/t = 1.9$ for various values of V and V_C on the $L = 20$ system. The figure is adapted from Ref. [1]

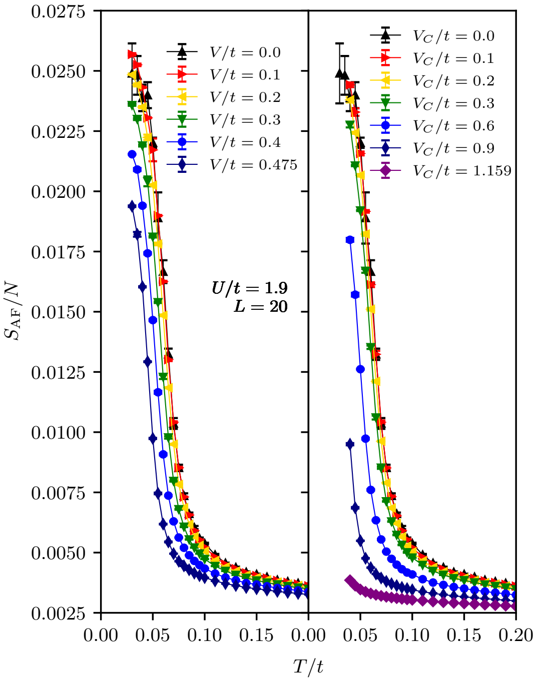

Figure 3.6: Temperature dependence of the AFM structure factor S_{AF} for (left) the U-V model and (right) the LRC-Hubbard model at $U/t = 1.9$ for various values of V and V_C on the $L = 20$ system. The figure is adapted from Ref. [1]

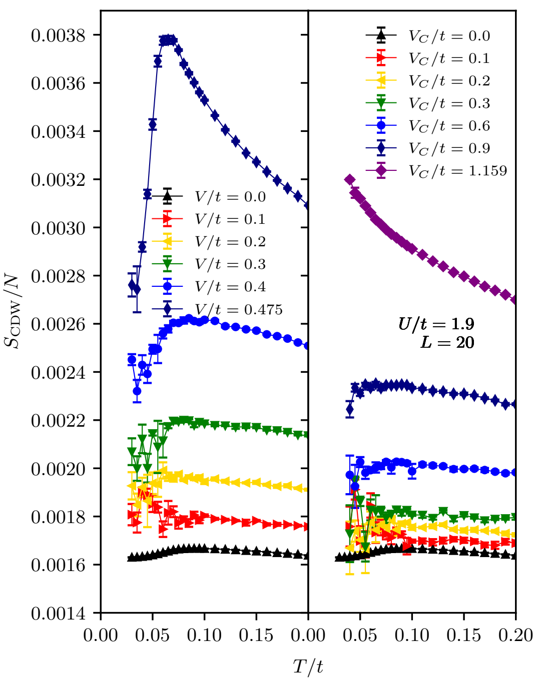

Figure 3.7: Temperature dependence of the CDW structure factor S_{CDW} for (left) the U-V model and (right) the LRC-Hubbard model at $U/t = 1.9$ for various values of V and V_C on the $L = 20$ system. The figure is adapted from Ref. [1]

structure factors S_{AF} and S_{CDW} for $L = 20$ and various values of V in the left panels of Fig. 3.6 and Fig. 3.7 for the U-V model. In agreement with the AFM ground state in the considered regime we find within the region accessible to DQMC a steady increase of the AFM structure factor with decreasing T. According to the Mermin-Wagner theorem [20], AFM order is destroyed by thermal fluctuations at any finite temperatures in the TDL. Upon lowering the temperature the CDW structure factor initially increases, before it is suppressed at sufficiently low T, which reflects the findings in Ref. [115] that for $V \leq U/4$ the ground state orders antiferromagnetically, while no CDW order persists. Increasing V, at some point the emerging CDW order stabilizes with respect to (weak) thermal fluctuations contrary to the AFM, i.e., the CDW order melts at a *finite* critical temperature across a thermal phase transition. From symmetry considerations, this transition belongs to the two-dimensional Ising universality class breaking a discrete $\mathbb{Z}_2$ symmetry. The critical local density fluctuations eventually enhance the double occupancy D in the vicinity of this thermal critical region for values of $V \lesssim U/4$, which apparently is captured by the data in Fig. 3.4. As a rough estimate for the critical temperature of the CDW melting transition in the interaction regime where the CDW ground state emerges, we identify from the peak position in D a temperature of $T/t \approx 0.06$.

3.3.3 LRC-Hubbard Model

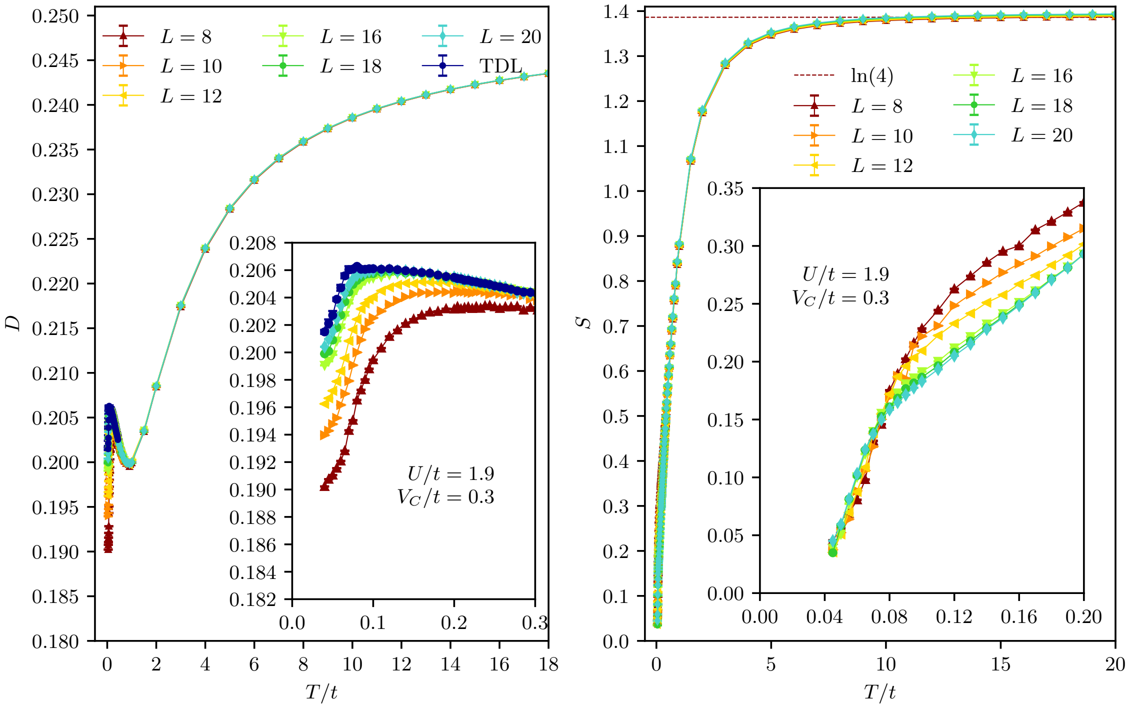

Figure 3.8: Temperature dependence of (left) the double occupancy D and (right) the entropy S for the LRC-Hubbard model at $U/t = 1.9$, $V_C/t = 0.3$. The insets focus on the low-temperature regime. Both figures are adapted fro Ref. [1]

For completeness, we also perform simulations for the case of long-range Coulomb interactions. In particular, we fix again the parameters $U/t = 1.9$ and set $V_C/t = 0.3$ accordingly to the nearest neighbor interaction V in the U-V model presented in the previous section. For this parameter set the variational approach yields a discontinuity in D comparable in magnitude to the U-V model case. In Fig. 3.8 we present our DQMC data for the LRC model. In this case, again we observe an overall enhancement of D and S with respect to the Hubbard model case, $V_C/t = 0$. The addition of interactions beyond the nearest-neighbor sites leads to a subtly weaker increase of D than for the U-V model, whereas the low-temperature enhancement of S is larger than for the latter model. Regarding the discontinuity reported in Ref. [109] for the LRC-Hubbard model, in this case, we also do not observe any indication for its presence in the DQMC data for D. Similar to the U-V model we performed DQMC simulations for varying values of V_C within the sign-problem free regime for $U/t = 1.9$. We present the DQMC data for the various considered quantities, D, S, S_{AF} and S_{CDW}, in the right panels of Figs. 3.4, 3.5, 3.6 and 3.7. For the considered values of $V_C/t > 0.6$ the computation did not allow us to reach sufficiently low temperatures down to the asymptotic low-T regime to see, e.g., the suppression of the entropy at low enough temperature (cf. Fig. 3.5). Within the relevant temperature range around $T/t \approx 0.06$, throughout the accessible interaction regime, the additional DQMC data exhibits very similar behavior and trends as for $V_C/t = 0.3$

3.4 Conclusion

In summary, we have examined two thermodynamic quantities of both the U-V model and the LRC-Hubbard model, which extend the on-site interaction of the Hubbard model. Focusing on the low-temperature regime, we studied the behavior of the double occupancy D and the entropy S, for which a recent variational approach proposed the emergence of a weakly first-order metal-to-insulator transition compared to the smooth crossover in the local Hubbard model limit [109].

Our DQMC data agrees with the variational calculations on the point of an overall enhancement of the double occupancy in the presence of finite extended interactions. We also identify an associated increase of the entropy within the low-temperature regime. Contrary to the behavior reported from the variational approach, both our finite-size data as well as the extrapolated TDL limit values do not provide any evidence for the presence or the onset of a discontinuity in D or S. Furthermore, we observe significant deviations of an order of magnitude that is larger than the size of the weak discontinuities reported in Ref. [109] from the variational calculations already for the Hubbard model case. We conclude that the non-continuous behavior found in Ref. [109] stems from inherent limitations of the variational approach in combination with the interpolations and filtering schemes employed in the previous study. Approaching the limiting values of $V = U/4$ for sign-problem free DQMC simulations for the U-V model, we observe a (weak) peak emerging in the temperature dependence of the double occupancy D. This could be linked to the enhancement of local density fluctuations in the vicinity of the thermal critical point of the CDW order that emerges for sufficiently large values of V, but which lies beyond the accessible interaction regime for DQMC.

We illustrate the discussed scenario for the U-V model in Sec. 3.3.2 with two sketches of qualitative phase diagrams in Fig. 3.9. In both scenarios, for sufficiently weak V/U the system resides in the ground state with an antiferromagnetically ordered spin density wave (SDW), breaking the continuous SU(2) symmetry, indicated by the green line. At the right end of the diagrams, i.e. large V/U, the system crosses the mentioned 2D Ising transition for decreasing temperature and stabilizes in a charge density wave (CDW),

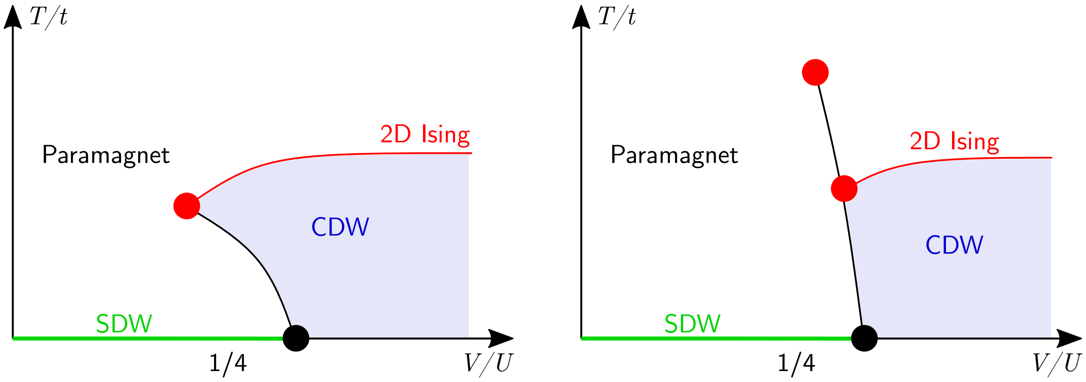

Figure 3.9: Two sketches of possible phase diagrams of the U-V model, where in both figures the green line indicates the SDW ground state, the black line a first order transition and the black dot a critical point, separating two symmetry broken phases. The shaded region depicts the stabilized CDW regime for large enough $V \gtrsim U/4$. The difference is how the first order transition line ends. Left: a 2D Ising transition (red line) meets the end of the black line in a tricritical point (red dot). Right: the black line ends at a critical point, whereas the red line terminates somewhere on the black line in a critical endpoint.

which is characterized by a broken discrete $\mathbb{Z}_2$ symmetry. In the vicinity of $V \approx U/4$ the 2D Ising critical line terminates at a tricritical endpoint in the left panel, indicated by the red dot and in a critical endpoint in the right panel. Notice the alternative ending of the black line in a critical point in the right panel. In this interaction region at low temperatures, the first order transition indicated by the black line is mediated by the competition between the local U and non-local V interaction and is depicted as a critical point at zero temperature by the black dot, separating both symmetry broken phases. Furthermore, the maximum in the S_{CDW} data in Fig. 3.7 for $V/t = 0.475$ can be viewed as a ”reentrance” scenario: at $V = U/4$ the system crosses the 2D Ising line upon decreasing temperature maximizing the value of S_{CDW}, entering the CDW region and leaving it again for small enough T thus lowering the value of the CDW structure factor. However, we cannot predict the curvature of both transition lines with certainty.

As an outlook it would certainly be enriching to extend the investigations on the thermodynamic properties of extended interactions in correlated electron systems with even larger values of the extended interactions strengths, beyond the limits of the DQMC simulations due to the sign-problem, based on, e.g., tensor network [34] or minimally entangled thermal typical state approaches [116, 117].

3.5 Extrapolations

3.5.1 Trotter Discretization Extrapolation

Discretizing the imaginary time and decomposing an exponential of the sum of operators, as introduced in Sec. 2.2 for the DQMC scheme, a Trotter-error arises that scales, due to the hermiticity of physical observables, asymptotically proportional to $\Delta\tau^2$ (cf. A.1.1). This property allows us to systematically extrapolate the DQMC data to the $\Delta\tau \to 0$ limit. The functional behavior of D in $\Delta\tau^2$ is illustrated for representative data sets for the Hubbard model at three different temperatures for the linear dimension $L = 20$ and $U/t = 1.9$ in Fig. 3.10. We provide access to all the obtained finite $\Delta\tau$ DQMC data via an online repository [118].

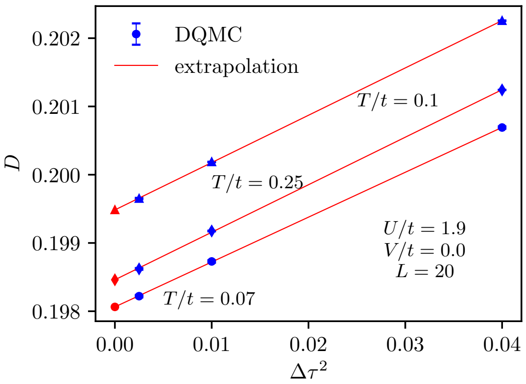

Figure 3.10: Trotter discretization extrapolation of the double occupancy D for the Hubbard model at $U/t = 1.9$ and linear dimension $L = 20$ for different values of the temperature T. The figure is adapted from Ref. [1]

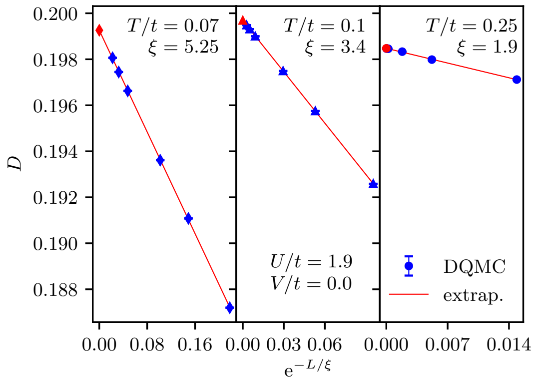

Figure 3.11: Finite-size extrapolation of the double occupancy D for the Hubbard model at $U/t = 1.9$ for several values of the temperature T. The figure is adapted from Ref. [1]

3.5.2 Finite-Size Extrapolation

The finite-size extrapolation to the TDL involves the consideration of the leading finite-size correction at low-temperatures in terms of a finite (correlation) length scale from thermal fluctuations. In particular, we obtain the TDL value for the double occupancy D_{TDL} by fitting the finite-size data D (after performing the $\Delta\tau \to 0$ extrapolation, cf. Sec. 3.5.1) to the finite-size form $D(L) - D_{\mathrm{TDL}} \propto \mathrm{e}^{-L/\xi}$, where ξ is a temperature T-dependent parameter that quantifies the corresponding length scale. We illustrate this procedure for a selection of representative data sets in Fig. 3.11.

Hubbard Model on ABCA Tetra-layer Honeycombs 4

Motivated by the recent experimental realization of an ABCA stacked tetra-layer graphene structure [119], we study ground state properties of the Hubbard model on a honeycomb tetra-layer lattice at half-filling, based on DQMC simulations. The free low energy band structure of multilayer rhombohedral graphene exhibits a flat band leading to a sharply peaked DOS at the Fermi level, which enhances correlation effects and allows for the emergence of magnetic order by introducing local Coulomb repulsion. We find a possible stabilization of antiferromagnetic order at $U/t \approx 5.3$. Furthermore, we find the AFM order to be robust with respect to enhanced inter-layer hopping strengths and an extended interactions.

The results in this chapter depict the QMC analysis of a collaborative work in preparation with authors of Ref. [119]. My contributions are the presented DQMC simulations. The SSE values in Fig. 4.5 have been provided by Nils Caci (RWTH Aachen).

4.1 Motivation

The discovery of correlated phases in stacked graphene multi-layers [120–125] and twisted multi-layer stacks [126–130] has led to great research effort from both the experimental side, as well as with various theoretical approaches. In particular, multi-layer systems with twisted graphene sheets, which lead to a moiré pattern with a unit cell that is about a hundred times larger than the distance between the carbon atoms, have aroused great interest regarding their correlated low-energy physics [131, 132]. This might suggest that strongly correlated physics emerges favorably in twisted graphene layer systems. However, it has been demonstrated that flat bands and strongly correlated many-body phases also arise in less complex multi-layer graphene arangements, e.g., in rhombohedral ABC-stacked graphene [133] or tetra-layered ABCA graphene [119]. Indeed, a perturbative approach [134] shows the effective low-energy band structure of rhombohedral multilayer graphene to exhibit a behavior $E(K) \sim k^N$ (where N is the number of layers) at the high symmetry points K, K' in the Brillouin zone. This implies the formation of essentially flat bands in these systems, which apparently can be achieved by stacking graphene layers. In the graphene realm, the experimental realization of stable multi-layered structures remains a challenging task. We explore magnetic ground state properties by taking screened Coulomb interactions into account, incorporated via a Hubbard model description of the carbon π-electrons. In particular, based on projective QMC simulations (cf. Sec. 2.2.3), we explore spin correlations over a wide local interaction strength range. Having identified the topmost 1-site and the bottommost 8-site (cf. Fig. 4.1) to hold the dominant spectral weight [119], we add a non-local interaction term between electrons on the respective sites for a more realistic model.

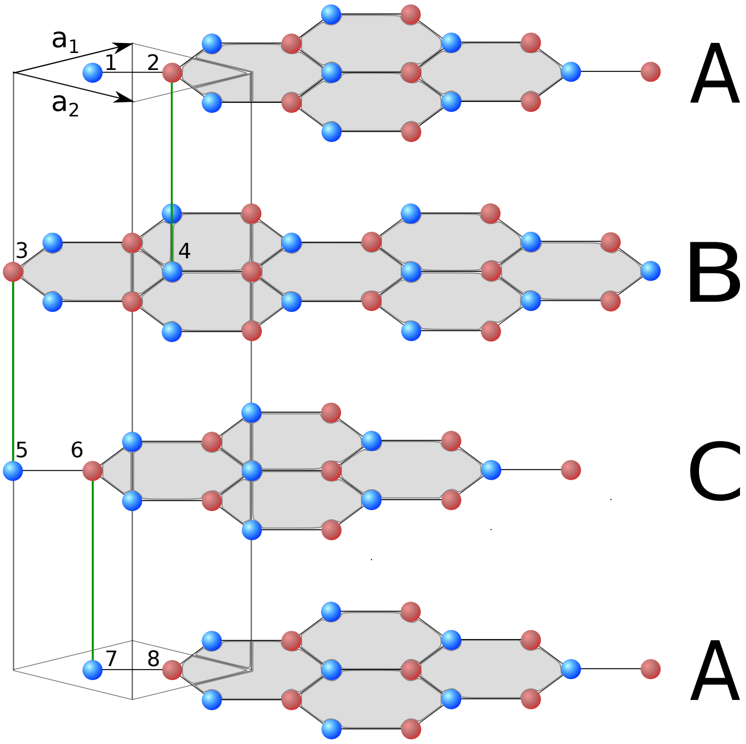

Figure 4.1: The ABCA stacked rhombohedral graphene lattice with its bipartite structure, indicated by two differently colored lattice sites. Included is the unit cell spanned by the lattice vectors $\mathbf{a}_1$, $\mathbf{a}_2$. Solid black lines indicate the intra-layer hopping t, while solid green lines indicate the inter-layer hopping $t_\perp$.

We consider the Hamiltonian $H = H_0 + H_U + H_{U'}$, with H_0 denoting the free tight-binding term containing both the intra-layer t and inter-layer $t_\perp$ hopping, $H_U = U \sum_i n_{i\uparrow} n_{i\downarrow}$ the local repulsion ($n_{i\sigma} = c^\dagger_{i\sigma} c_{i\sigma}$ the density operator at site i for spin σ) and $H_{U'} = U' \sum_{i,\sigma\sigma'} n_{i_1\sigma} n_{i_8\sigma'}$ the extended interaction between the 1-sites with the 8-sites, as illustrated in Fig. 4.1.

4.2 Spin Correlations

To probe for magnetic ground state properties based on QMC calculations, we measure the antiferromagnetic structure factor

$$S_{\mathrm{AF}} = \frac{1}{N} \sum_{i,j=1}^{N} \epsilon_i \epsilon_j \langle \mathbf{S}_i \mathbf{S}_j \rangle \, , \tag{4.1}$$

with alternating $\epsilon_i = \pm 1$ dependent on the sublattice in each layer and N the total number of sites. From this quantity we obtain the mean staggered magnetization per lattice site

$$m_s = \sqrt{S_{\mathrm{AF}}/(8L^2)} \, . \tag{4.2}$$

We fix the values $t = -0.375\,eV$ and $t_\perp = 0.46\,eV$, which were obtained from density functional theory (DFT) calculations in Ref. [119] and vary U and U'. Before turning on the extended U' interaction, we consider the pure Hubbard case on finite lattices of sizes $L = 6, 9, 12$. In Fig. 4.2 we report the DQMC data for the staggered magnetization over a large U range up to $U = 50\,eV$. From the finite-size data we cannot make a definitive statement about the low-U magnetization, in particular, how it scales with increasing U. We would require a finite-size extrapolation in the thermodynamic limit,

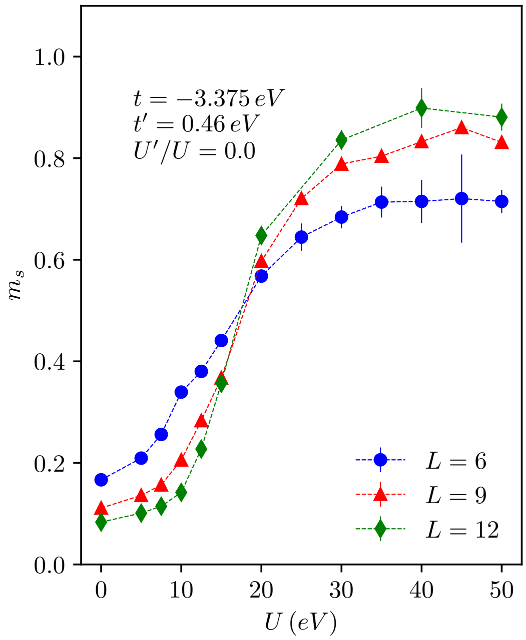

Figure 4.2: Local interaction U dependence of the staggered magnetization per lattice site m_s for the Hubbard model at $t = -0.375\,eV$ and $t_\perp = 0.46\,eV$ on lattice sizes $L = 6, 9, 12$.

which would be arguably unstable for only three finite sizes. Nevertheless, we find a (scale invariant) crossing point in the finite-size data at $U \approx 18\,eV$, with respect to the hopping at $U/t \approx 5.3$, which implies a phase transition from a paramagnetic to an AFM stabilized phase. Without further studies, we cannot rule out misleading finite-size behavior. Beneficial measurements could involve, e.g., the U-dependence of the single particle gap and the dynamic magnetic susceptibility, obtained from the imaginary-time resolved Green's function within DQMC, to gain more insight in the ground state properties.

Next, we investigate the effect of a varied inter-layer hopping $t_\perp$ reported in Fig. 4.3 representative on the $L = 9$ system. $t_\perp$ is the parameter that couples the layers, i.e., a vanishing $t_\perp$ results in decoupled graphene sheets. In this context we observe an enhancement of the staggered magnetization upon increasing $t_\perp$ at high values of U relative to t. In the high U limit we can describe the spin interactions via an effective coupling of $J = 4t^2/U$ and $J_\perp = 4t_\perp^2/U$, respectively (cf. Chap. 1). Within the effective description it is not surprising that spin correlations increase upon higher effective exchange coupling strengths. Finally, we turn on the extended U' interaction up to the value of $U'/U = 1$ for

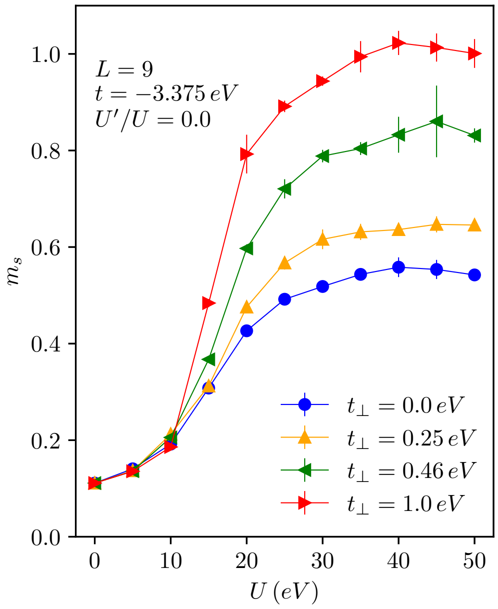

Figure 4.3: Local interaction U dependence of the staggered magnetization per lattice site m_s for the Hubbard model at $t = -0.375\,eV$ for various $t_\perp$ on the $L = 9$ lattice size.

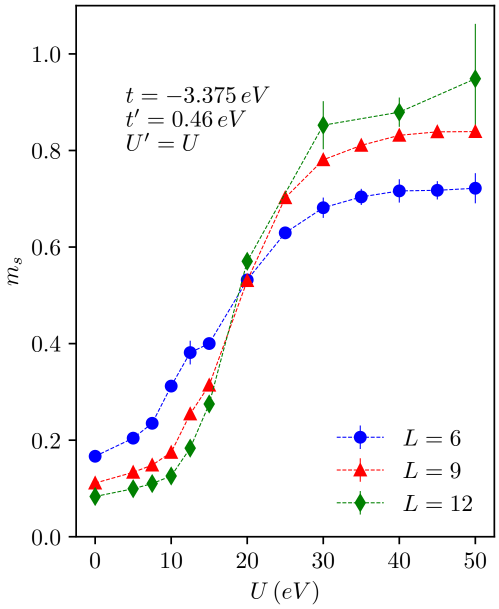

Figure 4.4: Local interaction U dependence of the staggered magnetization per lattice site m_s at $t = -0.375\,eV$ and $t_\perp = 0.46\,eV$ on lattice sizes $L = 6, 9, 12$ for the maximal value of $U' = U$ within the sign-problem free regime.

sign-problem free simulations in Fig. 4.4. The effect is marginal, but can still be observed in the vicinity of $U = 20\,eV$. The crossing point is slightly shifted to higher U values and the slope seems steeper. Having in mind the findings in Chap. 3, in particular, the proliferation of charge density order for extended interactions $V \gtrsim U/4$, one may expect a similar trend upon increasing U'/U, albeit on a smaller scale compared to the U-V model. For $U' \gtrsim U$ mean-field calculations predict the stabilization of an insulating charge transfer order [119] that meets an AFM phase at a first order transition line. The charge transfer order is characterized by a broken inversion symmetry between the top and bottom layer, which we can associate with a charge density wave, as in the U-V model case. The QMC data suggests that the AFM order might become less robust against quantum fluctuations upon increasing U', so that a higher U is required for the stabilization, while eventually it is destroyed completely for values $U' > U$ driving the system into a charge density ordered state. Again, this regime is inaccessible to sign-problem free DQMC.

4.3 Technical Remark

Although unbiased, QMC methods are still implemented on finite-precision machines, which on extreme scales can lead to numerical (round-off) errors. Here, we draw a comparison of the high-U values of m_s in Fig. 4.2 obtained by DQMC with the same quantity measured for the Heisenberg model, as an effective high-U limit, with proper J and $J_\perp$ couplings based on SSE simulations, shown in Fig. 4.5. We see a systematic difference in the DQMC and SSE values, however a qualitatively similar behavior. The DQMC overestimates in the high-U regime (starting at $U \gtrsim 30\ eV$ or $U/t \gtrsim 9$) the staggered magnetization, which we attribute to numerical precision errors for large values of U and is supposedly implementation dependent. A systematic Trotter error is unlikely, due to a relative small $\Delta\tau = 0.1$ used in the simulations. However, since the high-U limit is not of particular interest within this study, we did not dive into the numerical subtleties of the implementation.

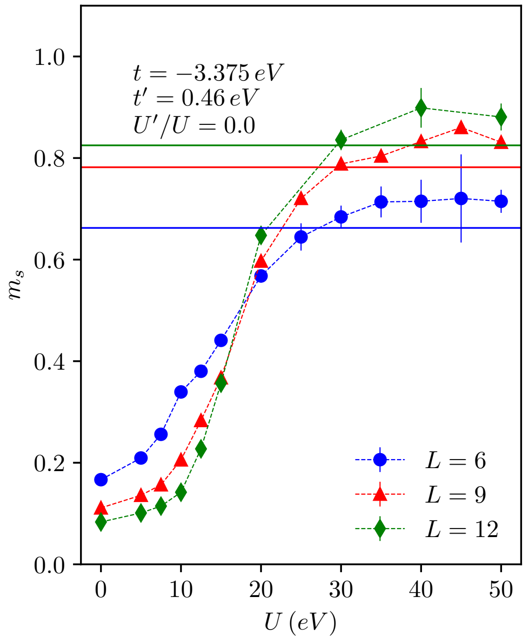

Figure 4.5: Local interaction U dependence of the staggered magnetization per lattice site m_s for the Hubbard model at $t = -0.375\,eV$ and $t_\perp = 0.46\,eV$ on lattice sizes $L = 6, 9, 12$. The solid horizontal lines are effective values in the high-U limit obtained from SSE calculations of the Heisenberg model with $J = 4t^2/U$ and $J = 4t_\perp^2/U$.

4.4 Conclusion

Based on the projective version of DQMC for ground state calculations, we examined the magnetic properties of the Hubbard model on an ABCA stacked tetra-layer graphene structure with realistic hopping strengths obtained by DFT calculations. In detail, we explored the U-dependence of the mean staggered magnetization on the finite lattice sizes $L = 6, 9, 12$ and found an indication of a transition into an AFM ordered phase at a ratio of $U/t \approx 5.3$. Due to the immense computational cost, we cannot access larger lattices, so that a stable extrapolation in the TDL is not feasible. We did observe an enhanced m_s upon increasing $t_\perp$ for high values of U/t. In this regime we describe the spin interaction effectively by the exchange couplings $J = 4t^2/U$ and $J_\perp = 4t_\perp^2/U$, which gives a natural explanation for stronger spin correlations upon increasing the inter-layer spin coupling. For a realistic description of the system, we added an extended U' interaction between the topmost 1-sites and the bottommost 8-sites and explore its influence on the magnetic properties. A finite U' apparently shifts the transition point to higher values of U, thus destabilizing the AFM order. One may expect a similar behavior as for the U-V model in Chap. 3, where we observed the proliferation of a charge density order for large enough extended interactions with respect to the local U. Indeed, the stabilization of a charge transfer order, which we associate with a charge density wave, has been predicted by mean-field calculations [119]. Unfortunately, higher U'/U ratios are not accessible to sign-problem free DQMC simulations. To study the ground state further, it would be beneficial to calculate the single-particle gap and the dynamic magnetic susceptibility, which can be obtained from the imaginary-time resolved Green's function.

Anisotropic Quantum Heisenberg Model

5

Using the SSE scheme for large-scale QMC simulations, we determine the ground state phase diagram of the spin-1/2 antiferromagnetic Heisenberg model on the honeycomb lattice. We consider the most generic case of interaction strengths, namely, varying exchange couplings along the three unequivalent lattice directions. We determine continuous quantum phase transition lines separating a long-range ordered antiferromagnetic state from three quantum-disordered regimes. These regimes exhibit dimer-singlet formations along the dominant exchange coupling. We find anomalously large scaling corrections to the finite-size behavior along the transition lines. These corrections can be related to recent, similar findings in certain dimerized quantum spin systems and to singular one-dimensional limits in the model parameter space. Furthermore, we include more general comments on the non-universality of critical cumulant ratios in anisotropic systems, as well as on attempts to restore universality of these ratios by tuning the lattice aspect ratio.

The results in this chapter have been published in Ref. [2]. My contributions have been performing the SSE simulations, carrying out the extrapolations and partially writing the manuscript. The data presented in Figs. 5.12, 5.13 has been obtained by Stefan Wessel.

5.1 Motivation

Among the eleven uniform Archimedean tilings, i.e., periodic tessellations of the plane by regular polygons such that all edge lengths are equal and every vertex looks alike, the honeycomb lattice has the lowest possible coordination number of three [135]. However, due to its bipartitness, realized through a Bravais lattice with a two-atom basis, a Néel antiferromagnetic ground state ordering may stabilize. One of the most prominent examples is the spin-1/2 Heisenberg antiferromagnet with isotropic nearest-neighbor interactions, which considers the same interaction strength among all two-site bonds on the honeycomb lattice [136, 137]. Introducing one anisotropic coupling, i.e., a deviating interaction strength along one of the three unequivalent bond directions with respect to the other two, the quantum spin system can be driven out of the AFM regime. Explicitly for the honeycomb lattice a critical ratio of the corresponding couplings has been found. If the ratio extends beyond a critical value of 1.735, the AFM order is destroyed and the system resides in a non-magnetic, quantum disordered ground state, namely a dimerized state characterized by the dominant formation of spin singlets among the bonds with the larger interaction strength [138].

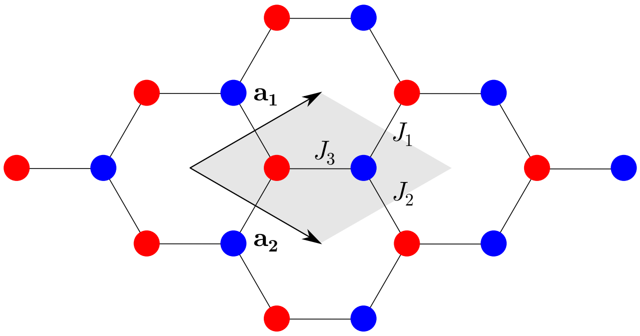

Figure 5.1: The honeycomb lattice with its bipartite structure, indicated by two differently colored lattice sites. The gray shaded area indicates the unit cell spanned by the lattice vectors $\mathbf{a}_1$ and $\mathbf{a}_2$. The exchange couplings are denoted by J_1, J_2 and J_3 along the three unequivalent bond directions. The shown finite lattice corresponds to a linear dimension $L = 3$. The figure is adapted from Ref. [2].

This way of dimerization on the honeycomb lattice exhibits a certain similarity to a dimerized quantum magnet on the square lattice. Different dimerization patterns, e.g., columnar vs. staggered, have been rigorously studied recently [138–145]. At the quantum phase transition, various studies on two-dimensional quantum Heisenberg magnets with columnar dimerization patterns have found critical exponents consistent with the classical three-dimensional O(3) universality [139, 140, 146–148]. Notably, for the specific case of staggered dimerization patterns, large scaling corrections at the quantum phase transition between the AFM phase and the disordered quantum state have been reported [141–145]. These scaling corrections have been associated to certain non-topological cubic terms in the effective low-energy field theory describing the quantum critical point [143].

The effective field theory includes the relevant degrees of freedom at low energy scales to describe, e.g., the mentioned quantum phase transition, disregarding degrees of freedom at higher energy scales. Without diving into details, let us illustrate the relevant points, while we refer to Ref. [149] for a comprehensive introduction into quantum field theories. Within this framework, the quantum partition function is defined in the path integral formalism in the following way:

$$Z = \mathrm{Tr}\left(\mathrm{e}^{-\beta H}\right) = \int [\mathrm{d}\phi(\tau, \mathbf{x})]\, \mathrm{e}^{-S(\phi)}\,, \tag{5.1}$$

where $\phi(\tau, \mathbf{x})$ is an imaginary-time and real-space dependent continuous field and $S(\phi)$ is an action (note the formal similarity to the DQMC partition function in Sec. 2.2). On a finite lattice, given an imaginary time τ', we can write the path integral as product of ordinary integrals of a degree of freedom $\phi(\mathbf{x}_i)$ at each lattice site:

$$\int [\mathrm{d}\phi(\tau', \mathbf{x})] \sim \prod_{\mathbf{x}_i} \int_{-\infty}^{\infty} \mathrm{d}\phi(\tau', \mathbf{x}_i) \,. \tag{5.2}$$

Identifying the integrand in Eq. (5.1) as a positive measure, the partition function may act as a moment-generating function, i.e., we are able to compute equal-time n-point correlation functions:

$$\langle \phi(\mathbf{x}_1) \dots \phi(\mathbf{x}_n) \rangle \sim \int [\mathrm{d}\phi] \; \phi(\mathbf{x}_1) \dots \phi(\mathbf{x}_n) \mathrm{e}^{-S(\phi)} \,. \tag{5.3}$$

In our case, we may associate the vector field ϕ with a three-component vector order-parameter field describing magnetic fluctuations. Typically, SU(2) symmetric models, describing quantum magnets, are formulated with an action of the ϕ^4 type, i.e., the action only contains terms with even powers of ϕ up to forth order. The critical behavior of this particular form is known to follow the O(3) universality [143]. However, as mentioned above, certain staggered-dimer spin-1/2 Heisenberg models displayed deviations from the expected O(3) critical behavior, which could be associated with a cubic term in the effective action, derivated in Ref. [143]. In addition to those corrections expected for the three-dimensional classical Heisenberg universality class, which generically characterize the quantum phase transition in such bipartite dimerized spin systems [150], they give rise to a further (in the RG sense) weakly-irrelevant operator [145]. An introductory overview to the RG is provided in Ref. [151].

In this chapter, we report the appearance of similar anomalously large scaling corrections on the phase transition line in the anisotropic Heisenberg model on the honeycomb lattice, upon considering the most generic case, in which all three unequivalent nearest-neighbor bonds have a different coupling strength. Furthermore, we can link this scaling correction of the two-dimensional lattice to the special scaling in the one-dimensional limit, which is realized for a vanishing coupling along one of the three unequivalent bond directions. For the analysis of the anisotropic Heisenberg model we used large-scale quantum Monte Carlo simulations, based on the SSE [23–25], which we introduced in Sec. 2.3. Based on the QMC analysis, especially focusing on the Binder ratio [145, 152], we determine the quantum phase transition lines and obtain the global ground state phase diagram of the most generic form of the anisotropic nearest-neighbor spin-1/2 Heisenberg model on the honeycomb lattice.

5.2 Anisotropic Hamiltonian

We consider the spin-1/2 Heisenberg model with different interaction strengths J_1, J_2 and J_3 between the nearest-neighbor bonds along the three unequivalent directions on the honeycomb lattice, described by the Hamiltonian

$$H = J_1 \sum_{\langle i,j \rangle_1} \mathbf{S}_i \cdot \mathbf{S}_j + J_2 \sum_{\langle i,j \rangle_2} \mathbf{S}_i \cdot \mathbf{S}_j + J_3 \sum_{\langle i,j \rangle_3} \mathbf{S}_i \cdot \mathbf{S}_j \, , \tag{5.4}$$

where each of the three summations extends only over the parallel bonds corresponding to the labeling in Fig. 5.1. Each $\mathbf{S}_i$ denotes a vector operator containing the three spin operators $S_i^\alpha = \frac{\hbar}{2}\sigma_i^\alpha$ with σ_i^α being the Pauli-matrices for $\alpha = x, y, z$. As usual we set $\hbar = 1$ in the following.

Previous studies in the isotropic case, i.e., $J_1 = J_2 = J_3$, have shown that the ground state stabilizes long-range AFM order. In this case, the staggered magnetization m_s^{iso} is reduced by about 54% from its classical value in the perfect Néel state [137]. As a next step it has been considered to enhance one of the three exchange couplings, e.g. $J_1 > J_2 = J_3$. This study has found that the AFM order gets suppressed and for $J_1/J_2 = J_1/J_3 > 1.735(1)$ the ground state is driven into the aforementioned dimerized quantum disordered state with a dominant singlet formation along the J_1 bonds [138], which we denote by D_1, corresponding to the lattice direction in the following. Analogously, upon increasing J_2 (J_3) with respect to $J_1 = J_3$ ($J_1 = J_2$), the dimerized states, denoted by D_2 (D_3), form dominant singlets along the J_2 (J_3) bonds. Here, we explore the phase diagram for the most general case of fully spatially anisotropic interactions, i.e. all three exchange couplings may be varied independently.

To this end we have performed QMC computations employing the SSE scheme with directed loop updates. We have simulated several finite-size systems of rhombic shape (integer multiples of the shaded area in Fig. 5.1) built by stringing together copies of L unit cells in both the $\mathbf{a}_1$ and $\mathbf{a}_2$ directions resulting in the number of spins $N = 2L^2$. The simulations have been performed at sufficiently low temperatures to probe ground state properties and with periodic boundary conditions. Based on the staggered magnetization

$$m_s = \sqrt{S_{\mathrm{AF}}/N} \, , \tag{5.5}$$

where S_{AF} is the staggered structure factor

$$S_{\mathrm{AF}} = \frac{1}{N} \sum_{i,j} \epsilon_i \epsilon_j \langle \mathbf{S}_i \cdot \mathbf{S}_j \rangle \, , \tag{5.6}$$

with $\epsilon_i = \pm 1$, depending on the sublattice on which $\mathbf{S}_i$ is located, we determine the system's state (ordered AFM or disordered dimerization) after an extrapolation to the thermodynamic limit. Moreover, we extract the phase transition lines by measuring the Binder ratio [138, 145, 152]

$$R = \frac{\langle M_s^4 \rangle}{\langle M_s^2 \rangle^2}\,, \tag{5.7}$$

where $\langle M_s^x \rangle = \langle (\sum_i \epsilon_i S_i^z)^x \rangle$ denotes the staggered moment of the order parameter distribution. The Binder ratio characterizes how close the order parameter distribution is to a Gaussian. In the disordered phase, e.g., in the D_1 state for $J_1/J_2 = J_1/J_3 > 1.735(1)$ as mentioned above, the linear dimension L is much larger than the correlation length ξ. Since regions separated on a larger scale than ξ are uncorrelated, it follows from the central limit theorem that the probability distribution of the order parameter is a Gaussian around $M_s = 0$. With Wick's theorem we find $\langle M_s^4 \rangle = 3\langle M_s^2 \rangle^2$ so that $R \to 3$. Contrary, deep in an ordered phase, e.g. in the AFM, fluctuations in the order parameter are suppressed and $\langle M_s^4 \rangle = \langle M_s^2 \rangle \langle M_s^2 \rangle$ and $R \to 1$ for a one-component order parameter. n-component order parameters, such as $n = 3$ for the Heisenberg model, introduce n-dependent factors [16]. The relation between the one-component order parameter to the three-component order parameter, containing the magnetization with respect to all three directions, can be found in App. A.3. However, at the critical point, which lies somewhere in between these two limiting cases, the central limit theorem does not generally hold, due to long-range spin correlations and a diverging correlation length. Numerical data does not exactly diverge for finite-size systems, but a peak emerges for increasing system sizes, mimicking a divergence for singular quantities in the thermodynamic limit. The critical point can be determined by the specific fixed-point value R_c (in a renormalization-group sense), which is characteristic for the universality class [152]. The magnetization is known to scale with $\langle M_s \rangle \sim L^{-\beta/\nu}$ [153], so that at criticality, the power laws $\langle M_s^2 \rangle \sim L^{-2\beta/\nu}$ and $\langle M_s^4 \rangle \sim L^{-4\beta/\nu}$ cancel and R becomes (almost) scale independent at R_c. To leading order the different finite-size systems with a fixed spatial (as well as for quantum phase transitions fixed space-time) aspect ratio, cross each other at the (quantum) critical point, up to a small drift. For this subtle drift we observe the aforementioned anomalous scaling behavior in the presence of anisotropic coupling ratios.

Before we go into details on the scaling corrections, we present the ground state phase diagram in the following section.

5.3 Ground State Phase Diagram

First we consider the ground state phase diagram shown in Fig. 5.2, which illustrates the different ground state regimes. The parametrization is given in units of the coupling J_3, so that we tune the ratios J_1/J_3 and J_2/J_3 and obtain finite-size analyzed values from the QMC data. Employing barycentric coordinates, defined as $j_i = J_i/(J_1 + J_2 + J_3)$ with

$j_1+j_2+j_3=1$, we express the phase diagram in an alternative form incorporating its three-fold rotational symmetry, shown in Fig. 5.3 (a point's coordinates in the diagram lie on the intersection of lines parallel to the respective left axis in counter-clockwise direction). Included in this figure is a heatmap of the staggered magnetization m_s normalized to its maximum value m_s^{iso} in the isotropic case located at the center of the triangle. Evaluating

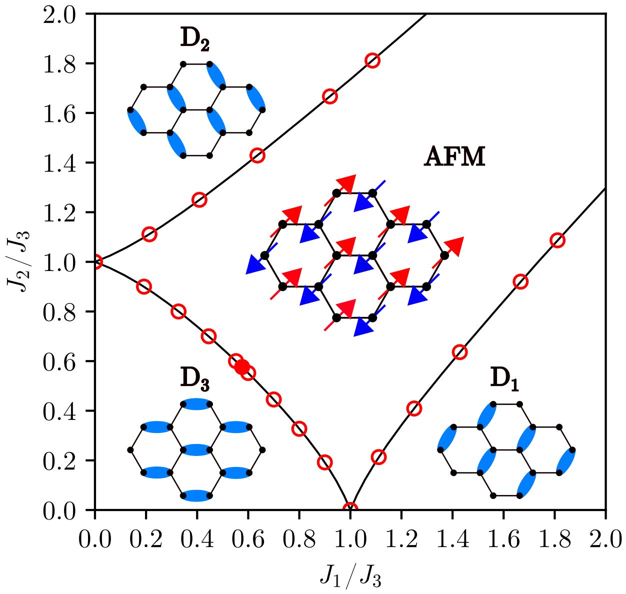

Figure 5.2: Ground state phase diagram of the anisotropic spin-1/2 Heisenberg model on the honeycomb lattice, expressed in the two parameter ratios J_1/J_3 and J_2/J_3. Circles indicate results from the QMC simulations, while the solid lines are a guide to the eye. Illustrated within each disordered regime, is the dominant dimerization pattern. The figure is adapted from Ref. [2].

the ground state phase diagrams, we find that the three dimerized disordered states D_1, D_2, and D_3 are separated by the AFM phase. They meet only pairwise at singular points, which are found on lines where one coupling vanishes. For example, if we fix $J_1=0$, the system decouples into zig-zag chains (cf. Fig 5.1) along the $\mathbf{a}_2$ direction and for $J_2=J_3$ these chains have a gapless, quantum critical ground state, so that an arbitrarily weak inter-chain coupling $J_1>0$ drives the system into the AFM phase [154]. Away from these quantum critical points, in our example for $J_2>J_3$ ($J_3>J_2$), the isolated chains have a gapped ground state, namely dimerized bonds along the J_2 (J_3) direction, corresponding to the one-dimensional limit of the D_2 (D_3) phase [154]. Thus, to drive the system into the AFM phase, a finite inter-chain coupling $J_1>J_1^c>0$ is required to overcome the excitation gap. These quasi-one-dimensional physics and the corresponding cases for $J_2=0$ and $J_3=0$, give rise to the curved triangular shape of the AFM phase in Fig. 5.3.

The phase boundaries have been obtained by a finite-size analysis of the Binder ratio,

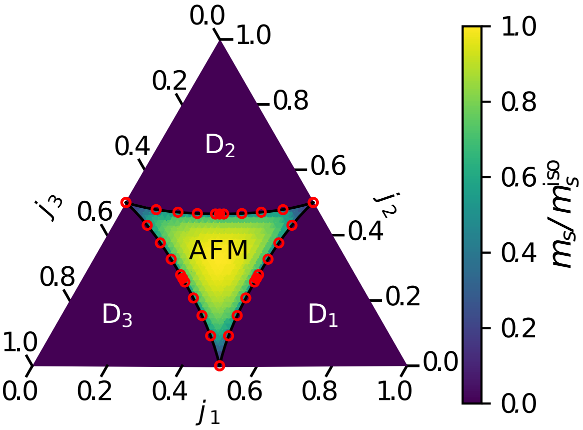

Figure 5.3: Ground state phase diagram of the anisotropic spin-1/2 Heisenberg model on the honeycomb lattice, expressed in barycentric coordinates. Circles indicate results from the QMC simulations, while the solid lines are a guide to the eye. Also shown inside the AFM regime is the magnitude of the staggered magnetization m_s, normalized to its maximum value m_s^{iso} in the isotropic case (located at the center of the triangle). The figure is adapted from Ref. [2].

which we discuss in detail in the following section. In particular, we find anomalous scaling corrections in the finite-size data for the Binder ratio, which we link to the singular, quantum critical points mentioned above.

5.4 Finite-Size Analysis

In order to determine the phase transition lines within the antiferromagnetic order stabilizes, we fixed the value of J_2/J_3 and varied J_1/J_3 in the QMC simulations. Along horizontal cuts in Fig. 5.2 we restricted the computations to the regime $J_1 \leq J_2 \leq J_3$, due to the system's symmetry. We obtain the other sections of the boundary by appropriate relabeling of the couplings.

First, we consider the symmetric line along $J_1 = J_2$, i.e., along the diagonal through the red, solid circle in Fig. 5.2. Fig. 5.4 shows the Binder ratio R dependent on the coupling ratio J_1/J_3 for $L \times L$ lattice sizes and fixed inverse temperature $\beta = 2L$ in units of $1/J_3$ [145]. A line crossing in the finite-size QMC data for R can indeed be observed in Fig. 5.4 near $J_1/J_3 \approx 0.576$. However, on a finer scale, the data exhibits a systematic drift of the crossing points between the different system sizes. In Fig. 5.5 and Fig. 5.6, we examine the crossing point values of $g = J_1/J_3$ and R between system sizes L and $2L$.

A striking feature of both g and R resolved in $1/L$ is a strongly nonmonotonic behavior. In Ref. [145] similar finite-size dependent curves have been observed for the staggered dimer square lattice model, but not for the columnar dimer case. This similarity makes

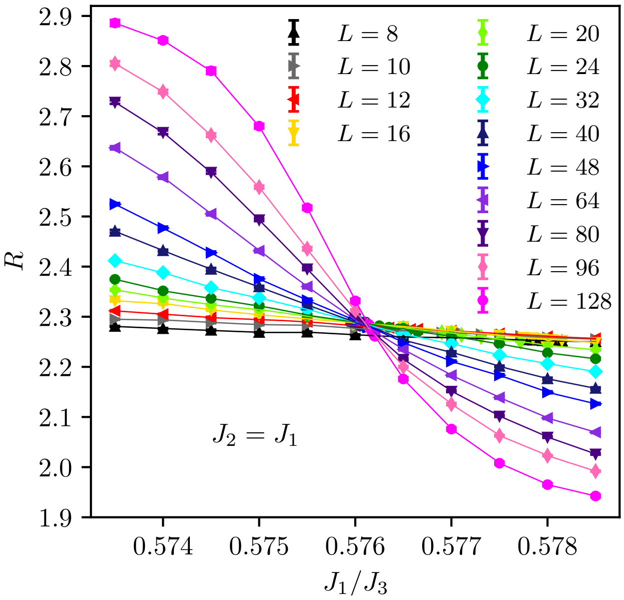

Figure 5.4: Binder ratio R as a function of $J_1 = J_2$ for different system sizes L. The figure is adapted from Ref. [2].

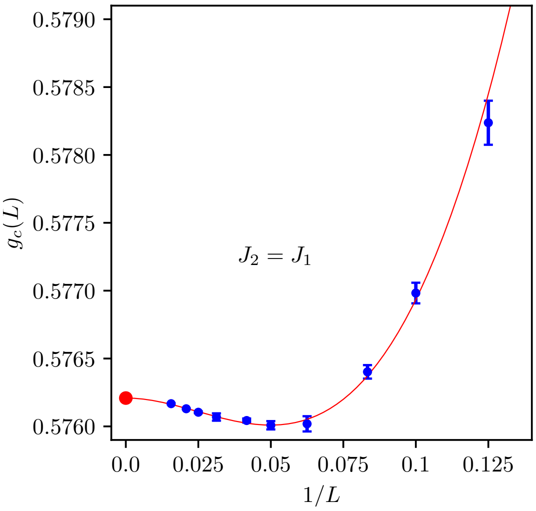

Figure 5.5: Crossing point values of $g = J_1/J_3$ for the Binder ratio R for $J_2 = J_1$ between system sizes L and $2L$. The red line indicates a fit to the finite-size scaling form Eq. (5.8) with the TDL value marked with a red dot. The figure is adapted from Ref. [2].

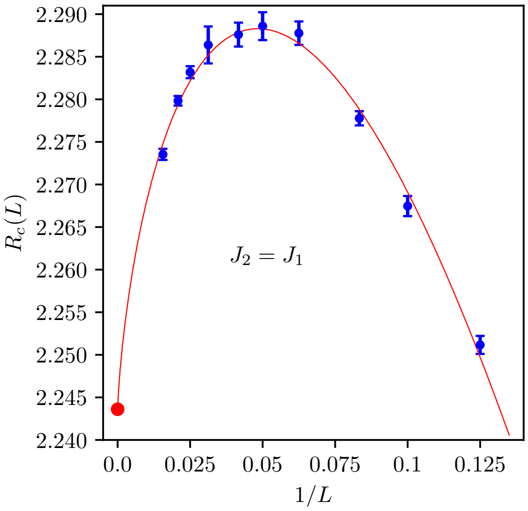

Figure 5.6: Crossing point values of the Binder ratio R for $J_2 = J_1$ between system sizes L and $2L$. The red line indicates a fit to the finite-size scaling form Eq. (6.4) with the TDL value marked with a red dot. The figure is adapted from Ref. [2].

sense upon comparing the two lattice structures: on the honeycomb lattice, the stronger coupled bonds, in this case the J_3 bonds, are arranged in a staggered fashion, however, with an effectively weaker inter-dimer coupling than on the staggered dimer square lattice. Notable in Ref. [138] is that (for the same coupling regime as here) no such nonmonotonic behavior has been reported, which can be possibly explained by (i) a lower coupling ratio resolution near the quantum critical point for the large system sizes than here, and/or (ii) the different finite-size lattice geometry employed in that study (different choice of a unit cell for the computations).

A careful finite-size analysis of such nonmonotonic scaling corrections has been performed in Ref. [145]. The conclusion of this work is that these scaling corrections are best accounted for by considering two subleading correction terms to the leading scaling form,

$$g_c(L) = g_c + L^{-1/\nu}(a_1 L^{-\omega_1} + a_2 L^{-\omega_2})\,, \tag{5.8}$$

$$R_c(L) = R_c + b_1 L^{-\omega_1} + b_2 L^{-\omega_2}\,, \tag{5.9}$$

where g denotes the tuning parameter driving the quantum phase transition, in our case $g = J_1/J_3$, ν is the scaling exponent of the correlation length and ω_1, ω_2 are two correction exponents, whereas the a_i, b_i are nonuniversal prefactors. The exponents $1/\nu = 1.406$ and $\omega_1 = 0.78$, which have been taken in Ref. [145] from the classical values of the three-dimensional Heisenberg universality class [155–157], can also be considered for the quantum phase transition in the present case. Note that besides ν, also the correction exponent ω_1 is universal within a given universality class. For the staggered dimer square-lattice model a value of $\omega_2 \approx 1.25$ has been estimated in Ref. [145] and it was argued that the additional correction term stems from the cubic term in the effective action of the field theory describing the quantum critical point [143, 145].

The anomalous, nonmonotonic behavior observed for the honeycomb lattice here fits well (cf. Figs. 5.5, 5.6) to the above mentioned ansatz in Eq. (5.8) and Eq. (6.4), which we affirm with values of $\chi^2/\text{d.o.f.} \approx 1$. Unfortunately, we are not able to perform an independent, robust estimation of the scaling exponents, due to the limited accessible accuracy on the crossing points. As a result of these fits, we obtain estimates for the critical coupling $J_1^c = 0.57620(1)J_3$ (illustrated by the full, red circle in Fig. 5.2 and Fig. 5.3) at a critical Binder ratio $R_c = 2.244(1)$. The stated uncertainties stem from the fitting procedure and do not account for the unknown uncertainty in the value of ω_2 estimated in Ref. [145]. We find our values agree with the previous estimates along the diagonal line in the coupling ratio space [142].

Upon deviating from the symmetric line $J_2 = J_1$, we find the anomalous finite-size behavior to persist. Representative for an intermediate coupling regime, we discuss the case $J_2 = 0.7J_3$. Here, based on the fits shown in Fig. 5.7 and 5.8, we estimate the critical values $J_1^c = 0.44533(1)J_3$ and $R_c = 2.258(1)$, respectively.

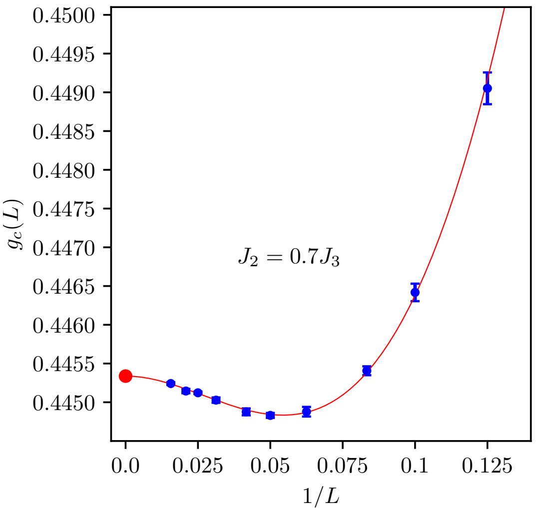

Figure 5.7: Crossing point values of $g = J_1/J_3$ for the Binder ratio R for $J_2 = 0.7J_3$ between system sizes L and $2L$. The red line indicates a fit to the finite-size scaling form Eq. (5.8) with the TDL value marked with a red dot. The figure is adapted from Ref. [2].

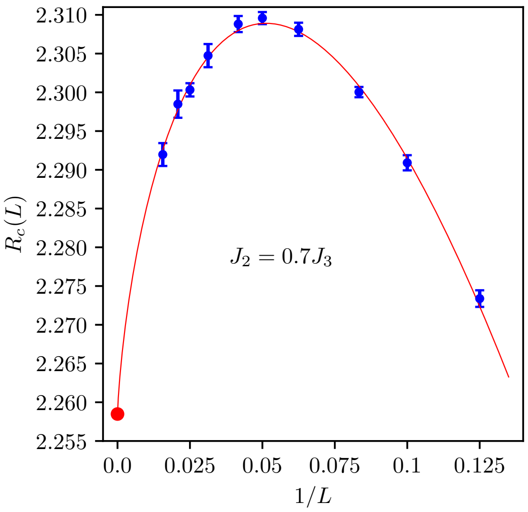

Figure 5.8: Crossing point values of the Binder ratio R for $J_2 = 0.7J_3$ between system sizes L and $2L$. The red line indicates a fit to the finite-size scaling form Eq. (6.4) with the TDL value marked with a red dot. The figure is adapted from Ref. [2].

However, upon increasing J_2/J_3, we arrive at a distinct and noteworthy coupling ratio $J_2 = J_3$, shown in Fig. 5.9 and 5.10. Here, we observe a rather peculiar finite-size scaling behavior regarding the scaling forms above. The data does not feature the previously observed nonmonotonic behavior, instead it fits well to scaling forms with only a single exponent each, which we denote by p and ω,

$$g_c(L) = g_c + a\, L^{-p}\,, \tag{5.10}$$

$$R_c(L) = R_c + b\, L^{-\omega}\,. \tag{5.11}$$

In accord with the quasi-one-dimensional physics mentioned in the previous section, we find a critical value of $J_1^c = 0.001(1)J_3$ (consistent with zero). Also the extracted value of $R_c = 2.996(2)$ is compatible with the value of $R_c = 3.05(5)$ that we obtain from QMC simulations performed for an isolated spin-1/2 Heisenberg chain (cf. Sec. 5.5). From the fits we extract the correction exponents $\omega \approx 1.40(4)$ and $p \approx 1.21(5)$, which we find to be comparable to the above used estimate for $\omega_2 \approx 1.25$ from Ref. [145]. This suggests a simple explanation for the necessity of the second subleading scaling correction captured by the $L^{-\omega_2}$ term with a crossover effect: If we consider small system sizes, the finite-size behavior is still affected by the influence of the specific fixed-point, corresponding to the

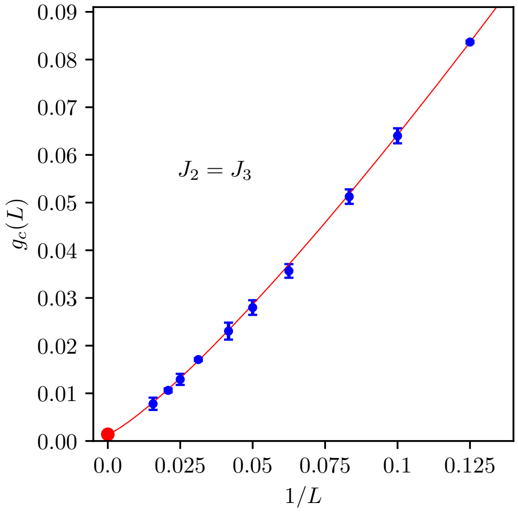

Figure 5.9: Crossing point values of $g = J_1/J_3$ for the Binder ratio R for $J_2 = J_3$ between system sizes L and $2L$. The red line indicates a fit to the finite-size scaling form Eq. (5.10) with the TDL value marked with a red dot. The figure is adapted from Ref. [2].

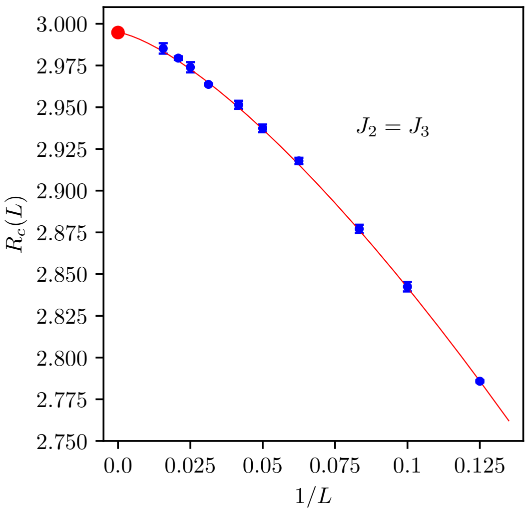

Figure 5.10: Crossing point values of the Binder ratio R for $J_2 = J_3$ between system sizes L and $2L$. The red line indicates a fit to the finite-size scaling form Eq. (5.11) with the TDL value marked with a red dot. The figure is adapted from Ref. [2].

decoupled spin-1/2 Heisenberg chains. Only on sufficiently large system sizes does the actual asymptotic scaling of the three-dimensional classical Heisenberg universality class prevail. We estimate a crossover scale of $L_c \approx 20$ for this scenario based on the local extrema in the finite-size crossing points.

Throughout the scans we notice that the critical Binder ratio R_c varies significantly. We summarize the extrapolated values of R_c as a function of J_2 along the considered branch of the AFM phase boundary line in Fig. 5.11. We observe a clear dependence of the value of R_c on the coupling ratio with the aforementioned tendency towards 3 for $J_2 = J_3$. Interestingly, the obtained values are all substantially larger than the critical value $R_c^{\text{iso}} = 2.0437...$ of the isotropic three-dimensional classical Heisenberg model, without exhibiting any trend to approach this value for the considered coupling ratios. This observation supports previous studies on the effects of anisotropies on the Binder ratio, which are reported to be accompanied by not isotropic correlations in the considered quantum spin systems [158, 159]. In Sec. 5.6 we elaborate on this circumstance.

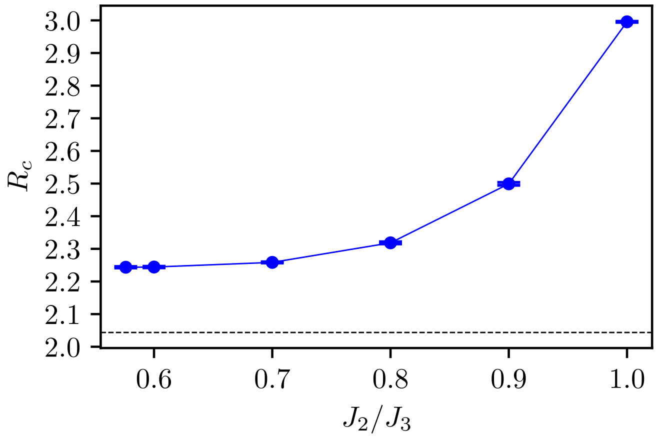

Figure 5.11: Critical Binder ratio R as a function of J_2 along the considered phase transition line. The dashed line indicates the value of the critical Binder ratio $R_c^{\text{iso}} = 2.0437...$ of the isotropic three-dimensional classical Heisenberg model. The figure is adapted from Ref. [2].

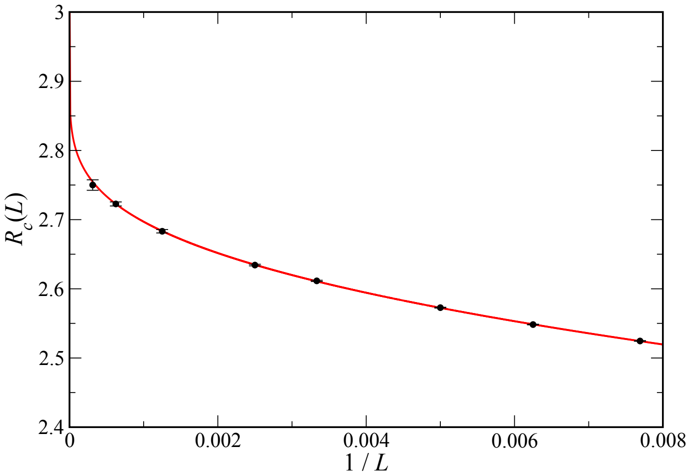

Figure 5.12: Critical Binder ratio $R_c(L)$ for the spin-1/2 Heisenberg chain. The red line indicates a fit according to the finite-size scaling form in Eq. (5.12). The figure is adapted from Ref. [2].

5.5 Binder Ratio of the Spin-1/2 Heisenberg Chain

In order to directly estimate the value of R_c at the singular points of the phase diagram, we performed QMC simulations for an isolated spin-1/2 Heisenberg chain. The finite-size resolved data $R_c(L)$ is displayed in Fig. 5.12. The chains contain L spins up to a size of $L = 3200$ with periodic boundary conditions. We scale the inverse temperature in units of the nearest-neighbor exchange coupling J as $\beta J = L$. We find the values of $R_c(L)$ to be monotonously growing upon increasing the system size. The functional behavior fits well to a logarithmic dependence

$$R_c - R_c(L) \propto (\ln(L))^{-q} \ . \tag{5.12}$$

Performing the fit to the QMC data, we obtain the estimates $R_c = 3.05(5)$ and $q = 1.1(1)$, respectively. The inclusion of a logarithmic finite-size term in the scaling of $R_c(L)$ can be expected due to the known asymptotic spin-spin correlation function behavior of the spin-1/2 Heisenberg chain that decays with distance r as $\sqrt{\ln(r)}/r$ [154]. We are not aware of any previous analytic prediction for the finite-size scaling form of the Binder ratio in this system.

5.6 General Remarks on Anisotropic Systems

By now it is well established that certain dimensionless quantities such as the critical Binder ratio R_c are not universal, but depend on the anisotropy of the correlations [158, 159]. Indeed it is possible to restore the isotropic value R_c^{iso} by considering finite-size systems with appropriate aspect ratios [144]. However, such a restoration has been argued to not be crucial for the analysis of, e.g., the universal properties of the critical point [145]. For instance, consider a finite rectangle consisting of $L_x \times L_y$ unit cells in the respective directions for a simple square lattice geometry. By tuning the aspect ratio $\rho = L_y/L_x$, the critical Binder ratio $R_c(\rho)$ takes on the isotropic value $R_c(\rho^*) = R_c^{\mathrm{iso}}$, even though in general $R_c(1) \neq R_c^{\mathrm{iso}}$. Note that for a quantum critical system, the inverse temperature has to be adapted as well [144]. Such restorations have indeed been demonstrated for various classical and quantum models for which the principal axes of the correlation function align with the axes of the underlying square lattice [144, 159–161]. Based on Ref. [162] we denote, for a general anisotropic two-dimensional system, the angular dependence of the correlations by the angle Ω, which specifies the orientation of the two principal axes. Analogous to the geometric aspect ratio ρ, we introduce the ratio q of the two principal correlation lengths upon approaching criticality. The mentioned restorations are special cases that correspond to $\Omega = 0$ or $\pi/2$, i.e., the principal axes of the correlations are parallel or orthogonal. Taking for example the $\Omega = 0$ case, the value of ρ^* is fixed by the condition that $q\rho^* = 1$, realized e.g., for $q = 2$, such that the correlation length in the x direction is larger than the correlation length in y direction by a factor 2, which means $\rho = 1/2 \Leftrightarrow L_x = 2L_y$. Such systems were labeled by the term ”virtual isotropic” [139, 144]. Considering a more generic case, in which Ω is not limited to specific values, i.e., when the principle axes are not aligned with the lattice directions, two questions arise: (i) is such a restoration possible, which means finding a ρ^*, so that $R_c(\rho^*) = R_c^{\mathrm{iso}}$, and (ii) what is the physical interpretation of the value of ρ^* in that case.

Below, we demonstrate explicitly for an anisotropic, classical model that the restoration of the isotropic value is indeed still possible. However, the value of ρ^* appears in this case to be unrelated to the orientation of the underlying correlations. To this end, we consider the triangular-lattice Ising model [162–165]. The Hamiltonian reads

$$H^{\mathrm{Is}} = -\sum_i \left(E_1\sigma_i\sigma_{i+\hat{x}} + E_2\sigma_i\sigma_{i+\hat{y}} + E_3\sigma_i\sigma_{i+\hat{x}+\hat{y}}\right) , \tag{5.13}$$

where $\sigma_i = \pm 1$. We examine the system on a square lattice with horizontal, vertical, and (up-right) diagonal couplings $E_1, E_2,\ E_3 \geq 0$ (see the left inset of Fig. 5.13 for an illustration of the unitcell). We focus on the symmetric case $E_1 = E_2 = E$, for which $\Omega = \pi/4$ and $q = 1/\hat{S}_3$ with correlations decaying equally in x and y direction [162, 165]. The critical temperature T_c that separates the low-T ferromagnetic phase from the paramagnetic regime, can be determined through the condition $\hat{S}_1\hat{S}_2 + \hat{S}_2\hat{S}_3 + \hat{S}_3\hat{S}_1 = 1$, where $\hat{S}_\alpha = \sinh(2E_\alpha/T_c)$ [166]. Employing Wolff-cluster Monte Carlo simulations [40] at T_c, we report the ρ-dependence of the critical Binder cumulant [152]

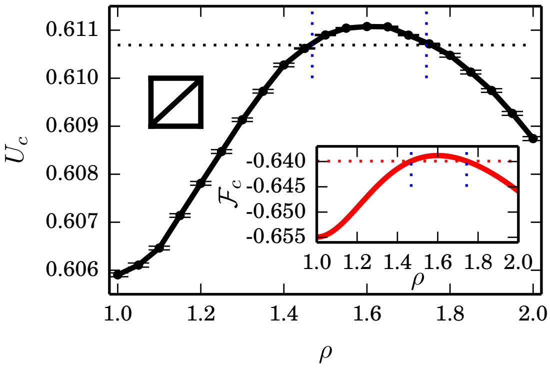

Figure 5.13: Aspect ratio ρ dependence of the critical Binder cumulant U_c and the critical amplitude of the singular free energy density $\mathcal{F}_c$ in the inset for the anisotropic Ising model with $E_3 = 3E$. The horizontal lines indicate the isotropic values and the vertical lines indicate the two values of ρ^*. The left inset illustrates the unit cell with E_1, E_2, E_3 along horizontal, vertical and diagonal directions, respectively. The figure is adapted from Ref. [2].

$$U_c = 1 - \frac{1}{3}R_c, \quad R_c = \frac{\langle M^4\rangle}{\langle M^2\rangle^2} , \tag{5.14}$$

where $M = \sum_i \sigma_i$, for the specific case of $E_3 = 3E$ extracted for the thermodynamic limit in Fig. 5.13. The value of U_c obtained for $\rho = 1$ agrees with an earlier study [159]. In the standard Ising model ($E_1 = E_2$, $E_3 = 0$) $U_c(\rho)$ decreases monotonously for $\rho > 1$ from the isotropic value $U(\rho = 1) = U_c^{\mathrm{iso}} = 0.61069...$ [160]. Contrary to the standard case, we find a nonmonotonous behavior in our specific case. In particular, we restore the isotropic value U_c^{iso} for two aspect ratios $\rho^* \approx 1.47$ and 1.74. Within numerical precision these values agree with the values of ρ for which the critical amplitude of the singular free energy density $\mathcal{F}_c(\rho)$ recovers its isotropic value $\mathcal{F}_c^{\mathrm{iso}} = -0.639912...$ [167] (cf. the inset of Fig. 5.13). However, we cannot draw an apparent relation between these ρ values and the value of $q = 2.82843...$. Based on expressions for $\mathcal{F}_c$ employing exact conformal field theory, we are able to compute ρ^* for the latter quantity [164, 165]. For $E_3 = 3E$, we obtain $\rho^* = 1.4683...$ and $1.7433...$. The above observations have been made also at other ratios E_3/E (see Ref. [161] for the specific case $E_3 = E$), resulting in different values of ρ^*. This suggests (i) it is feasible to restore the isotropic values of both the critical Binder cumulant and the critical amplitude of the singular free energy density upon varying the aspect ratio ρ for the considered anisotropic Ising model, (ii) the corresponding values of ρ^* for both quantities are equal within numerical precision and (iii) we do not find an evident relation of these values with the geometric properties of the anisotropic correlation functions for $\Omega \neq 0, \pi/2$. We argue that once the principal axes are not aligned to the underlying lattice directions, one cannot expect to be able to relate, as in previous cases [144, 159, 160], the value of ρ^* directly to (i) the correlation length ratio along the lattice directions, which in the above considered Ising model cases equals to 1, since $E_1 = E_2$, nor to (ii) the ratio q of the two principal correlation lengths. Regarding the above studied quantum system, it is thus not clear, how and if the procedure proposed in Ref. [144] to determine the location of ρ^* can be generalized to the fully anisotropic case. Certainly, this leaves room for further studies of the triangular-lattice Ising model, as well as more general systems.

5.7 Conclusion

Based on large-scale quantum Monte Carlo simulations we determined the ground state phase diagram of the spin-1/2 Heisenberg model on the honeycomb lattice for the most generic case of three anisotropic nearest-neighbor exchange interactions. The AFM phase separates three quantum disordered regimes, each characterized by a dominant dimer singlet formation along the strongest bonds. These dimer phases touch at three singular points in the limit of one vanishing coupling with equal strength in the remaining two.

Similar to the previously investigated staggered dimer model [145], we find nonmonotonic, anomalous finite-size corrections at the quantum phase transition along the boundary line of the AFM regime. Utilizing a scaling ansatz with two irrelevant scaling correction terms, we were able to capture the scaling behavior well. The additional scaling correction is subdominant to the leading finite-size correction that relates to the three-dimensional O(3) universality class. The scaling ansatz changes upon approaching the aforementioned singular points. The system decouples into parallel spin-1/2 Heisenberg (zig-zag) chains, for which we used a similar finite-size correction term, but only to *leading* order. As an explanation for the nonmonotonic scaling behavior we propose a crossover scenario of spe-

cific fixed-points of the different finite sizes smaller and larger than $L \approx 20$.
In this context it is noteworthy that the cubic interaction term in the effective low-energy field theory, previously proposed to underlie the anomalous scaling, observed in the staggered dimer model [143], has a formal similarity with the topological θ-term that is characteristic for the gapless state of the spin-1/2 Heisenberg chain [154]. Haldane conjectured that the ground state of integer-spin AFM Heisenberg chains has a gapped ground state, whereas half-odd-integer-spin Heisenberg chains exhibit gapless excitations, based on the mapping of one-dimensional Heisenberg chains onto the (1+1)-dimensional O(3) nonlinear sigma model field theory [168, 169]. Here, the relevant detail is the addition of a spin-S dependent cubic interaction term to a quadratic term in the effective action. The additional topological term takes the form

$$S_3 = i2\pi S\theta \,, \tag{5.15}$$

where θ contains cubic interactions and returns an integer value [170, 171]. In the case of half-odd-interger-spin chains, the contribution of any field configuration into the partition function carries a non-trivial phase factor $\mathrm{e}^{-i2\pi S\theta}$, which ultimately leads to a gapless spectrum [171]. Thus, the link between the subleading scaling correction and the behavior at the one-dimensional singular points requires more in-depth investigation in appropriate generalizations of the staggered dimer model.
Finally, we discussed the previously proposed schemes [144] for the automated restoration of isotropic values of cumulant ratios and argue that it is not directly applicable to generic anisotropic systems, even in cases for which such a restoration may be feasible. For the future it would be interesting to explore proper applications and limitations of the restoration schemes.

Quantum Heisenberg Model on the Diamond Lattice

6

We report quantum Monte Carlo calculations employing the SSE scheme for the spin-1/2 Heisenberg model on the diamond lattice with both antiferromagnetic as well as ferromagnetic nearest-neighbor exchange coupling. We determine the Néel temperature T_N and the Curie temperature T_C from a finite-size analysis of the temperature resolved Binder ratio. The comparison shows $T_N > T_C$, which we discuss with regard to the stability of the FM and AFM against fluctuations based on the respective temperature resolved entropy.

The results in this chapter constitute the QMC analysis of a collaborative work in preparation. My contributions are the presented SSE simulations (except Fig. 6.8 - performed by Stefan Wessel), which are motivated by discussions with Yasir Iqbal (IIT Madras), Yannik Schaden (FU Berlin), Johannes Reuter (FU Berlin), Andreas Honecker (CY Cergy Paris Université) and Stefan Wessel.

6.1 Motivation

The quantum Heisenberg model is one of the most important models in condensed matter physics. A wide variety of physical behavior can be realized, depending on the underlying lattice geometry for both ferromagnetic and antiferromagnetic coupling. On a one-dimensional spin-1/2 chain the ferromagnetic ground state exhibits long range order [154], whereas the antiferromagnetic ground state exhibits critical fluctuations [168]. The ground states in two dimensions on a square lattice is ordered in both cases [172–174]. These ordered states are destroyed by thermal fluctuations for any $T > 0$ in one and two spatial dimensions [20]. In three dimensions, quantum fluctuations are suppressed relative to thermal fluctuations and a finite critical temperature $T_c > 0$ is expected with a critical behavior according to the classical three-dimensional Heisenberg universality class [175]. Critical properties have been successfully obtained by means of a high-temperature expansions for various two- and three-dimensional lattices [176–178] among which the diamond lattice can be found [179]. Further analytical, approximative calculations have been carried out for three dimensional lattices [180, 181] as well as QMC studies [182–184] on a variety of systems. Here, we support the exploration of the diamond lattice magnetism realized in the material class of A-site spinels [185–189]. Although these systems typically suffer from frustration due to extended interactions, thus prohibiting a direct access for the SSE [23–25], a profound analysis of the unfrustrated diamond lattice forms the basis of further studies. We report detailed QMC calculations aimed at reliably extracting the critical temperatures for both the ferromagnetic and antiferromagnetic spin-1/2 Heisenberg model on the diamond lattice as well as providing unbiased results for the temperature dependence of the respective entropy.

6.2 Quantum Heisenberg Model

We consider the spin-1/2 Heisenberg model with isotropic interaction strength J between the nearest-neighbor bonds, with $J > 0$ ($J < 0$) in the antiferromagnetic (ferromagnetic) case, described by the Hamiltonian

$$H = J \sum_{\langle i,j \rangle} \mathbf{S}_i \cdot \mathbf{S}_j \,, \tag{6.1}$$

where $\mathbf{S}_i$ denotes the spin degree of freedom on a lattice site i. The diamond lattice consists of two intertwined face centered cubic (FCC) lattices with a relative shift of 1/4 along the room diagonal (the lattice constant is set to $a = 1$). This results in a bipartite lattice, in which one site resides on the coordinates $(0,0,0)$ and the other at

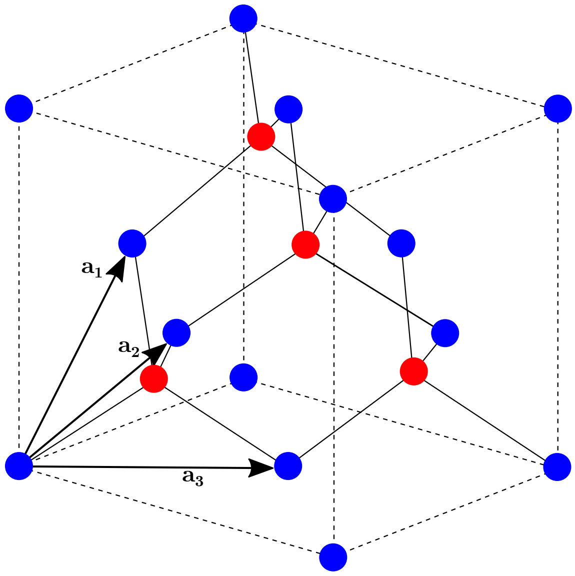

Figure 6.1: The diamond lattice with its bipartite structure, indicated by two differently colored lattice sites. Included is the unit cell spanned by the lattice vectors $\mathbf{a}_1$, $\mathbf{a}_2$ and $\mathbf{a}_3$.

$1/4(1,1,1)$ in the unitcell as shown in Fig. 6.1. From a previous study employing a high-temperature expansion the Néel and Curie temperature are estimated to $T_N/J = 0.531(1)$ and $T_C = 0.447(1)$, respectively [179]. Furthermore, this model has been studied on the simple cubic lattice [184], which is a perfect starting point to access the effects arising in more complex structures, such as the bipartite diamond lattices presented here.
We performed large-scale QMC simulations based on the SSE scheme with directed loop updates. We have simulated several finite-size systems up to a linear dimension of $L = 32$ with periodic boundary conditions, resulting in a total of $N = 2L^3$ number of spins. The computations have been performed in a temperature range of $T/|J| \approx 0.43 - 0.53$ to extract the crossing points of the temperature resolved Binder ratio [152]

$$R = \frac{\langle M^4_{(s)} \rangle}{\langle M^2_{(s)} \rangle^2}\,, \tag{6.2}$$

where $\langle M^x_s \rangle = \langle (\sum_i \epsilon_i S^z_i)^x \rangle$ ($\epsilon_i = \pm 1$ dependent on the sublattice) denotes the staggered moment of the order parameter distribution in the antiferromagnetic case and $\langle M^x \rangle = \langle (\sum_i S^z_i)^x \rangle$ in the ferromagnetic case. Taking a scaling ansatz of the form

$$\begin{aligned} T_c(L) &= T_c + L^{-1/\nu}(a_1 L^{-\omega} + a_2 L^{-2\omega})\,, &(6.3)\\ R_c(L) &= R_c + b_1 L^{-\omega} + b_2 L^{-2\omega}\,, &(6.4) \end{aligned}$$

where $1/\nu = 1.406$ and $\omega = 0.78$ are exponents in the O(3) classical Heisenberg universality class [155–157], we determine the critical temperatures upon extrapolating to the TDL. In order to extract the temperature dependence of the entropy, we obtain the internal energy over a very high temperature range of $T/|J| = 0.01 - 1000$ and perform a thermodynamic integration (cf. Sec. 3.2) based on the relations for the free energy $F = E - TS$, $F = -T\ln(Z)$ and the internal energy $E = -\partial_\beta \ln(Z)$:

$$S = \beta E(\beta) + \ln(2) - \int_0^\beta \mathrm{d}\beta' E(\beta')\,, \tag{6.5}$$

where ln(2) is the is the upper bound of the entropy (per site) in the $T \to \infty$ limit. The statistical error is estimated through a simple bootstrap scheme, where we repeatedly evaluate the integral by fluctuating the energy values within their respective errorbars according to a Gaussian distribution.

6.3 Thermal Phase Transitions

In Fig. 6.2 (AFM) and Fig. 6.3 (FM), we present the QMC results for the Binder ratio for both the antiferromagnetic and the ferromagnetic Heisenberg model for lattice sizes up to $L = 32$. For the AFM case the crossing points of the $(L, 2L)$ finite-size data pairs seem to converge around $T/|J| \approx 0.5275$, whereas in the FM case for $T/|J| \approx 0.444$. Both values are already in the vicinity of T_N and T_C obtained with the high-temperature expansion approach [179]. In the next step we extrapolate the finite-size crossing points to the thermodynamic limit according to the scaling laws in Eq. (6.3) and Eq. (6.4) from the O(3) Heisenberg universality class. The scaling laws are expected to fit well, since quantum fluctuations are suppressed by classical, thermal fluctuations. From the analysis shown in Fig. 6.4 and Fig. 6.5 we extract $R_c^N = 2.028(2)$ and $R_c^C = 2.042(1)$. Finally, we obtain the Néel temperature $T_N = 0.52782(5)$ for the AFM case (see Fig. 6.6) and the Curie temperature $T_C = 0.44447(4)$ for the FM case (see Fig. 6.7), respectively. Compared to the simple cubic case [184], we find both phases, where an order stabilizes, to be less robust against thermal fluctuations. The Néel (Curie) temperature is reduced by approximately 44% (47%) with respect to the simple cubic lattice [184]. Furthermore, we report data in Fig. 6.8 for the staggered (uniform) susceptibility in the AFM (FM) cases, which is computed by $\chi = \beta\langle M_{(s)}^2\rangle$ within the SSE formulation. Until numerically not distinguishable, χ^{AFM} remains larger than χ^{FM}, which indicates the AFM order to be more robust against thermal fluctuations.

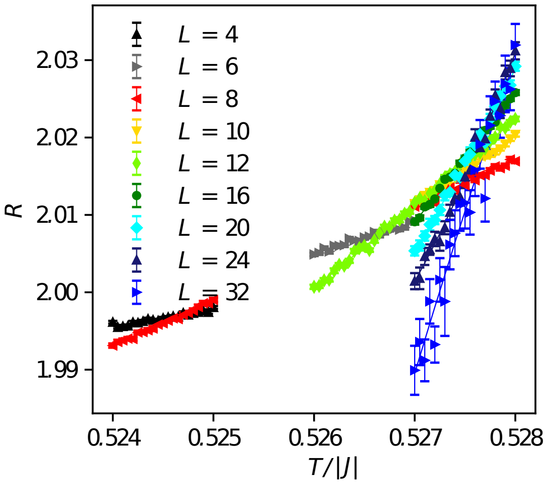

Figure 6.2: Binder ratio R as a function of $T/|J|$ for different system sizes L in the AFM case.

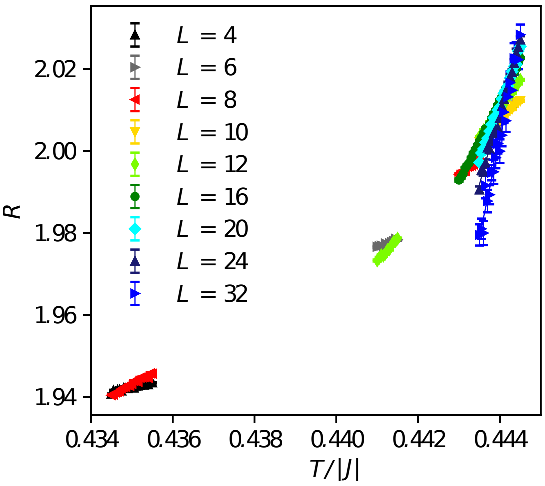

Figure 6.3: Binder ratio R as a function of $T/|J|$ for different system sizes L in the FM case.

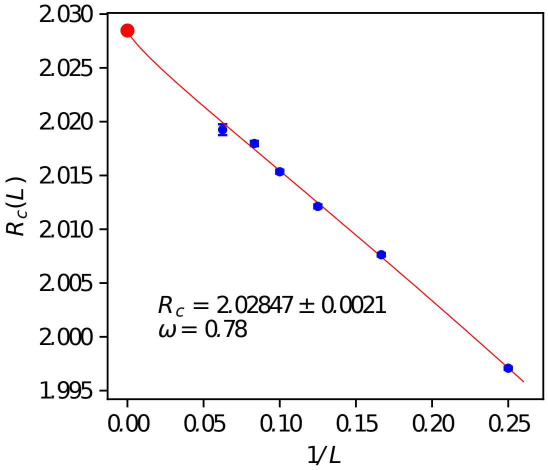

Figure 6.4: Crossing point values of the Binder ratio R between system sizes L and $2L$ for the AFM. The red line indicates a fit to the finite-size scaling form Eq. (6.4) with the TDL value marked with a red dot.

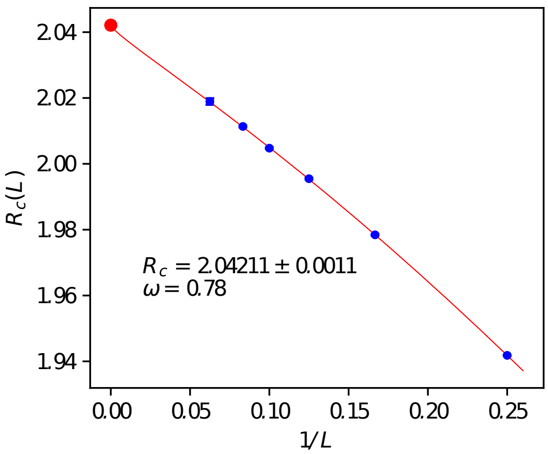

Figure 6.5: Crossing point values of the Binder ratio R between system sizes L and $2L$ for the FM. The red line indicates a fit to the finite-size scaling form Eq. (6.4) with the TDL value marked with a red dot.

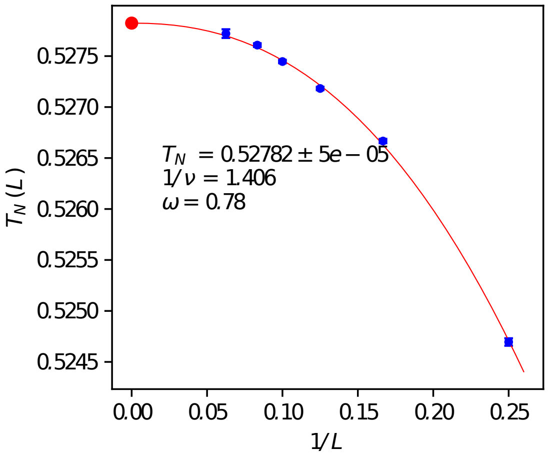

Figure 6.6: Crossing point values of T for the Binder ratio R between system sizes L and $2L$ for the AFM. The red line indicates a fit to the finite-size scaling form Eq. (6.3) with the TDL value marked with a red dot.

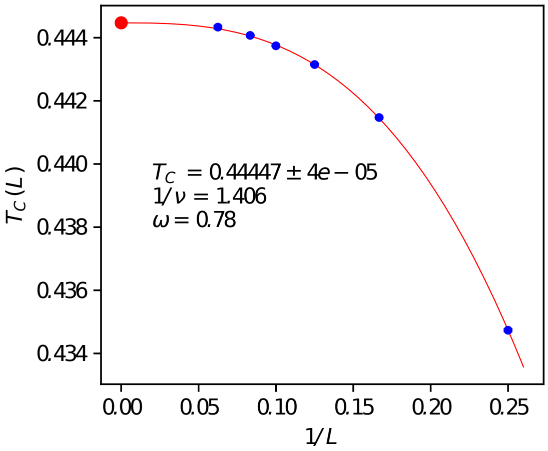

Figure 6.7: Crossing point values of T for the Binder ratio R between system sizes L and $2L$ for the FM. The red line indicates a fit to the finite-size scaling form Eq. (6.3) with the TDL value marked with a red dot.

To understand why upon heating, the ferromagnetic order is destroyed earlier than the antiferromagnetic one ($T_C/T_N \approx 0.84$), we examine the entropy density at accessible, low temperatures, i.e. the entropy per lattice site. Finite-size effects are marginal for this

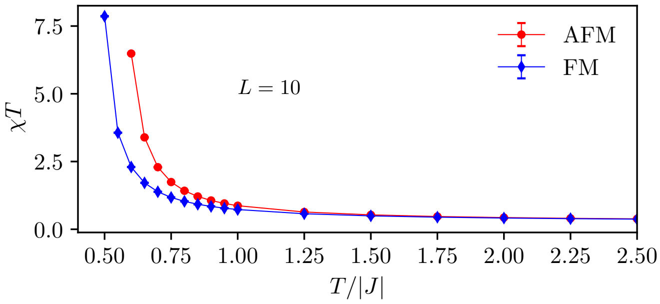

Figure 6.8: Temperature dependence of the staggered (AFM) and uniform (FM) susceptibility for the spin-1/2 quantum Heisenberg on the diamond lattice. Results from the QMC simulations are shown for $L = 10$.

quantity, so that we simulate the system in both cases for a linear dimension of $L = 8$ as a representative for the TDL behavior. The data is reported in Fig. 6.9, which also includes fits to the low-T scaling $S \sim T^3$ ($S \sim T^{3/2}$) for the antiferromagnet (ferromagnet). The respective low temperature behavior is described by the linear (quadratic) dispersion of the spin-wave excitations in the AFM (FM) case [170]. The significantly enhanced production

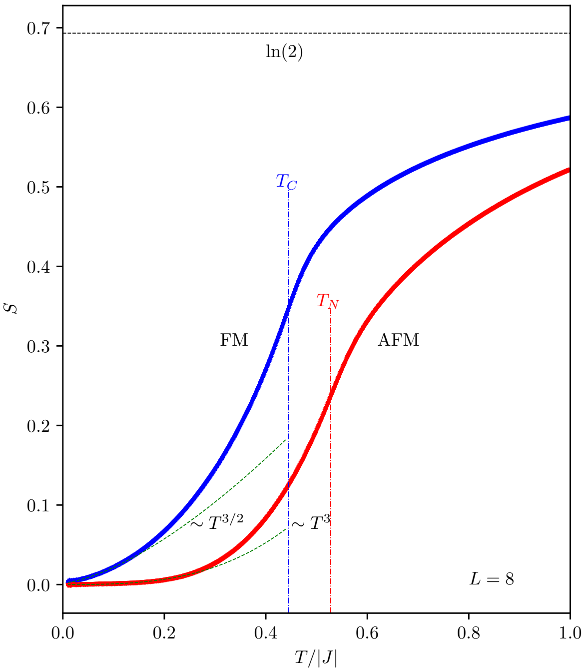

Figure 6.9: Temperature dependence of the entropy for the spin-1/2 quantum Heisenberg on the diamond lattice. Results from the QMC simulations are shown for $L = 8$. Vertical lines indicate the transition temperatures T_N and T_C for the antiferromagnet and the ferromagnet, respectively. The green dashed curves denote fits to the algebraic low-T scaling $S \sim T^3$ ($S \sim T^{3/2}$) for the AFM (FM).

of entropy upon heating up the system, observed in the FM case, gives a natural explanation for the lower transition temperature: a higher entropy increase destroys magnetic order faster. This circumstance is affirmed by the low-energy dispersion of the spin-wave theory.

6.4 Conclusion

From QMC simulations based on the SSE formulation with directed loop updates, we obtained the phase transition temperatures, the temperature dependence of the entropy and the staggered and uniform susceptibility for both the antiferromagnetic and the ferromagnetic spin-1/2 Heisenberg model on the diamond lattice. We find a decrease in the transition temperatures by 44% (AFM) and 47% (FM), respectively, compared to the simple cubic case [184], which we can attribute to the lower coordination number of the diamond lattice. Hence, the ordered states are less robust against thermal fluctuations. Comparing the individual temperature resolved entropies and susceptibilities on the diamond lattice, we observe that the entropy gain upon heating in the FM case is significantly larger than in the AFM case, while the uniform susceptibility is smaller than its staggered counter part. This behavior and the low-energy spin-wave dispersion give a plausible explanation for the lower transition temperature of the ferromagnet.

Extending the interactions to next-nearest neighbor, one can examine qualitatively more realistic models that are more suitable to study experimentally realized materials, such as A-site spinels. Unfortunately, SSE suffers from a sign problem in this setup prohibiting a direct analysis. Therefore, other methods, e.g. PF/PM FRG [190], have to be employed. However, the current status of the ongoing investigation with a PMFRG approach on the given model yields similar temperature values, but in opposite order, i.e., PMFRG predicts $T_C > T_N$. To further investigate the robustness and proliferation of magnetic order (especially either AFM or FM is more stable), an interesting lattice geometry is the hyperhoneycomb lattice, i.e. the generalized honeycomb lattice to three spatial dimensions. It has an even lower coordination number than the diamond lattice, thus it is expected to have lower transition temperatures, while retaining a similar low-T entropy scaling. To come back to the discussion in the previous chapter 5, one can examine the spin-1/2 Heisenberg model on the diamond lattice, as a three-dimensional bipartite example, regarding the restoration scheme of isotropic moment ratios upon introducing an anisotropic coupling between the two sites in the diamond unit cell.

Conclusion and Outlook

7

We already drew conclusions at the end of each individual chapter. Here, we briefly summarize these conclusions and make some additional remarks.

Starting with the exploration of non-local interaction extensions to the Hubbard model with finite-temperature DQMC in Chap. 3, we find for both the U-V and LRC-Hubbard model an overall enhancement of the double occupancy in the presence of finite extended interactions and identify an associated increase of the entropy within the low-temperature regime. In contrast to Ref. [109], both our finite-size data as well as the extrapolated TDL limit values do not provide any evidence for the presence or the onset of a discontinuity in D or S. We observe a (weak) peak emerging in the temperature dependence of the double occupancy D as we approach the limiting value of $V = U/4$ for the U-V model. This might be explained by the enhancement of local density fluctuations in the vicinity of the thermal critical point of the CDW order that emerges for sufficiently large values of V. Unfortunately, this regime lies beyond the accessibility of sign-problem free DQMC. In Fig. 3.9 we propose qualitative phase diagrams of the U-V model, which might be supported by further studies, e.g., with tensor network approaches, in the high-V/U regime.

Extended interactions in the Hubbard model continue to play a role in Chap. 4, where we study magnetic properties of ABCA stacked tetra-layer graphene. We explore the U dependence of the staggered magnetization on the finite lattice and find an indication of a transition into a AFM phase at $U/t \approx 5.3$. Due to the immense computational cost, we cannot access larger lattices, so that a stable extrapolation to the TDL is not feasible. For a realistic description of graphene tetra-layers, we added an extended U' interaction between the topmost 1-sites and the bottommost 8-sites. A finite U' seems to shift the transition point to higher values of U and we can expect a similar proliferation of a charge density order as for the U-V model. Indeed, based on mean-field calculations, the onset of an insulating charge transfer order, which we associate with a charge density wave, is predicted at $U' \gtrsim U$ [119]. To examine this idea further, the measurement of the single-particle gap and the dynamic magnetic susceptibility would be beneficial. Again larger extended interactions are not accessible. We conclude that, at least for the investigated systems, a non-local interaction beyond the regime accessible to sign-problem free DQMC is responsible for a discrete symmetry breaking to a charge ordered state in the extended models.

In Chap. 5 we determine the ground state phase diagram of the Heisenberg model on the honeycomb lattice with three anisotropic nearest-neighbor exchange interactions and find that an AFM phase separates three quantum disordered dimer regimes. Similar to the previously investigated staggered dimer model [145], we find nonmonotonic, anomalous finite-size corrections at the quantum phase transition. We explain this behavior by the discussed crossover scenario. We find a drastic change in the scaling behavior in the limit of decoupled one-dimensional zig-zag chains and note that the link between the subleading scaling correction and the behavior at the one-dimensional singular points requires more in-depth investigation. Furthermore, we discuss previously proposed schemes [144] for the automated restoration of isotropic values of cumulant ratios and argue that it is not directly applicable to generic anisotropic systems.

Finally, we turned to a three-dimensional lattice. We obtained the phase transition temperatures, the temperature resolved entropy and the staggered (uniform) susceptibility for the antiferromagnetic (ferromagnetic) spin-1/2 Heisenberg model on the diamond lattice. We find the Néel temperature to be higher than the Curie temperature, which we can understand based on the entropy gain upon heating, i.e., in the FM case it is significantly larger than in the AFM case. To study experimentally realized materials, such as A-site spinels, we need to extend the couplings to next-nearest neighbors, which would lead to a sign-problem in the SSE. Therefore, different approaches, e.g. PF/PM FRG [190], have to be considered. With regard to the anisotropies investigated in Chap. 5, the Heisenberg model on the diamond lattice, as a three-dimensional bipartite representative, can be an interesting system to study the (anomalous) scaling behavior as well. Furthermore, to investigate the robustness and the relative temperatures of the ordered states, one can examine the hyperhoneycomb lattice with its lower coordination number. The expectation is that the transition temperatures reduce, while a similar low-T entropic gain emerges.

Appendix

A

A.1 DQMC

A.1.1 Suzuki-Trotter Decomposition

This section follows the outline of the appendix 10.A of Ref. [41]. Given a Hamiltonian of the form

$$H = H_1 + H_2 \,, \tag{A.1}$$

the Suzuki-Trotter decomposition allows us to split the imaginary time propagator into a product of infinitesimal small time propagations:

$$\mathrm{e}^{-\beta H} = \lim_{\Delta\tau \to 0} \left(\mathrm{e}^{-\Delta\tau H_1} \mathrm{e}^{-\Delta\tau H_2} \right)^{L_T} \quad , \tag{A.2}$$

where we discretize the inverse temperature $\beta = L_T \Delta\tau$. In general the commutator $[H_1, H_2] \neq 0$ and in QMC simulations we fix the time slice "thickness" $\Delta\tau$ to a small, but finite value. This introduces a systematic error in $\Delta\tau$:

$$\mathrm{e}^{-\Delta\tau(H_1+H_2)} = e^{-\Delta\tau H_1} \mathrm{e}^{-\Delta\tau H_2} - \frac{\Delta\tau^2}{2}[H_1, H_2] + \mathcal{O}(\Delta\tau^3) \,. \tag{A.3}$$

This equation stems from the comparison of the Taylor expansions of the exponential functions in Eq. (A.2) up to third order:

$$\begin{aligned}
\mathrm{e}^{-\Delta\tau(H_1+H_2)} &= 1 - \Delta\tau(H_1 + H_2) + \frac{\Delta\tau^2}{2}(H_1 + H_2)^2 + \mathcal{O}(\Delta\tau^3) \\
&= 1 - \Delta\tau(H_1 + H_2) + \frac{\Delta\tau^2}{2}(H_1^2 + H_2^2 + 2H_1H_2 - [H_1, H_2]) + \mathcal{O}(\Delta\tau^3) \,, \\
\mathrm{e}^{-\Delta\tau H_1} \mathrm{e}^{-\Delta\tau H_2} &= (1 - \Delta\tau H_1 + \frac{\Delta\tau^2}{2} H_1^2)(1 - \Delta\tau H_2 + \frac{\Delta\tau^2}{2} H_2^2) \\
&= 1 - \Delta\tau(H_1 + H_2) + \frac{\Delta\tau^2}{2}(H_1^2 + H_2^2 + 2H_1H_2) + \mathcal{O}(\Delta\tau^3) \,.
\end{aligned}$$

Subtracting the commutator initially in the exponent of the left hand side in Eq. (A.3) and taking both sides to the power of L_T we arrive at

$$\mathrm{e}^{-\beta(H - \frac{\Delta\tau}{2}[H_1, H_2])} = \left[\mathrm{e}^{-\Delta\tau H_1} \mathrm{e}^{-\Delta\tau H_2} \right]^{L_T} + \mathcal{O}(\Delta\tau^2) \,. \tag{A.4}$$

Note that the resulting error is of order $\Delta\tau^2$, since it is exponentiated too.
To evaluate the left hand side we use time dependent perturbation theory. Given a Hamiltonian $h = h_0 + h_1$, where h_1 is much smaller than h_0, the imaginary time propagation in the interaction picture reads

$$U(\tau) = \mathrm{e}^{\tau h_0}\mathrm{e}^{-\tau h}\,. \tag{A.5}$$

The time derivative results in

$$\begin{aligned}\frac{\partial}{\partial\tau}U(\tau) &= \mathrm{e}^{\tau h_0}(h_0 - h)\mathrm{e}^{-\tau h} = -\underbrace{\mathrm{e}^{\tau h_0}h_1\mathrm{e}^{-\tau h_0}}_{=h_1(\tau)}U(\tau)\\ &= -h_1(\tau)U(\tau)\,.\end{aligned} \tag{A.6}$$

Integrating both sides, with $U(0) = \boldsymbol{I}$, the above equation transforms into a self consistent integral equation

$$U(\tau) = \boldsymbol{I} - \int_0^\tau \mathrm{d}\tau'\, h_1(\tau')U(\tau') = \int_0^\tau \mathrm{d}\tau'\, h_1(\tau') + \mathcal{O}(h_1^2)\,. \tag{A.7}$$

Coming back to Eq. (A.4), we set $h_0 = H$, $h_1 = -\frac{\Delta\tau}{2}[H_1, H_2]$ and $\tau = \beta$ to obtain

$$\begin{aligned}&\mathrm{e}^{-\beta(H-\frac{\Delta\tau}{2}[H_1,H_2])} + \mathcal{O}(\Delta\tau^2)\\ &= \mathrm{e}^{-\beta H} + \frac{\Delta\tau}{2}\underbrace{\int_0^\beta \mathrm{d}\tau\,\mathrm{e}^{-(\beta-\tau)H}[H_1, H_2]\mathrm{e}^{-\tau H}}_{=A} + \mathcal{O}(\Delta\tau^2)\\ &= \left(\mathrm{e}^{-\Delta\tau H_1}\mathrm{e}^{-\Delta\tau H_2}\right)^{L_T} + \mathcal{O}(\Delta\tau^2)\,.\end{aligned} \tag{A.8}$$

The ultimate goal is to compute the thermal expectation value of an observable $O = O^\dagger$:

$$\frac{\mathrm{Tr}\left[\left(\mathrm{e}^{-\Delta\tau H_1}\mathrm{e}^{-\Delta\tau H_2}\right)^{L_T} O\right]}{\mathrm{Tr}\left[\left(\mathrm{e}^{-\Delta\tau H_1}\mathrm{e}^{-\Delta\tau H_2}\right)^{L_T}\right]} = \frac{\mathrm{Tr}\left[\mathrm{e}^{-\beta H}O\right] + \frac{\Delta\tau}{2}\mathrm{Tr}[AO]}{\mathrm{Tr}\left[\mathrm{e}^{-\beta H}\right] + \frac{\Delta\tau}{2}\mathrm{Tr}[A]} + \mathcal{O}(\Delta\tau^2)\,. \tag{A.9}$$

It can be shown that A is an anti-Hermitian operator by substituting $\tau = \beta - \tau'$:

$$\begin{aligned}A^\dagger &= -\int_0^\beta \mathrm{d}\tau\,\mathrm{e}^{-\beta H}[H_1, H_2]\mathrm{e}^{-(\beta-\tau)H}\\ &= \int_\beta^0 \mathrm{d}\tau'\,\mathrm{e}^{-(\beta-\tau')H}[H_1, H_2]\mathrm{e}^{-\tau' H} = -A\,.\end{aligned} \tag{A.10}$$

Due to the anti-hermiticity of A, the following relations hold: $[\mathrm{Tr}(A)]^* = \mathrm{Tr}(A^\dagger) = -\mathrm{Tr}(A)$ and $[\mathrm{Tr}(AO)]^* = -\mathrm{Tr}(AO)$. If O, H_1 and H_2 are real representable in a given basis, the trace becomes real and the linear term in $\Delta\tau$ in Eq. (A.10) vanishes due to the properties of A. Hence, the leading correction in the systematic Trotter error is in the order of $\Delta\tau^2$.

The decomposition can be carried out in other forms, which results in the same or even smaller corrections. For example another commonly used case is a symmetric decomposition:

$$\mathrm{e}^{-\Delta\tau(H_1+H_2)} = \mathrm{e}^{-\Delta\tau/2H_1}\mathrm{e}^{-\Delta\tau H_1}\mathrm{e}^{-\Delta\tau/2H_2} + \mathcal{O}(\Delta\tau^3)\,. \tag{A.11}$$

However, better numerical precession is often accompanied by higher computational costs.

A.1.2 Hubbard-Stratonovich Transformation

To decouple the electron-electron interaction we use a Hubbard-Stratonovich (HS) transformation. This creates an electron-field interaction, where each charge degree of freedom is locally coupled to a bosonic field. The discrete version used for the U-V model is based on the evaluation of a Gaussian integral [191]. The interactions are brought in bilinear form resulting in

$$\mathrm{e}^{A^2/2} = \frac{1}{\sqrt{2\pi}}\int \mathrm{d}\phi\,\mathrm{e}^{-\phi^2/2-A\phi}\,, \tag{A.12}$$

where A is an operator and $\phi = \phi(\mathbf{r},\tau)$ is a space and imaginary time dependent field. There are different formulations of the discretization dependent on the problem. It has been demonstrated that it is sufficient to use two distinct field values enabling the possibility of an Ising-like sampling procedure [192].
In our simulations we use a more general formulation that preserves the SU(2) symmetry of the U-V model [193]. For a squared operator A describing the charge-charge interaction the transformation on any time slice reads

$$\mathrm{e}^{\Delta\tau\lambda A^2} = \sum_{l=\pm1,\pm2}\gamma(l)\mathrm{e}^{\sqrt{-\Delta\tau\lambda}\eta(l)A} + \mathcal{O}(\Delta\tau^4)\,, \tag{A.13}$$

where the fields γ and η take the values

$$\gamma(\pm1) = 1+\sqrt{6}/3, \quad \eta(\pm1) = \pm\sqrt{2\left(3-\sqrt{6}\right)} \tag{A.14}$$

$$\gamma(\pm2) = 1-\sqrt{6}/3, \quad \eta(\pm2) = \pm\sqrt{2\left(3+\sqrt{6}\right)}\,. \tag{A.15}$$

The advantage of this formulation is that it preserves the generalized SU(N) spin symmetry for each HS-field configuration explicitly [42]. Overall, the transformation produces an error in the order of magnitude of $\mathcal{O}(\Delta\tau^3)$, since it is used L_T times before a measurement. However, this error will be neglected as the Trotter error is already one order of magnitude bigger.

For the LRC-model we cannot use the discretized version since the addition of further interacting bonds would results in a renormalized $\tilde{U}$ that is either limited to a very narrow value range or leads to the fermionic sign problem. The transformation for long range interactions V_{ij}, given by

$$V_{ij} = U \begin{cases} 1 & \text{, for } i = j \\ \frac{\alpha}{d_{ij}} & \text{, for } i \neq j \end{cases} , \tag{A.16}$$

follows Ref. [42]. Here, U is the on-site interaction strength, α a real number monitoring the Coulomb tail and d_{ij} the minimal distance between two lattice sites. On a torus, i.e. with periodic boundary conditions, we have to be careful defining this distance properly. We use a continuous HS decomposition with a symmetric and positive definite matrix V_{ij}:

$$\mathrm{e}^{-\Delta\tau A} \propto \int \prod_i \mathrm{d}\phi_i \mathrm{e}^{-\frac{\Delta\tau}{2}\sum_{ij}\phi_i V_{ij}^{-1}\phi_j - \sum_i i\Delta\tau\phi_i(n_i-1)} , \tag{A.17}$$

where ϕ_i is a local field component. The partition function can be decomposed into a "bosonic" part W_B containing the field information and a "fermionic" part W_F containing the single-fermion terms in the Hamiltonian:

$$Z \propto \int \prod_i \mathrm{d}\phi_{i,\tau} \underbrace{\mathrm{e}^{-\frac{\Delta\tau}{2}\sum_{ij}\phi_i V_{ij}^{-1}\phi_j}}_{W_B(\phi)} \underbrace{\mathrm{Tr}\left[\prod_\tau \mathrm{e}^{-\Delta\tau H_T}\mathrm{e}^{-\sum_i i\Delta\tau\phi_i(n_i-1)}\right]}_{W_F(\phi)} . \tag{A.18}$$

It is convenient to work in basis where V is diagonal

$$D = \mathrm{diag}(\lambda_1, \lambda_2, \dots) = U^T V U , \tag{A.19}$$

with the unitary matrix U containing the eigenvectors of V. Furthermore, We transform the fields in the diagonal basis

$$\eta_{i\tau} = \sum_j U_{ij}^T \phi_{j\tau} . \tag{A.20}$$

On a given timeslice τ_m we propose a configuration update $C \to C' = C(\eta')$ with the probability

$$P(C \to C') = \begin{cases} \prod_i \left[p_a P_B(\eta'_{i\tau_m}) + (1-p_a)\delta(\eta_{i\tau_m} - \eta'_{i\tau_m})\right] & \text{, for } \tau = \tau_m \\ \delta(\eta_{i\tau} - \eta'_{i\tau}) & \text{, for } \tau \neq \tau_m \end{cases} , \tag{A.21}$$

where $P_B(\eta_{i\tau}) = \mathrm{e}^{-\frac{\Delta\tau}{2\lambda_i}\eta_{i\tau}^2}$, $p_a \in [0,1]$ and δ is the Dirac δ-function. p_a is a free parameter to tune the acceptance in the Metropolis sampling with probability

$$R = \min\left(\frac{P(C' \to C) W_B(\eta') W_F(\eta')}{P(C \to C') W_B(\eta) W_F(\eta)}, 1\right) = \min\left(\frac{W_F(\eta')}{W_F(\eta)}, 1\right) , \tag{A.22}$$

with the adjusted weights

$$W_B(\eta) = \mathrm{e}^{-\frac{\Delta\tau}{2}\sum_{i\tau}\eta_{i\tau}^2/\lambda_i}\,, \tag{A.23}$$

$$W_F(\eta) = \mathrm{Tr}\left[\prod_\tau \mathrm{e}^{-\Delta\tau H_T}\mathrm{e}^{-\sum_{ij} i\Delta\tau U_{ij}\eta_{j\tau}(n_i-1)}\right]\,. \tag{A.24}$$

A local change on a fixed time slice in η-basis corresponds to a non-local spacial change in ϕ-basis. Effectively we carry out one global update in the spacial dimension on a distinct imaginary time slice.

A.1.3 Fermionic Trace

We demonstrate in this section how the fermionic degree of freedom can be “traced out” in the DQMC partition function. We follow the rigorous proofs and detailed discussions in Refs. [22, 194].
We want to prove the relation

$$\mathrm{Tr}\left(\mathrm{e}^{-\sum_{ij} c_i^\dagger A_{ij} c_j}\mathrm{e}^{-\sum_{ij} c_i^\dagger B_{ij} c_j}\right) = \det\left(\boldsymbol{I} + \mathrm{e}^{-A}\mathrm{e}^{-B}\right)\,, \tag{A.25}$$

where A and B are arbitrary matrices and $c_i^{(\dagger)}$ are fermionic ladder operators. We begin by showing that the equation

$$\mathrm{e}^{-\sum_{ij} c_i^\dagger A_{ij} c_j}\mathrm{e}^{-\sum_{ij} c_i^\dagger B_{ij} c_j} = \mathrm{e}^{-\sum_\nu \alpha_\nu c_\nu^\dagger c_\nu} \tag{A.26}$$

holds with $\mathrm{e}^{-\alpha_\nu}$ being the eigenvalues of the matrix $\mathrm{e}^{-A}\mathrm{e}^{-B}$. From this identity the trace-determinant relation in Eq. (A.25) follows immediately:

$$\mathrm{Tr}\,\mathrm{e}^{-\sum_\nu \alpha_\nu c_\nu^\dagger c_\nu} = \prod_\nu \sum_{n_\nu=0,1} \mathrm{e}^{-\alpha_\nu n_\nu} = \prod_\nu (\boldsymbol{I} + \mathrm{e}^{-\alpha_\nu}) = \det\Big(\boldsymbol{I} + \mathrm{e}^{-A}\mathrm{e}^{-B}\Big)\,. \tag{A.27}$$

We are left with proving Eq. (A.26). The idea is to show that both sides of this equation propagate an arbitrary many-particle state in the same way. Consider a single particle state

$$|\Phi\rangle = \sum_j a_j c_j^\dagger \,|0\rangle\,, \tag{A.28}$$

with $a_j \in \mathbb{C}$ and the vacuum state $|0\rangle$. Let $|\mu\rangle$ be a basis in which B is diagonal

$$B = \sum_\mu b_\mu \,|\mu\rangle\,\langle\mu| \tag{A.29}$$

and transform the operators accordingly to

$$c_\mu = \sum_j \langle j|\mu\rangle \, c_j \ , \quad c_\mu^\dagger = \sum_j \langle \mu|j\rangle \, c_j^\dagger \, . \tag{A.30}$$

We can write the exponential of B as

$$\mathrm{e}^{-c_i^\dagger B_{ij} c_j} = \mathrm{e}^{-b_\mu c_\mu^\dagger c_\mu} = \prod_\mu \left[1 + (\mathrm{e}^{-b_\mu} - 1) n_\mu\right] \, . \tag{A.31}$$

Applying this to $|\Phi\rangle$ we find

$$\begin{aligned} \mathrm{e}^{-c_i^\dagger B_{ij} c_j} \, |\Phi\rangle &= \sum_j a_j' c_j^\dagger \, |0\rangle \ \text{, with} \\ a_i' &= \sum_j \left(\mathrm{e}^{-B}\right)_{ij} a_j \, . \end{aligned} \tag{A.32}$$

Similarly we obtain

$$\begin{aligned} \mathrm{e}^{-c_i^\dagger A_{ij} c_j} \mathrm{e}^{-c_i^\dagger B_{ij} c_j} \, |\Phi\rangle &= \sum_j a_j'' c_j^\dagger \, |0\rangle \ \text{, with} \\ a_j'' &= \sum_j (\mathrm{e}^{-A} \mathrm{e}^{-B})_{ij} a_j \, . \end{aligned} \tag{A.33}$$

The above equation is valid in any basis, especially in the basis where the product of the exponentials is diagonal. If we start with an eigenstate of $\mathrm{e}^{-A}\mathrm{e}^{-B}$

$$|\Psi\rangle = c_\nu^\dagger \, |0\rangle \ , \tag{A.34}$$

then

$$\mathrm{e}^{-\sum_{ij} c_i^\dagger A_{ij} c_j} \mathrm{e}^{-\sum_{ij} c_i^\dagger B_{ij} c_j} \, |0\rangle = \left(\mathrm{e}^{-A} \mathrm{e}^{-B}\right)_{\nu\nu} c_\nu^\dagger \, |0\rangle = \mathrm{e}^{-\alpha_\nu} c_\nu^\dagger \, |0\rangle \ , \tag{A.35}$$

which is the same result as the action of the right hand side of Eq. (A.26) on the same state.

Now, we can extend this concept to a many particle state and we will see that the propagation splits into independent propagations of the individual one-particle states. Consider the two-particle state

$$|\Phi\rangle = c_{\mu_1}^\dagger c_{\mu_2}^\dagger \, |0\rangle \tag{A.36}$$

and propagate it with B:

$$\begin{aligned} \mathrm{e}^{-c_i^\dagger B_{ij} c_j} \, |\Phi\rangle &= \prod_\mu \left[1 + (\mathrm{e}^{-b_\mu} - 1) c_\mu^\dagger c_\mu\right] c_{\mu_1}^\dagger c_{\mu_2}^\dagger \, |0\rangle \\ &= \mathrm{e}^{-B_{\mu_1}} \mathrm{e}^{-B_{\mu_2}} c_{\mu_1}^\dagger c_{\mu_2}^\dagger \, |0\rangle \ . \end{aligned} \tag{A.37}$$

This equation is true for both $\mu_1 = \mu_2$ and $\mu_1 \neq \mu_2$. We see that the propagation of a many-particle state is made of the superposition of individual propagations. This argument can be used repeatedly for an arbitrary, fixed number of particles.

A.1.4 Particle-Hole Symmetry in the U-V Model

A profound discussion on the particle-hole symmetry in condensed matter physics can be found in Ref. [195]. According to this reference we define the particle-hole transformation as a charge reversing map

$$K : \mathcal{F}^{pq} \to \mathcal{F}^{qp} \,, \tag{A.38}$$

where $\mathcal{F}^{pq}$ is the combined Fock space of p electron and q hole excitations. We call a Hamiltonian particle-hole symmetric if $KHK^{-1} = H$. Explicitly for the U-V model, we can show that the Hamiltonian, in the form required for the DQMC scheme,

$$H = -t \sum_{\langle i,j \rangle, \sigma} \left(c^{\dagger}_{i\sigma} c_{j\sigma} + \text{h.c.} \right) + \frac{\bar{U}}{2} \sum_{i} (n_i - 1)^2 + \frac{V}{2} \sum_{<ij>} (n_i + n_j - 2)^2 \,, \tag{A.39}$$

with the total local particle number operator $n_i = n_{i\uparrow} + n_{i\downarrow}$ and the renormalized on-site interaction $\bar{U} = U - z_D V$, is invariant under the transformation of the field operators

$$c^{\dagger}_{i\sigma} \to (-1)^i d_{i\sigma} \quad \text{and} \quad c_{i\sigma} \to (-1)^i d^{\dagger}_{i\sigma} \,, \tag{A.40}$$

where $c_{i\sigma}$ ($c^{\dagger}_{i\sigma}$) annihilates (creates) an electron and $d_{i\sigma}$ ($d^{\dagger}_{i\sigma}$) annihilates (creates) a hole on lattice site i with spin σ. The hole operators obey the same anti-commutation relations as the electronic operators. The corresponding particle number operators have the following relation:

$$n_{i\sigma} = c^{\dagger}_{i\sigma} c_{i\sigma} = (-1)^i d_{i\sigma} (-1)^i d^{\dagger}_{i\sigma} = 1 - d^{\dagger}_{i\sigma} d_{i\sigma} = 1 - n^{h}_{i\sigma} \,. \tag{A.41}$$

The electron number $n_{i\sigma} = 0, 1$ is swapped with the hole number $n^{h}_{i\sigma} = 1, 0$.
The operators in the separate terms of the U-V model's Hamiltonian (A.39) transform in the following way:

- The kinetic term:

  $$c^{\dagger}_{i\sigma} c_{j\sigma} = (-1)^{i+j} d_{i\sigma} d^{\dagger}_{j\sigma} = (-1)^{i+j+1} d^{\dagger}_{j\sigma} d_{i\sigma} = d^{\dagger}_{j\sigma} d_{i\sigma} \,. \tag{A.42}$$

  $(-1)^{i+j} = -1$ is always true due to the bipartite nature of the nearest-neighbor hopping, so that $i + j$ is always odd. The second term $c^{\dagger}_{j\sigma} c_{i\sigma}$ transforms into $d^{\dagger}_{i\sigma} d_{j\sigma}$ analogously. Note that next-nearest neighbor hopping terms can induce a fermionic sign problem.

- On-site U-interaction:

$$\begin{aligned}(n_i-1)^2 &= n_i^2-2n_i+1=(n_{i\uparrow}+n_{i\downarrow})^2-2(n_{i\uparrow}+n_{i\downarrow})+1\\ &= 2n_{i\uparrow}n_{i\downarrow}+n_{i\uparrow}^2+n_{i\downarrow}^2-2(n_{i\uparrow}+n_{i\downarrow})+1\\ &= 2n_{i\uparrow}n_{i\downarrow}-(n_{i\uparrow}+n_{i\downarrow})+1\\ &= 2(1-n_{i\uparrow}^h)(1-n_{i\downarrow}^h)-(1-n_{i\uparrow}^h)-(1-n_{i\downarrow}^h)+1\\ &= 2n_{i\uparrow}^h n_{i\downarrow}^h-(n_{i\uparrow}^h+n_{i\downarrow}^h)+1=(n_i^h-1)^2\end{aligned} \tag{A.43}$$

- Inter-site V-interaction:

$$(n_i+n_j-2)^2=(n_i-1)^2+(n_j-1)^2+2(n_i-1)(n_j-1)\,. \tag{A.44}$$

  Both squared terms are of U-interaction type, so that it is sufficient to show the transformation of the remaining part. With $n_i=2-n_i^h$ we get

$$\begin{aligned}2(n_i-1)(n_j-1) &= 2\left[(2-n_i^h)(2-n_j^h)-(2-n_i^h+2-n_j^h)+1\right]\\ &= 2n_i^h n_j^h-2(n_i^h+n_j^h)+2=2(n_i^h-1)(n_j^h-1)\ .\end{aligned} \tag{A.45}$$

For $\mu=0$ the Hamiltonian with squared interaction terms is particle-hole symmetric and half-filling is ensured. Factoring out all terms, we find that half filling corresponds to $\mu=-(\frac{U}{2}+z_D V)$ in the original form (3.1).

A.2 SSE

A.2.1 Detailed Balance for Directed Loop Updates

One global directed-loop update consists of a series of local off-diagonal vertex updates. Following Ref. [79] we show that the loop update fulfills detailed balance by satisfying detailed balance for the individual vertex updates.

We define the probability for n_L head-vertex encounters before recombining with the tail as

$$P_{hv}=P_{\text{init}}P_{\text{insert}}(T_0,|\sigma(l_1)\rangle)\prod_{i=1}^{n_L}P(\Sigma_{b_i,i},T_{i-1}\to T_i,l_i\to l_i')\,, \tag{A.46}$$

where P_{init} is the uniform probability to choose the head position in the operator string (i.e. a point in space-time) and $P_{\text{insert}}(T_0,|\sigma(l_1)\rangle)$ denotes the probability to insert the head with an initial operator T_0 on a leg with the initially proposed state $|\sigma(l_1)\rangle$. The leg index refers to the i-th vertex. Now, we consider the probability for the exact same, but inverse traversed loop. The inverse-head undoes the action of the original head in reverse order after the completion of a whole loop. The inverse-head-tail pair is inserted at the same point carrying the inverse initial operators. The inverse head-vertex encounter probability is given by

$$\bar{P}_{hv} = P_{\text{init}} P_{\text{insert}}(T^{\dagger}_{n_L}, T^{\dagger}_{n_L} \,|\sigma(l'_{n_L})\rangle\rangle) \prod_{i=1}^{n_L} P(\bar{\Sigma}_{b_i,i}, T^{\dagger}_{i} \to T^{\dagger}_{i-1}, l'_i \to l_i)\,. \tag{A.47}$$

Dividing both probabilities yields

$$\frac{P_{hv}}{\bar{P}_{hv}} = \frac{P_{\text{insert}}(T_0, |\sigma(l_1)\rangle\rangle)}{P_{\text{insert}}(T^{\dagger}_{n_L}, T^{\dagger}_{n_L} \,|\sigma(l'_{n_L})\rangle\rangle)} \prod_{i=1}^{n_L} \frac{P(\Sigma_{b_i,i}, T_{i-1} \to T_i, l_i \to l'_i)}{P(\bar{\Sigma}_{b_i,i}, T^{\dagger}_{i} \to T^{\dagger}_{i-1}, l'_i \to l_i)} \tag{A.48}$$

and with the local detailed balance condition (2.93) we obtain

$$\frac{P_{hv}}{\bar{P}_{hv}} = \frac{P_{\text{insert}}(T_0, |\sigma(l_1)\rangle\rangle)}{P_{\text{insert}}(T^{\dagger}_{n_L}, T^{\dagger}_{n_L} \,|\sigma(l'_{n_L})\rangle\rangle)} \prod_{i=1}^{n_L} \frac{W(\Sigma_{b_i,i})}{W(\bar{\Sigma}_{b_i,i})}\,. \tag{A.49}$$

Detailed balance for a loop holds if the insertion probability of the inverse loop is the same as the original one:

$$P_{\text{insert}}(T_0, |\sigma(l_1)\rangle\rangle) = P_{\text{insert}}(T^{\dagger}_{n_L}, T^{\dagger}_{n_L} \,|\sigma(l'_{n_L})\rangle\rangle)\,. \tag{A.50}$$

A.3 n-Component Moment Ratio

To generalize the Binder ratio to an n-component order parameter ($n = 1$ for the Ising model, $n = 2$ for the XY model, $n = 3$ for the Heisenberg model) we integrate a Gaussian distribution of the absolute value of the magnetization $|m|$ over the n-dimensional space to compute the averages $\langle m^4 \rangle$ and $\langle m^2 \rangle$ in the Binder ratio. This introduces n-dependent factors. The consequence is better observed in the more general Binder cumulant U, which takes the values 0 in the disordered phase and 1 in the ordered phase, respectively, in the thermodynamic limit, regardless of the number of components n. Therefore, U is defined by [16]:

$$U = \frac{n+2}{2} \left(1 - \frac{n}{n+2} R \right)\,. \tag{A.51}$$

In the following we calculate the ratio of the one-component and the three-component Binder ratios. In the TDL in the disordered phase the magnetization distribution is centered around 0 for each odd moment, since the integrand is odd over a symmetric interval. We begin by calculating the first two non-vanishing one-component moments:

$$\begin{aligned}\langle m^2\rangle &= \frac{1}{\sqrt{2\pi}}\int_{-\infty}^{\infty}\mathrm{d}m\, m^2 \mathrm{e}^{-m^2/2}\\ &= \frac{1}{\sqrt{2\pi}}\int_{-\infty}^{\infty}\mathrm{d}m\, m\cdot m\,\mathrm{e}^{-m^2/2}\\ &= \frac{1}{\sqrt{2\pi}}\left[\left(m\cdot(-1)\mathrm{e}^{-m^2/2}\right)_{-\infty}^{\infty}+\int_{-\infty}^{\infty}\mathrm{d}m\,\mathrm{e}^{-m^2/2}\right]\\ &= 1\,. \end{aligned} \tag{A.52}$$

For $\langle m^4\rangle$ we employ Wick's theorem 2.2.4 resulting in:

$$\begin{aligned}\langle m^4\rangle &= \wick{\c1 m \c1 m \c2 m \c2 m} + \wick{\c1 m \c2 m \c2 m \c1 m} + \wick{\c1 m \c2 m \c1 m \c2 m}\\ &= 3\langle m^2\rangle = 3\end{aligned} \tag{A.53}$$

As for the three-component moments we obtain:

$$\begin{aligned}\langle \mathbf{m}^2\rangle &= \frac{1}{\sqrt{2\pi}^3}\int\int\int \mathrm{d}m_x\mathrm{d}m_y\mathrm{d}m_z\,\left(m_x^2+m_y^2+m_z^2\right)\mathrm{e}^{-(m_x^2+m_y^2+m_z^2)/2}\\ &= \frac{3}{\sqrt{2\pi}^3}\int\int\int \mathrm{d}m_x\mathrm{d}m_y\mathrm{d}m_z\, m_x^2\,\mathrm{e}^{-m_x^2/2}\mathrm{e}^{-(m_y^2+m_z^2)/2}\\ &= \frac{3}{\sqrt{2\pi}^3}\int \mathrm{d}m_x\, m_x^2\,\mathrm{e}^{-m_x^2/2}\int\int \mathrm{d}m_y\mathrm{d}m_z\,\mathrm{e}^{-(m_y^2+m_z^2)/2}\\ &= \frac{3}{\sqrt{2\pi}}\int \mathrm{d}m_x\, m_x^2\,\mathrm{e}^{-m_x^2/2}\\ &= 3\,. \end{aligned} \tag{A.54}$$

Again for the forth moment we employ Wick's theorem:

$$\begin{aligned}\langle \mathbf{m}^4\rangle &= \langle\left(m_x^2+m_y^2+m_z^2\right)^2\rangle\\ &= \langle m_x^4+m_y^4+m_z^4+m_x^2m_y^2+m_x^2m_z^2+m_y^2m_x^2+m_y^2m_z^2+m_z^2m_x^2+m_z^2m_y^2\rangle\\ &= 3\langle m_x^4\rangle+6\langle m_x^2m_y^2\rangle\\ &= 3\langle m_x^4\rangle+6\langle m_x^2\rangle\langle m_y^2\rangle\\ &= 3\cdot 3+6\cdot 1 = 15\,, \end{aligned} \tag{A.55}$$

where we used

$$\begin{aligned}\langle m_x^2 m_y^2\rangle &= \langle m_x m_x m_y m_y\rangle \\ &= \wick{\c1{m}_x \c1{m}_x \c2{m}_y \c2{m}_y} + \wick{\c1{m}_x \c2{m}_x \c2{m}_y \c1{m}_y} + \wick{\c1{m}_x \c2{m}_x \c1{m}_y \c2{m}_y} \\ &= \langle m_x^2\rangle\langle m_y^2\rangle\,, \end{aligned} \tag{A.56}$$

since $\langle m_i m_j\rangle = 0$ for $i \neq j$. All together we obtain $R(1) = 3$ for the one-component Binder ratio and $R(3) = 5/3$ for the three-component one. As easily calculated both values result in $U = 0$ for the respective n. Finally, the relation between both Binder ratios is

$$R(1) = \frac{9}{5} R(3)\,. \tag{A.57}$$

Publications

[1] A. Sushchyev and S. Wessel. Thermodynamics of the metal-insulator transition in the extended Hubbard model from determinantal quantum Monte Carlo. *Phys. Rev. B*, 106, 10 2022. `doi:10.1103/PhysRevB.106.155121`.

[2] A. Sushchyev and S. Wessel. Anomalous scaling corrections and quantum phase diagram of the Heisenberg antiferromagnet on the spatially anisotropic honeycomb lattice. *Phys. Rev. B*, 108:235146, 12 2023. `doi:10.1103/PhysRevB.108.235146`.

Bibliography

[3] T. Giamarchi. Interactions in quantum fluids. In *Ultracold Gases and Quantum Information: Lecture Notes of the Les Houches Summer School in Singapore: Volume 91, July 2009*. Oxford University Press, 05 2011. `doi:10.1093/acprof:oso/9780199603657.003.0008`.

[4] K. G. Wilson and J. Kogut. The renormalization group and the ϵ expansion. *Physics Reports*, 12(2):75–199, 1974. `doi:https://doi.org/10.1016/0370-1573(74)90023-4`.

[5] M. E. Fisher. The renormalization group in the theory of critical behavior. *Rev. Mod. Phys.*, 46:597–616, Oct 1974. `doi:10.1103/RevModPhys.46.597`.

[6] M. Imada, A. Fujimori, and Y. Tokura. Metal-insulator transitions. *Rev. Mod. Phys.*, 70:1039–1263, Oct 1998. `doi:10.1103/RevModPhys.70.1039`.

[7] J. Hubbard. Electron correlations in narrow energy bands. *Proceedings of the Royal Society of London. Series A. Mathematical and Physical Sciences*, 276:238–257, 11 1963. `doi:10.1098/rspa.1963.0204`.

[8] M. C. Gutzwiller. Effect of correlation on the ferromagnetism of transition metals. *Physical Review*, 134:3–6, 1964. `doi:10.1103/PhysRev.134.A923`.

[9] J. Kanamori. Electron correlation and ferromagnetism of transition metals. *Progress of Theoretical Physics*, 30, 1963. `doi:10.1143/PTP.30.275`.

[10] D. P. Arovas, E. Berg, S. A. Kivelson, and S. Raghu. The Hubbard model. *Annual Review of Condensed Matter Physics*, 13(1):239–274, 2022. `doi:10.1146/annurev-conmatphys-031620-102024`.

[11] S. Bravyi, D. P. DiVincenzo, and D. Loss. Schrieffer–Wolff transformation for quantum many-body systems. *Annals of Physics*, 326(10):2793–2826, 2011. `doi:https://doi.org/10.1016/j.aop.2011.06.004`.

[12] P. Fazekas. *Lecture Notes on Electron Correlation and Magnetism*. EBL-Schweitzer. World Scientific, 1999.

[13] E. Manousakis. The spin-1/2 Heisenberg antiferromagnet on a square lattice and its application to the cuprous oxides. *Rev. Mod. Phys.*, 63:1–62, Jan 1991. `doi:10.1103/RevModPhys.63.1`.

[14] E. Dagotto and T. M. Rice. Surprises on the way from one- to two-dimensional quantum magnets: The ladder materials. *Science*, 271(5249):618–623, 1996. `doi:10.1126/science.271.5249.618`.

[15] J. S. Miller and A. J. Epstein. Molecule-based magnets - an overview. *MRS Bulletin*, 25:21–30, 1 2000. `doi:10.1557/mrs2000.221`.

[16] A. W. Sandvik. Computational studies of quantum spin systems. *AIP Conference Proceedings*, 1297:135–338, 11 2010. `doi:10.1063/1.3518900`.

[17] A. E. Thorarinsdottir and T. D. Harris. Metal–organic framework magnets. *Chemical Reviews*, 120(16):8716–8789, 2020. PMID: 32045215. `doi:10.1021/acs.chemrev.9b00666`.

[18] V. Hinkov, P. Bourges, S. Pailhès, Y. Sidis, A. Ivanov, C. D. Frost, T. G. Perring, C. T. Lin, D. P. Chen, and B. Keimer. Spin dynamics in the pseudogap state of a high-temperature superconductor. *Nature*, 3:780–785, 9 2007. `doi:10.1038/nphys720`.

[19] V. Hinkov, D. Haug, B. Fauqué, P. Bourges, Y. Sidis, A. Ivanov, C. Bernhard, C. T. Lin, and B. Keimer. Electronic liquid crystal state in the high-temperature superconductor $YBa_2Cu_3O_{6.45}$. *Science*, 319(5863):597–600, 2008. `doi:10.1126/science.1152309`.

[20] N. D. Mermin and H. Wagner. Absence of ferromagnetism or antiferromagnetism in one- or two-dimensional isotropic Heisenberg models. *Phys. Rev. Lett.*, 17:1133–1136, 1966. `doi:10.1103/PhysRevLett.17.1133`.

[21] A. Weiße and H. Fehske. *Exact Diagonalization Techniques*, pages 529–544. Springer, Berlin Heidelberg, 2008. `doi:10.1007/978-3-540-74686-7`.

[22] R. Blankenbecler, D. J. Scalapino, and R. L. Sugar. Monte Carlo calculations of coupled boson-fermion systems. i. *Phys. Rev. D*, 24:2278–2286, 1981. `doi:10.1103/PhysRevD.24.2278`.

[23] A. W. Sandvik and J. Kurkijärvi. Quantum Monte Carlo simulation method for spin systems. *Phys. Rev. B*, 43:5950–5961, Mar 1991. `doi:10.1103/PhysRevB.43.5950`.

[24] A. W. Sandvik. A generalization of Handscomb's quantum Monte Carlo scheme-application to the 1D Hubbard model. *Journal of Physics A: Mathematical and General*, 25(13):3667, jul 1992. `doi:10.1088/0305-4470/25/13/017`.

[25] A. W. Sandvik. Stochastic series expansion method with operator-loop update. *Phys. Rev. B*, 59:R14157–R14160, Jun 1999. `doi:10.1103/PhysRevB.59.R14157`.

[26] A. Reingruber, N. Caci, S. Wessel, and J. Richter. Thermodynamics of the spin-1/2 Heisenberg antiferromagnet on the star lattice, 2023. `arXiv:2311.13393`.

[27] A. J. A. James, R. M. Konik, P. Lecheminant, X. Y. Xu, Z. H. Liu, G. Pan, A. Honecker, L. Weber, P. Corboz, F. Mila, and S. Wessel. Quantum Monte Carlo simulations of highly frustrated magnets in a cluster basis: The two-dimensional Shastry-Sutherland model. *Journal of Physics: Conference Series*, 2207:012032, 3 2022. `doi:10.1088/1742-6596/2207/1/012032`.

[28] L. Weber, A. Y. D. Fache, F. Mila, and S. Wessel. Thermal critical points from competing singlet formations in fully frustrated bilayer antiferromagnets. *Phys. Rev. B*, 106:235128, 12 2022. `doi:10.1103/PhysRevB.106.235128`.

[29] L. Weber, N. Caci, and S. Wessel. Cluster quantum Monte Carlo study of two-dimensional weakly coupled frustrated trimer antiferromagnets. *Phys. Rev. B*, 106:035141, 7 2022. `doi:10.1103/PhysRevB.106.035141`.

[30] D. Vollhardt, K. Byczuk, and M. Kollar. *Dynamical Mean-Field Theory*, pages 203–236. Springer Berlin Heidelberg, Berlin, Heidelberg, 2012. `doi:10.1007/978-3-642-21831-6_7`.

[31] T. Pruschke. *Dynamical Mean-Field Approximation and Cluster Methods for Correlated Electron Systems*, pages 473–503. Springer Berlin Heidelberg, Berlin, Heidelberg, 2008. `doi:10.1007/978-3-540-74686-7_16`.

[32] S. R. White. Density matrix formulation for quantum renormalization groups. *Phys. Rev. Lett.*, 69:2863–2866, Nov 1992. `doi:10.1103/PhysRevLett.69.2863`.

[33] I. Peschel and V. Eisler. *The Conceptual Background of Density-Matrix Renormalization*, pages 581–596. Springer Berlin Heidelberg, Berlin, Heidelberg, 2008. `doi:10.1007/978-3-540-74686-7_20`.

[34] J. Jordan, R. Orús, G. Vidal, F. Verstraete, and J. I. Cirac. Classical simulation of infinite-size quantum lattice systems in two spatial dimensions. *Phys. Rev. Lett.*, 101:250602, Dec 2008. `doi:10.1103/PhysRevLett.101.250602`.

[35] D. Reiter. *The Monte Carlo Method, an Introduction*, pages 63–78. Springer, Berlin Heidelberg, 2008. `doi:10.1007/978-3-540-74686-7`.

[36] W. Janke. *Monte Carlo Methods in Classical Statistical Physics*, pages 79–140. Springer, Berlin Heidelberg, 2008. `doi:10.1007/978-3-540-74686-7`.

[37] J. S. Speagle. A conceptual introduction to Markov chain Monte Carlo methods, 2020. `arXiv:1909.12313`.

[38] N. Metropolis, A. W. Rosenbluth, M. N. Rosenbluth, A. H. Teller, and E. Teller. Equation of state calculations by fast computing machines. *The Journal of Chemical Physics*, 21:1087–1092, 1953. `doi:10.1063/1.1699114`.

[39] R. J. Glauber. Time-dependent statistics of the Ising model. *Journal of Mathematical Physics*, 4:294–307, 2 1963. `doi:10.1063/1.1703954`.

[40] U. Wolff. Collective Monte Carlo updating for spin systems. *Phys. Rev. Lett.*, 62:361–364, Jan 1989. `doi:10.1103/PhysRevLett.62.361`.

[41] F. Assaad and H. Evertz. World-line and determinantal quantum Monte Carlo method for spins, phonons and electrons. pages 277–356. Springer, Berlin Heidelberg, 2008. `doi:10.1007/978-3-540-74686-7`.

[42] F. Assaad, M. Bercx, F. Goth, A. Götz, J. Hofmann, E. Huffman, Z. Liu, F. P. Toldin, J. Portela, and J. Schwab. The ALF (Algorithms for Lattice Fermions) project release 2.0. Documentation for the auxiliary-field quantum Monte Carlo code. *SciPost Physics Codebases*, 8 2022. `doi:10.21468/scipostphyscodeb.1`.

[43] P. F. LeBlanc, A. E. Antipov, F. Becca, I. W. Bulik, G. K. L. Chan, C. M. Chung, Y. Deng, M. Ferrero, T. M. Henderson, C. A. Jiménez-Hoyos, E. Kozik, X. W. Liu, A. J. Millis, N. V. Prokof'ev, M. Qin, G. E. Scuseria, H. Shi, B. V. Svistunov, L. F. Tocchio, I. S. Tupitsyn, S. R. White, S. Zhang, B. X. Zheng, Z. Zhu, and E. Gull. Solutions of the two-dimensional Hubbard model: Benchmarks and results from a wide range of numerical algorithms. *Phys. Rev. X*, 5:041041, 12 2015. `doi:10.1103/PhysRevX.5.041041`.

[44] D. J. Scalapino. Numerical studies of the 2D Hubbard model. *Handbook of High-Temperature Superconductivity*, pages 495–526, 3 2007. `doi:10.1007/978-0-387-68734-6_13`.

[45] F. F. Assaad, M. Bercx, and M. Hohenadler. Topological invariant and quantum spin models from magnetic π fluxes in correlated topological insulators. *Phys. Rev. X*, 3:011015, 2 2013. `doi:10.1103/PhysRevX.3.011015`.

[46] J. S. Hofmann, F. F. Assaad, R. Queiroz, and E. Khalaf. Search for correlation-induced adiabatic paths between distinct topological insulators. *Phys. Rev. Res.*, 2:023390, Jun 2020. `doi:10.1103/PhysRevResearch.2.023390`.

[47] D. Zheng, G. M. Zhang, and C. Wu. Particle-hole symmetry and interaction effects in the Kane-Mele-Hubbard model. *Phys. Rev. B*, 84:205121, 11 2011. `doi:10.1103/PhysRevB.84.205121`.

[48] M. Hohenadler, T. C. Lang, and F. F. Assaad. Correlation effects in quantum spin-Hall insulators: A quantum Monte Carlo study. *Phys. Rev. Lett.*, 106:100403, 3 2011. `doi:10.1103/PhysRevLett.106.100403`.

[49] V. Peri, Z. D. Song, B. A. Bernevig, and S. D. Huber. Fragile topology and flat-band superconductivity in the strong-coupling regime. *Phys. Rev. Lett.*, 126, 2021. `doi:10.1103/PhysRevLett.126.027002`.

[50] M. Hohenadler, F. P. Toldin, I. F. Herbut, and F. F. Assaad. Phase diagram of the Kane-Mele-Coulomb model. *Phys. Rev. B*, 90, 8 2014. `doi:10.1103/PhysRevB.90.085146`.

[51] H. K. Tang, J. N. Leaw, J. N. Rodrigues, I. F. Herbut, P. Sengupta, F. F. Assaad, and S. Adam. The role of electron-electron interactions in two-dimensional Dirac fermions. *Science*, 361:570–574, 8 2018. `doi:10.1126/science.AAO2934`.

[52] H. K. Tang, E. Laksono, J. N. Rodrigues, P. Sengupta, F. F. Assaad, and S. Adam. Interaction-driven metal-insulator transition in strained graphene. *Phys. Rev. Lett.*, 115:186602, 10 2015. `doi:10.1103/PhysRevLett.115.186602`.

[53] M. Raczkowski and F. F. Assaad. Interplay between the edge-state magnetism and long-range Coulomb interaction in zigzag graphene nanoribbons: Quantum Monte Carlo study. *Phys. Rev. B*, 96:115155, 9 2017. `doi:10.1103/PhysRevB.96.115155`.

[54] J. N. Leaw, H. K. Tang, P. Sengupta, F. F. Assaad, I. F. Herbut, and S. Adam. Electronic ground state in bilayer graphene with realistic Coulomb interactions. *Phys. Rev. B*, 100:125116, 9 2019. `doi:10.1103/PhysRevB.100.125116`.

[55] G. Pan, W. Wang, A. Davis, Y. Wang, and Z. Y. Meng. Yukawa-SYK model and self-tuned quantum criticality. *Phys. Rev. Res.*, 3:013250, 3 2021. `doi:10.1103/PhysRevRes.3.013250`.

[56] M. Rozenberg. Dynamical mean-field theory and the Mott transition. *Many-Body Methods for Real Materials*, 9, 2019.

[57] Y. Schattner, S. Lederer, S. A. Kivelson, and E. Berg. Ising nematic quantum critical point in a metal: A Monte Carlo study. *Phys. Rev. X*, 6:031028, 8 2016. `doi:10.1103/PhysRevX.6.031028`.

[58] O. Grossman, J. S. Hofmann, T. Holder, and E. Berg. Specific heat of a quantum critical metal. *Phys. Rev. Lett.*, 127:017601, 7 2021. `doi:10.1103/PhysRevLett.127.017601`.

[59] X. Y. Xu, K. Sun, Y. Schattner, E. Berg, and Z. Y. Meng. Non-fermi liquid at (2+1)D ferromagnetic quantum critical point. *Phys. Rev. X*, 7:031058, 9 2017. `doi:10.1103/PhysRevX.7.031058`.

[60] Z. H. Liu, G. Pan, X. Y. Xu, K. Sun, and Z. Y. Meng. Itinerant quantum critical point with fermion pockets and hotspots. *Proceedings of the National Academy of Sciences*, 116(34):16760–16767, 2019. `doi:10.1073/pnas.1901751116`.

[61] R. Mondaini, S. Tarat, and R. T. Scalettar. Quantum critical points and the sign-problem. *Science*, 375(6579):418–424, 2022. `doi:10.1126/science.abg9299`.

[62] K. S. D. Beach. Identifying the maximum entropy method as a special limit of stochastic analytic continuation, 2004. `arXiv:cond-mat/0403055`.

[63] J. Dongarra, M. Gates, A. Haidar, J. Kurzak, P. Luszczek, S. Tomov, and I. Yamazaki. The singular value decomposition: Anatomy of optimizing an algorithm for extreme scale. *SIAM Review*, 60:808–865, 11 2018. `doi:10.1137/17M1117732`.

[64] Z. Bai, C. Lee, R. C. Li, and S. Xu. Stable solutions of linear systems involving long chain of matrix multiplications. *Linear Algebra and Its Applications*, 435:659–673, 2011. `doi:10.1016/j.laa.2010.06.023`.

[65] M. Ulybyshev and F. Assaad. Mitigating spikes in fermion Monte Carlo methods by reshuffling measurements. *Phys. Rev. E*, 106, 8 2022. `doi:10.1103/PhysRevE.106.025318`.

[66] M. Troyer and U. J. Wiese. Computational complexity and fundamental limitations to fermionic quantum Monte Carlo simulations. *Phys. Rev. Lett.*, 94, 5 2005. `doi:10.1103/PhysRevLett.94.170201`.

[67] Z.-X. Li and H. Yao. Sign-problem-free fermionic quantum Monte Carlo: Developments and applications. 5 2018. `doi:10.1146/annurev-conmatphys-033117-054307`.

[68] P. Henelius, P. Fröbrich, P. J. Kuntz, C. Timm, and P. J. Jensen. Quantum Monte Carlo simulation of thin magnetic films. *Phys. Rev. B*, 66:094407, 9 2002. `doi:10.1103/PhysRevB.66.094407`.

[69] R. G. Melko. Simulations of quantum XXZ models on two-dimensional frustrated lattices. *Journal of Physics: Condensed Matter*, 19:145203, 3 2007. `doi:10.1088/0953-8984/19/14/145203`.

[70] A. W. Sandvik. Stochastic series expansion method for quantum Ising models with arbitrary interactions. *Phys. Rev. E*, 68:056701, 11 2003. `doi:10.1103/PhysRevE.68.056701`.

[71] S. Wessel, F. Alet, M. Troyer, and G. G. Batrouni. Quantum Monte Carlo simulations of confined bosonic atoms in optical lattices. *Phys. Rev. A*, 70:053615, 11 2004. `doi:10.1103/PhysRevA.70.053615`.

[72] S. Wessel, F. Alet, S. Trebst, D. Leumann, M. Troyer, and G. George Batrouni. Bosons in optical lattices – from the Mott transition to the Tonks–Girardeau gas. *Journal of the Physical Society of Japan*, 74(Suppl):10–15, 2005. `doi:10.1143/JPSJS.74S.10`.

[73] P. Pippan, H. G. Evertz, and M. Hohenadler. Excitation spectra of strongly correlated lattice bosons and polaritons. *Phys. Rev. A*, 80:033612, Sep 2009. `doi:10.1103/PhysRevA.80.033612`.

[74] K. Harada, N. Kawashima, and M. Troyer. Néel and spin-Peierls ground states of two-dimensional quantum antiferromagnets. *Phys. Rev. Lett.*, 90:4, 3 2003. `doi:10.1103/PhysRevLett.90.117203`.

[75] N. Kawashima and Y. Tanabe. Ground states of the SU(N) Heisenberg model. *Phys. Rev. Lett.*, 98:057202, Jan 2007. `doi:10.1103/PhysRevLett.98.057202`.

[76] R. K. Kaul and A. W. Sandvik. Lattice model for the SU(N) Néel to valence-bond solid quantum phase transition at large N. *Phys. Rev. Lett*, 108:137201, 3. `doi:10.1103/PhysRevLett.108.137201`.

[77] R. K. Kaul, R. G. Melko, and A. W. Sandvik. Bridging lattice-scale physics and continuum field theory with quantum Monte Carlo simulations. *Annual Review of Condensed Matter Physics*, 4(1):179–215, 2013. `doi:10.1146/annurev-conmatphys-030212-184215`.

[78] O. F. Syljuasen and A. W. Sandvik. Quantum Monte Carlo with directed loops. *Phys. Rev. E*, 66:046701, 10 2002. `doi:10.1103/PhysRevE.66.046701`.

[79] F. Alet, S. Wessel, and M. Troyer. Generalized directed loop method for quantum Monte Carlo simulations. *Phys. Rev. E*, 71:036706, Mar 2005. `doi:10.1103/PhysRevE.71.036706`.

[80] T. Nakamura. Vanishing of the negative sign-problem of quantum Monte Carlo simulations in one-dimensional frustrated spin systems. *Phys. Rev. B*, 57:R3197, 2 1998. `doi:10.1103/PhysRevB.57.R3197`.

[81] F. Alet, K. Damle, and S. Pujari. Sign-problem-free Monte Carlo simulation of certain frustrated quantum magnets. *Phys. Rev. Lett.*, 117:197203, 11 2016. `doi:10.1103/PhysRevLett.117.197203`.

[82] A. Honecker, S. Wessel, R. Kerkdyk, T. Pruschke, F. Mila, and B. Normand. Thermodynamic properties of highly frustrated quantum spin ladders: Influence of many-particle bound states. *Phys. Rev. B*, 93:054408, 2 2016. `doi:10.1103/PhysRevB.93.054408`.

[83] S. Wessel, B. Normand, F. Mila, and A. Honecker. Efficient quantum Monte Carlo simulations of highly frustrated magnets: The frustrated spin-1/2 ladder. *SciPost Phys.*, 3:005, 2017. `doi:10.21468/SciPostPhys.3.1.005`.

[84] K. K. Ng and M. F. Yang. Field-induced quantum phases in a frustrated spin-dimer model: A sign-problem-free quantum Monte Carlo study. *Phys. Rev. B*, 95:064431, 2 2017. `doi:10.1103/PhysRevB.95.064431`.

[85] J. Stapmanns, P. Corboz, F. Mila, A. Honecker, B. Normand, and S. Wessel. Thermal critical points and quantum critical end point in the frustrated bilayer Heisenberg antiferromagnet. *Phys. Rev. Lett.*, 121:127201, 9 2018. `doi:10.1103/PhysRevLett.121.127201`.

[86] S. Wessel, I. Niesen, J. Stapmanns, B. Normand, F. Mila, P. Corboz, and A. Honecker. Thermodynamic properties of the Shastry-Sutherland model from quantum Monte Carlo simulations. *Phys. Rev. B*, 98:174432, 11 2018. `doi:10.1103/PhysRevB.98.174432`.

[87] O. F. Syljuasen. Directed loop updates for quantum lattice models. *Phys. Rev. E*, 67:046701, 4 2003. `doi:10.1103/PhysRevE.67.046701`.

[88] A. Dorneich and M. Troyer. Accessing the dynamics of large many-particle systems using the stochastic series expansion. *Phys. Rev. E*, 64:066701, 11 2001. `doi:10.1103/PhysRevE.64.066701`.

[89] B. Efron. Bootstrap methods: Another look at the Jackknife. *The Annals of Statistics*, 7(1):1–26, 1979.

[90] E. Khatami and M. Rigol. Thermodynamics of strongly interacting fermions in two-dimensional optical lattices. *Phys. Rev. A*, 84, 11 2011. `doi:10.1103/PhysRevA.84.053611`.

[91] J. P. Leblanc and E. Gull. Equation of state of the fermionic two-dimensional Hubbard model. *Phys. Rev. B*, 88, 10 2013. `doi:10.1103/PhysRevB.88.155108`.

[92] K. Seki, T. Shirakawa, and S. Yunoki. Variational cluster approach to thermodynamic properties of interacting fermions at finite temperatures: A case study of the two-dimensional single-band Hubbard model at half filling. *Phys. Rev. B*, 98, 11 2018. `doi:10.1103/PhysRevB.98.205114`.

[93] E. Kozik, E. Burovski, V. W. Scarola, and M. Troyer. Néel temperature and thermodynamics of the half-filled three-dimensional Hubbard model by diagrammatic determinant Monte Carlo. *Phys. Rev. B*, 87, 5 2013. `doi:10.1103/PhysRevB.87.205102`.

[94] C. Walsh, P. Sémon, D. Poulin, G. Sordi, and A. M. Tremblay. Thermodynamic and information-theoretic description of the Mott transition in the two-dimensional Hubbard model. *Phys. Rev. B*, 99, 2 2019. `doi:10.1103/PhysRevB.99.075122`.

[95] T. Esslinger. Fermi-Hubbard physics with atoms in an optical lattice. *Annual Review of Condensed Matter Physics*, 1:129–152, 7 2010. `doi:10.1146/annurev-conmatphys-070909-104059`.

[96] M. Greiner, O. Mandel, T. Esslinger, T. W. Haensch, and I. Bloch. Quantum phase transition from a superfluid to a Mott insulator in a gas of ultracold atoms. *ChemInform*, 33, 2010. `doi:10.1002/chin.200214016`.

[97] R. Jördens, N. Strohmaier, K. Günter, H. Moritz, and T. Esslinger. A Mott insulator of fermionic atoms in an optical lattice. *Nature*, 455:204–207, 2008. `doi:10.1038/nature07244`.

[98] E. Cocchi, L. A. Miller, J. H. Drewes, M. Koschorreck, D. Pertot, F. Brennecke, and M. Köhl. Equation of state of the two-dimensional Hubbard model. *Phys. Rev. Lett.*, 116, 4 2016. `doi:10.1103/PhysRevLett.116.175301`.

[99] E. Cocchi, L. A. Miller, J. H. Drewes, C. F. Chan, D. Pertot, F. Brennecke, and M. Köhl. Measuring entropy and short-range correlations in the two-dimensional Hubbard model. *Phys. Rev. X*, 7, 8 2017. `doi:10.1103/PhysRevX.7.031025`.

[100] H.-J. Shao, Y.-X. Wang, D.-Z. Zhu, Y.-S. Zhu, H.-N. Sun, S.-Y. Chen, C. Zhang, Z.-J. Fan, Y. Deng, X.-C. Yao, Y.-A. Chen, and J.-W. Pan. Observation of the antiferromagnetic phase transition in the fermionic Hubbard model, 2024. `arXiv:2402.14605`.

[101] T. Ayral, S. Biermann, P. Werner, and L. Boehnke. Influence of Fock exchange in combined many-body perturbation and dynamical mean field theory. *Phys. Rev. B*, 95, 6 2017. `doi:10.1103/PhysRevB.95.245130`.

[102] Y. I. T. Veld, M. Schüler, T. O. Wehling, M. I. Katsnelson, and E. G. V. Loon. Bandwidth renormalization due to the intersite Coulomb interaction. *Journal of Physics Condensed Matter*, 31, 8 2019. `doi:10.1088/1361-648X/ab36fe`.

[103] R. A. Bari. Effects of short-range interactions on electron-charge ordering and lattice distortions in the localized state. *Phys. Rev. B*, 3:2662–2670, Apr 1971. `doi:10.1103/PhysRevB.3.2662`.

[104] Y. Zhang and J. Callaway. Extended Hubbard model in two dimensions. *Phys. Rev. B*, 39:9397–9404, 1989. `doi:10.1103/PhysRevB.39.9397`.

[105] H. Terletska, T. Chen, and E. Gull. Charge ordering and correlation effects in the extended Hubbard model. *Phys. Rev. B*, 95, 3 2017. `doi:10.1103/PhysRevB.95.115149`.

[106] H. Terletska, T. Chen, J. Paki, and E. Gull. Charge ordering and nonlocal correlations in the doped extended Hubbard model. *Phys. Rev. B*, 97, 3 2018. `doi:10.1103/PhysRevB.97.115117`.

[107] J. Paki, H. Terletska, S. Iskakov, and E. Gull. Charge order and antiferromagnetism in the extended Hubbard model. *Phys. Rev. B*, 99, 6 2019. `doi:10.1103/PhysRevB.99.245146`.

[108] M. Schüler, E. G. V. Loon, M. I. Katsnelson, and T. O. Wehling. First-order metal-insulator transitions in the extended Hubbard model due to self-consistent screening of the effective interaction. *Phys. Rev. B*, 97, 4 2018. `doi:10.1103/PhysRevB.97.165135`.

[109] M. Schüler, E. G. van Loon, M. I. Katsnelson, and T. O. Wehling. Thermodynamics of the metal-insulator transition in the extended Hubbard model. *SciPost Physics*, 6, 6 2019. `doi:10.21468/SciPostPhys.6.6.067`.

[110] M. Golor and S. Wessel. Nonlocal density interactions in auxiliary-field quantum Monte Carlo simulations: Application to the square lattice bilayer and honeycomb lattice. *Phys. Rev. B*, 92, 11 2015. `doi:10.1103/PhysRevB.92.195154`.

[111] L. Fratino, P. Sémon, M. Charlebois, G. Sordi, and A. M. Tremblay. Signatures of the Mott transition in the antiferromagnetic state of the two-dimensional Hubbard model. *Phys. Rev. B*, 95, 6 2017. `doi:10.1103/PhysRevB.95.235109`.

[112] M. Laubach, R. Thomale, C. Platt, W. Hanke, and G. Li. Phase diagram of the Hubbard model on the anisotropic triangular lattice. *Phys. Rev. B*, 91, 6 2015. `doi:10.1103/PhysRevB.91.245125`.

[113] A. Georges and W. Krauth. Numerical solution of the d = ∞ Hubbard model: Evidence for a Mott transition. *Phys. Rev. Lett.*, 69, 1992. `doi:10.1103/PhysRevLett.69.1240`.

[114] F. Werner, O. Parcollet, A. Georges, and S. R. Hassan. Interaction-induced adiabatic cooling and antiferromagnetism of cold fermions in optical lattices. *Phys. Rev. Lett.*, 95, 7 2005. `doi:10.1103/PhysRevLett.95.056401`.

[115] M. Yao, D. Wang, and Q.-H. Wang. Determinant quantum Monte Carlo for the half-filled Hubbard model with nonlocal density-density interactions. *Phys. Rev. B*, 106:195121, Nov 2022. `doi:10.1103/PhysRevB.106.195121`.

[116] S. R. White. Minimally entangled typical quantum states at finite temperature. *Phys. Rev. Lett.*, 102:190601, May 2009. `doi:10.1103/PhysRevLett.102.190601`.

[117] E. M. Stoudenmire and S. R. White. Minimally entangled typical thermal state algorithms. *New Journal of Physics*, 12(5):055026, may 2010. `doi:10.1088/1367-2630/12/5/055026`.

[118] A. Sushchyev and S. Wessel. Thermodynamics of the metal-insulator transition in the extended Hubbard model from determinantal quantum Monte Carlo, September 2022. `doi:10.5281/zenodo.7116398`.

[119] A. Kerelsky, C. Rubio-Verdú, L. Xian, D. M. Kennes, D. Halbertal, N. Finney, L. Song, S. Turkel, L. Wang, K. Watanabe, T. Taniguchi, J. Hone, C. Dean, D. N. Basov, A. Rubio, and A. N. Pasupathy. Moiréless correlations in ABCA graphene. *Proceedings of the National Academy of Sciences*, 118, 1 2021. `doi:10.1073/pnas.2017366118`.

[120] T. C. Lang, Z. Y. Meng, M. M. Scherer, S. Uebelacker, F. F. Assaad, A. Muramatsu, C. Honerkamp, and S. Wessel. Antiferromagnetism in the Hubbard model on the Bernal-stacked honeycomb bilayer. *Phys. Rev. Lett.*, 109:126402, 9 2012. `doi:10.1103/PhysRevLett.109.126402`.

[121] A. M. Seiler, F. R. Geisenhof, F. Winterer, K. Watanabe, T. Taniguchi, T. Xu, F. Zhang, and R. T. Weitz. Quantum cascade of correlated phases in trigonally warped bilayer graphene. *Nature*, 608:298–302, 8 2022. `doi:10.1038/s41586-022-04937-1`.

[122] H. Zhou, T. Xie, T. Taniguchi, K. Watanabe, and A. F. Young. Superconductivity in rhombohedral trilayer graphene. *Nature*, 598:434–438, 9 2021. `doi:10.1038/s41586-021-03926-0`.

[123] K. G. Wirth, J. B. Hauck, A. Rothstein, H. Kyoseva, D. Siebenkotten, L. Conrads, L. Klebl, A. Fischer, B. Beschoten, C. Stampfer, D. M. Kennes, L. Waldecker, and T. Taubner. Experimental observation of ABCB stacked tetralayer graphene. *ACS Nano*, 16:16617–16623, 10 2022. `doi:10.1021/acsnano.2C06053`.

[124] A. Fischer, L. Klebl, J. B. Hauck, A. Rothstein, L. Waldecker, B. Beschoten, T. O. Wehling, and D. M. Kennes. Spin and charge fluctuation induced pairing in ABCB tetralayer graphene. *Phys. Rev. Res.*, 6:L012003, 5 2023. `doi:10.1103/PhysRevResearch.6.L012003`.

[125] Y. Zhang, R. Polski, A. Thomson, Étienne Lantagne-Hurtubise, C. Lewandowski, H. Zhou, K. Watanabe, T. Taniguchi, J. Alicea, and S. Nadj-Perge. Enhanced superconductivity in spin–orbit proximitized bilayer graphene. *Nature*, 613:268–273, 1 2023. `doi:10.1038/s41586-022-05446-x`.

[126] Y. Cao, V. Fatemi, A. Demir, S. Fang, S. L. Tomarken, J. Y. Luo, J. D. Sanchez-Yamagishi, K. Watanabe, T. Taniguchi, E. Kaxiras, R. C. Ashoori, and P. Jarillo-Herrero. Correlated insulator behaviour at half-filling in magic-angle graphene superlattices. *Nature*, 556:80–84, 3 2018. `doi:10.1038/nature26154`.

[127] M. Yankowitz, S. Chen, H. Polshyn, Y. Zhang, K. Watanabe, T. Taniguchi, D. Graf, A. F. Young, and C. R. Dean. Tuning superconductivity in twisted bilayer graphene. *Science*, 363:1059–1064, 3 2019. `doi:10.1126/science.aav1910`.

[128] Y. Cao, D. Rodan-Legrain, O. Rubies-Bigorda, J. M. Park, K. Watanabe, T. Taniguchi, and P. Jarillo-Herrero. Tunable correlated states and spin-polarized phases in twisted bilayer–bilayer graphene. *Nature*, 583:215–220, 5 2020. `doi:10.1038/s41586-020-2260-6`.

[129] C. Shen, Y. Chu, Q. S. Wu, N. Li, S. Wang, Y. Zhao, J. Tang, J. Liu, J. Tian, K. Watanabe, T. Taniguchi, R. Yang, Z. Y. Meng, D. Shi, O. V. Yazyev, and G. Zhang. Correlated states in twisted double bilayer graphene. *Nature*, 16:520–525, 3 2020. `doi:10.1038/s41567-020-0825-9`.

[130] X. Liu, Z. Hao, E. Khalaf, J. Y. Lee, Y. Ronen, H. Yoo, D. H. Najafabadi, K. Watanabe, T. Taniguchi, A. Vishwanath, and P. Kim. Tunable spin-polarized correlated states in twisted double bilayer graphene. *Nature*, 583:221–225, 7 2020. `doi:10.1038/s41586-020-2458-7`.

[131] R. Bistritzer and A. H. MacDonald. Moiré bands in twisted double-layer graphene. *Proceedings of the National Academy of Sciences*, 108:12233–12237, 7 2011. `doi:10.1073/pnas.1108174108`.

[132] L. Wang, E. M. Shih, A. Ghiotto, L. Xian, D. A. Rhodes, C. Tan, M. Claassen, D. M. Kennes, Y. Bai, B. Kim, K. Watanabe, T. Taniguchi, X. Zhu, J. Hone, A. Rubio, A. N. Pasupathy, and C. R. Dean. Correlated electronic phases in twisted bilayer transition metal dichalcogenides. *Nature*, 19:861–866, 6 2020. `doi:10.1038/s41563-020-0708-6`.

[133] F. Zhang, B. Sahu, H. Min, and A. H. MacDonald. Band structure of ABC-stacked graphene trilayers. *Phys. Rev. B*, 82:035409, Jul 2010. `doi:10.1103/PhysRevB.82.035409`.

[134] H. Min and A. H. MacDonald. Electronic structure of multilayer graphene. *Progress of Theoretical Physics Supplement*, 176:227–252, 06 2008. `doi:10.1143/ptps.176.227`.

[135] B. Grünbaum and G. C. Shephard. Tilings by regular polygons. *Math. Mag.*, 50(5):227–247, 1977. `doi:10.1080/0025570X.1977.11976655`.

[136] J. Richter, J. Schulenburg, and A. Honecker. Quantum magnetism in two dimensions: From semi-classical Néel order to magnetic disorder. In *Quantum Magnetism*, pages 85–153. Springer Berlin Heidelberg, 2004. `doi:10.1007/bfb0119592`.

[137] U. Löw. Properties of the two-dimensional spin-1/2 Heisenberg model on a honeycomb lattice with interlayer coupling. *Condensed Matter Physics*, 12:497–506, 01 2009. `doi:10.5488/cmp.12.3.497`.

[138] F. J. Jiang and U. Gerber. Subtlety of determining the critical exponent *nu* of the spin-1/2 Heisenberg model with a spatially staggered anisotropy on the honeycomb lattice. *Journal of Statistical Mechanics: Theory and Experiment*, 2009, 2009. `doi:10.1088/1742-5468/2009/09/P09016`.

[139] M. Matsumoto, C. Yasuda, S. Todo, and H. Takayama. Ground-state phase diagram of quantum Heisenberg antiferromagnets on the anisotropic dimerized square lattice. *Phys. Rev. B*, 65:014407, Nov 2001. `doi:10.1103/PhysRevB.65.014407`.

[140] L. Wang, K. S. Beach, and A. W. Sandvik. High-precision finite-size scaling analysis of the quantum-critical point of s=1/2 Heisenberg antiferromagnetic bilayers. *Phys. Rev. B*, 73, 2006. `doi:10.1103/PhysRevB.73.014431`.

[141] S. Wenzel, L. Bogacz, and W. Janke. Evidence for an unconventional universality class from a two-dimensional dimerized quantum Heisenberg model. *Phys. Rev. Lett.*, 101, 9 2008. `doi:10.1103/PhysRevLett.101.127202`.

[142] F. J. Jiang. Monte Carlo simulations of an unconventional phase transition for a two-dimensional dimerized quantum Heisenberg model. *Phys. Rev. B*, 85, 1 2012. `doi:10.1103/PhysRevB.85.014414`.

[143] L. Fritz, R. L. Doretto, S. Wessel, S. Wenzel, S. Burdin, and M. Vojta. Cubic interactions and quantum criticality in dimerized antiferromagnets. *Phys. Rev. B*, 83, 5 2011. `doi:10.1103/PhysRevB.83.174416`.

[144] S. Yasuda and S. Todo. Monte Carlo simulation with aspect-ratio optimization: Anomalous anisotropic scaling in dimerized antiferromagnets. *Phys. Rev. E*, 88, 12 2013. `doi:10.1103/PhysRevE.88.061301`.

[145] N. Ma, P. Weinberg, H. Shao, W. Guo, D. X. Yao, and A. W. Sandvik. Anomalous quantum-critical scaling corrections in two-dimensional antiferromagnets. *Phys. Rev. Lett.*, 121, 9 2018. `doi:10.1103/PhysRevLett.121.117202`.

[146] M. Troyer, M. Imada, and K. Ueda. Critical exponents of the quantum phase transition in a planar antiferromagnet. *Journal of the Physical Society of Japan*, 66(10):2957–2960, 1997. `doi:10.1143/JPSJ.66.2957`.

[147] S. Wenzel and W. Janke. Comprehensive quantum Monte Carlo study of the quantum critical points in planar dimerized/quadrumerized Heisenberg models. *Phys. Rev. B*, 79:014410, Jan 2009. `doi:10.1103/PhysRevB.79.014410`.

[148] A. F. Albuquerque, M. Troyer, and J. Oitmaa. Quantum phase transition in a Heisenberg antiferromagnet on a square lattice with strong plaquette interactions. *Phys. Rev. B*, 78:132402, Oct 2008. `doi:10.1103/PhysRevB.78.132402`.

[149] J. Zinn-Justin. *Quantum Field Theory and Critical Phenomena*. International Series of Monographs on Physics. Oxford University Press, 2021.

[150] A. V. Chubukov, S. Sachdev, and J. Ye. Theory of two-dimensional quantum Heisenberg antiferromagnets with a nearly critical ground state. *Phys. Rev. B*, 49:11919–11961, May 1994. `doi:10.1103/PhysRevB.49.11919`.

[151] M. E. Fisher. Renormalization group theory: Its basis and formulation in statistical physics. *Rev. Mod. Phys.*, 70:653–681, Apr 1998. `doi:10.1103/RevModPhys.70.653`.

[152] K. Binder. Finite size scaling analysis of Ising model block distribution functions. *Zeitschrift für Physik B Condensed Matter*, 43(2):119–140, 1981. `doi:10.1007/BF01293604`.

[153] C. Holm and W. Janke. Critical exponents of the classical three-dimensional Heisenberg model: A single-cluster Monte Carlo study. *Phys. Rev. B*, 48:936–950, Jul 1993. `doi:10.1103/PhysRevB.48.936`.

[154] T. Giamarchi. *Quantum Physics in One Dimension.* International Series of Monographs on Physics. Clarendon Press, 2004.

[155] R. Guida and J. Zinn-Justin. Critical exponents of the N-vector model. *Journal of Physics A: Mathematical and General*, 31(40):8103, oct 1998. `doi:10.1088/0305-4470/31/40/006`.

[156] M. Hasenbusch. Eliminating leading corrections to scaling in the three-dimensional $O(N)$-symmetric Φ^4 model: $N = 3$ and 4. *Journal of Physics A: Mathematical and General*, 34(40):8221, sep 2001. `doi:10.1088/0305-4470/34/40/302`.

[157] M. Campostrini, M. Hasenbusch, A. Pelissetto, P. Rossi, and E. Vicari. Critical exponents and equation of state of the three-dimensional Heisenberg universality class. *Phys. Rev. B*, 65:1–21, 2002. `doi:10.1103/PhysRevB.65.144520`.

[158] X. S. Chen and V. Dohm. Nonuniversal finite-size scaling in anisotropic systems. *Phys. Rev. E*, 70:7, 2004. `doi:10.1103/PhysRevE.70.056136`.

[159] W. Selke and L. N. Shchur. Critical Binder cumulant in two-dimensional anisotropic Ising models. *Journal of Physics A: Mathematical and General*, 38, 11 2005. `doi:10.1088/0305-4470/38/44/L03`.

[160] G. Kamieniarz and H. W. J. Blote. Universal ratio of magnetization moments in two-dimensional Ising models. *Journal of Physics A: Mathematical and General*, 26(2):201, jan 1993. `doi:10.1088/0305-4470/26/2/009`.

[161] W. Selke. The critical Binder cumulant for isotropic Ising models on square and triangular lattices. *Journal of Statistical Mechanics: Theory and Experiment*, 4 2007. `doi:10.1088/1742-5468/2007/04/P04008`.

[162] V. Dohm. Multiparameter universality and directional nonuniversality of exact anisotropic critical correlation functions of the two-dimensional Ising universality class. *Phys. Rev. E*, 100, 11 2019. `doi:10.1103/PhysRevE.100.050101`.

[163] J. Stephenson. Ising-model spin correlations on the triangular lattice. *Journal of Mathematical Physics*, 5(8):1009–1024, 12 2004. `doi:10.1063/1.1704202`.

[164] V. Dohm and S. Wessel. Exact critical Casimir amplitude of anisotropic systems from conformal field theory and self-similarity of finite-size scaling functions in $d \geq 2$

dimensions. *Phys. Rev. Lett.*, 126:060601, Feb 2021. `doi:10.1103/PhysRevLett.126.060601`.

[165] V. Dohm, S. Wessel, B. Kalthoff, and W. Selke. Multiparameter universality and conformal field theory for anisotropic confined systems: test by Monte Carlo simulations. *Journal of Physics A: Mathematical and Theoretical*, 54(23):23LT01, may 2021. `doi:10.1088/1751-8121/abf7f8`.

[166] R. Houtappel. Order-disorder in hexagonal lattices. *Physica*, 16(5):425–455, 1950. `doi:https://doi.org/10.1016/0031-8914(50)90130-3`.

[167] A. E. Ferdinand and M. E. Fisher. Bounded and inhomogeneous Ising models. i. Specific-heat anomaly of a finite lattice. *Phys. Rev.*, 185:832–846, Sep 1969. `doi:10.1103/PhysRev.185.832`.

[168] F. Haldane. Continuum dynamics of the 1-D Heisenberg antiferromagnet: Identification with the O(3) nonlinear sigma model. *Physics Letters A*, 93(9):464–468, 1983. `doi:https://doi.org/10.1016/0375-9601(83)90631-X`.

[169] F. D. M. Haldane. Nonlinear field theory of large-spin Heisenberg antiferromagnets: Semiclassically quantized solitons of the one-dimensional easy-axis Néel state. *Phys. Rev. Lett.*, 50:1153–1156, Apr 1983. `doi:10.1103/PhysRevLett.50.1153`.

[170] A. Auerbach. Interacting electrons and quantum magnetism. 1994. `doi:10.1007/978-1-4612-0869-3`.

[171] H.-J. Mikeska and A. K. Kolezhuk. *One-dimensional magnetism*, pages 1–83. Springer Berlin Heidelberg, Berlin, Heidelberg, 2004. `doi:10.1007/BFb0119591`.

[172] I. Affleck, T. Kennedy, E. H. Lieb, and H. Tasaki. Rigorous results on valence-bond ground states in antiferromagnets. *Phys. Rev. Lett.*, 59:799–802, Aug 1987. `doi:10.1103/PhysRevLett.59.799`.

[173] J. D. Reger and A. P. Young. Monte Carlo simulations of the spin-1/2 Heisenberg antiferromagnet on a square lattice. *Phys. Rev. B*, 37:5978–5981, Apr 1988. `doi:10.1103/PhysRevB.37.5978`.

[174] M. Greven, R. J. Birgeneau, Y. Endoh, M. A. Kastner, M. Matsuda, and G. Shirane. Neutron scattering study of the two-dimensional spin S=1/2 square-lattice Heisenberg antiferromagnet $Sr_2CuO_2Cl_2$. *Zeitschrift für Physik B Condensed Matter*, 96:465–477, 12 1995. `doi:10.1007/BF01313844`.

[175] A. W. Sandvik. Critical temperature and the transition from quantum to classical order parameter fluctuations in the three-dimensional Heisenberg antiferromagnet. *Phys. Rev. Lett.*, 80:5196–5199, Jun 1998. `doi:10.1103/PhysRevLett.80.5196`.

[176] J. Oitmaa, C. J. Hamer, and Z. Weihong. Heisenberg antiferromagnet and the XY model at $T = 0$ in three dimensions. *Phys. Rev. B*, 50:3877–3893, Aug 1994. `doi:10.1103/PhysRevB.50.3877`.

[177] J. Oitmaa and E. Bornilla. High-temperature-series study of the spin-1/2 Heisenberg ferromagnet. *Phys. Rev. B*, 53:14228–14235, Jun 1996. `doi:10.1103/PhysRevB.53.14228`.

[178] J. Oitmaa and W. Zheng. Curie and Néel temperatures of quantum magnets. *Journal of Physics: Condensed Matter*, 16(47):8653, nov 2004. `doi:10.1088/0953-8984/16/47/016`.

[179] J. Oitmaa. Diamond lattice Heisenberg antiferromagnet. *Journal of Physics: Condensed Matter*, 30(15):155801, mar 2018. `doi:10.1088/1361-648X/aab22c`.

[180] A. Barabanov and E. Zhasinas. The spherical-symmetric approach for the 3D S=12 Heisenberg antiferromagnet. *Physics Letters A*, 193(2):191–194, 1994. `doi:https://doi.org/10.1016/0375-9601(94)90958-X`.

[181] R.-J. Liu and T.-L. Chen. Study of the quantum spin Heisenberg model with variational-cumulant expansion to the third order. *Physics Letters A*, 194(1):137–140, 1994. `doi:https://doi.org/10.1016/0375-9601(94)00712-X`.

[182] R. A. Sauerwein and M. J. de Oliveira. Ground-state properties of the spin-1/2 antiferromagnetic Heisenberg model on a cubic lattice by a Monte Carlo method. *Modern Physics Letters B*, 9(10):619–627, January 1995. `doi:10.1142/S0217984995000589`.

[183] M. Troyer, M. E. Zhitomirsky, and K. Ueda. Nearly critical ground state of $\mathrm{LaCuO}_{2.5}$. *Phys. Rev. B*, 55:R6117–R6120, Mar 1997. `doi:10.1103/PhysRevB.55.R6117`.

[184] S. Wessel. Critical entropy of quantum Heisenberg magnets on simple-cubic lattices. *Phys. Rev. B*, 81:052405, Feb 2010. `doi:10.1103/PhysRevB.81.052405`.

[185] N. Tristan, J. Hemberger, A. Krimmel, H. A. K. V. Nidda, V. Tsurkan, and A. Loidl. Geometric frustration in the cubic spinels $M\mathrm{Al}_2\mathrm{O}_4$ (M=Co, Fe, and Mn). *Phys. Rev. B*, 72:174404, 11 2005. `doi:10.1103/PhysRevB.72.174404`.

[186] L. Ge, J. Flynn, J. A. Paddison, M. B. Stone, S. Calder, M. A. Subramanian, A. P. Ramirez, and M. Mourigal. Spin order and dynamics in the diamond-lattice Heisenberg antiferromagnets $\mathrm{CuRh}_2\mathrm{O}_4$ and $\mathrm{CoRh}_2\mathrm{O}_4$. *Phys. Rev. B*, 96:064413, 8 2017. `doi:10.1103/PhysRevB.96.064413/FIGURES/14/MEDIUM`.

[187] T. Suzuki, H. Nagai, M. Nohara, and H. Takagi. Melting of antiferromagnetic ordering in spinel oxide $CoAl_2O_4$. *Journal of Physics: Condensed Matter*, 19:145265, 3 2007. `doi:10.1088/0953-8984/19/14/145265`.

[188] A. Krimmel, H. Mutka, M. M. Koza, V. Tsurkan, and A. Loidl. Spin excitations in frustrated a-site spinels investigated with inelastic neutron scattering. *Phys. Rev. B*, 79:134406, 4 2009. `doi:10.1103/PhysRevB.79.134406/FIGURES/12/MEDIUM`.

[189] J. R. Chamorro, L. Ge, J. Flynn, M. A. Subramanian, M. Mourigal, and T. M. McQueen. Frustrated spin-one on a diamond lattice in $NiRh_2O_4$. *Phys. Rev. Mater.*, 2:034404, 3 2018. `doi:10.1103/PhysRevMaterials.2.034404`.

[190] T. Müller, D. Kiese, N. F. Niggemann, B. Sbierski, J. Reuther, S. Trebst, R. Thomale, and Y. Iqbal. Pseudo-fermion functional renormalization group for spin models. *Reports on Progress in Physics*, 2024.

[191] J. Hubbard. Calculation of partition functions. *Phys. Rev. Lett.*, 3:77–78, 1959. `doi:10.1103/PhysRevLett.3.77`.

[192] J. E. Hirsch. Discrete Hubbard-Stratonovich transformation for fermion lattice models. *Phys. Rev. B*, 28:4059–4061, 1983. `doi:10.1103/PhysRevB.28.4059`.

[193] F. F. Assaad. Phase diagram of the half-filled two-dimensional SU(N) Hubbard-Heisenberg model: A quantum Monte Carlo study. *Phys. Rev. B*, 71:1–10, 2005. `doi:10.1103/PhysRevB.71.075103`.

[194] J. E. Hirsch. Two dimensional Hubbard model. *Phys. Rev. B*, 31:4403, 1985. `doi:10.1103/PhysRevB.31.4403`.

[195] M. R. Zirnbauer. Particle-hole symmetries in condensed matter. 4 2020. `doi:10.1063/5.0035358`.

Acknowledgments

I want to thank everyone, who knowingly and unknowingly helped me during my PhD time to complete this thesis.

First and foremost I want to thank my thesis supervisor Stefan Weßel, who gave me the opportunity to stay in his group after my master's thesis, in which I was able to work on fascinating and challenging many-body systems with state-of-the-art QMC methods. With his relaxed, but always professional manner he helped me to never lose focus on what is important. I also want to thank Dante Kennes for taking the role of my second supervisor, who gave me another perspective and was always open for a chat.

I would like to thank the many people I had enlightening discussions with including everyone I met during workshops and conferences. I acknowledge funding from the DFG through the RTG 1995 and computation time provided by the Jülich-Aachen research alliance via the JARA-HPC program.

Next, I want to thank my colleagues at RWTH Aachen with whom I shared a pleasant time and entertaining coffee breaks. These include my group mates Nils Caci, Florian Kischel and Lukas Weber as well as Jonas Profe, Ammon Fischer, Clara Weber, Takuya Okugawa, Lennart Klebl, Javed Lindner, Geonho Han, Claudia Merger, Mara Caltapanides, Giacomo Passetti, Francesco Grandi, Fabian Engelhardt, Ispika Mohanty, Vanessa Wachter and Alex Rothstein.

Special thanks go to my track & field club Aachener TG and my dearest friends, who constantly reminded me that not every question in life can be answered by theoretical physics and rational thinking.

Finally, I want to thank my brother Niklas and my partner Viola for always supporting me and my parents Tatjana and Wadim, without who's courage I could not be where I am today.

Eidesstattliche Erklärung

Ich, Alexander Sushchyev, erkläre hiermit, dass diese Dissertation und die darin dargelegten Inhalte die eigenen sind und selbstständig, als Ergebnis der eigenen originären Forschung, generiert wurden.

Hiermit erkläre ich an Eides statt

1. Diese Arbeit wurde vollständig oder größtenteils in der Phase als Doktorand dieser Fakultät und Universität angefertigt;
2. Sofern irgendein Bestandteil dieser Dissertation zuvor für einen akademischen Abschluss oder eine andere Qualifikation an dieser oder einer anderen Institution verwendet wurde, wurde dies klar angezeigt;
3. Wenn immer andere eigene- oder Veröffentlichungen Dritter herangezogen wurden, wurden diese klar benannt;
4. Wenn aus anderen eigenen- oder Veröffentlichungen Dritter zitiert wurde, wurde stets die Quelle hierfür angegeben. Diese Dissertation ist vollständig meine eigene Arbeit, mit der Ausnahme solcher Zitate;
5. Alle wesentlichen Quellen von Unterstützung wurden benannt;
6. Wenn immer ein Teil dieser Dissertation auf der Zusammenarbeit mit anderen basiert, wurde von mir klar gekennzeichnet, was von anderen und was von mir selbst erarbeitet wurde;
7. Ein Teil oder Teile dieser Arbeit wurden zuvor veröffentlicht und zwar in [1, 2].

Aachen, den 05.03.2024
Alexander Sushchyev